National Centre for Nuclear Research

doctoral thesis

Towards the numerical prediction of flow and heat transfer in a tightly spaced rod bundle

Tomasz Kwiatkowski

A thesis submitted in fulfillment of the requirements
for the degree of Doctor of Physical Sciences
in the National Centre for Nuclear Research

Supervisor:
Prof. dr. hab. Mariusz P. Dąbrowski

Auxiliary supervisor:
Dr. Afaque Shams

Acknowledgments

First and foremost, I would like to express my sincere gratitude to Dr. Afaque Shams for his invaluable help, tremendous commitment, kindness and guidance he has given me over the past years. I consider it a privilege to work alongside him. I have a deep respect for his approach to problem solving and his endless spring of optimism, which always fills me with awe and inspiration. Thank you for the hours of talks, common understanding and friendship. You provided resources and guidance in the darkest of moments. It has been an unexpected journey.

I also would like to thank Professor Mariusz Dąbrowski and Dr. Sławomir Potempski for all support, patient, help, trust and a free hand to act.

Special thanks to Piotr Wasiuk and Tobiasz Jarosiewicz for constant and immediate help with software implementation and hardware usability, which I was using. Their help cannot be overestimated. I want to thank the whole team of CIŚ cluster and especially Prof. Wojciech Wiślicki, who agreed and allowed me use such tremendous computer resources!

I also acknowledge Dr. Michał Spirzewski and Piotr Prusiński, who were always willing to help with scientific and technical problems.

I want to thank all my colleagues at the National Centre for Nuclear Research for their valuable advice, interesting concepts and inspiring conversations.

To all my friends, on which I can always count on, thank you for your understanding and positive energy. Your friendship means a lot to me.

Last but not least, in particular, I wish to devote my greatest gratitude to my mom and dad and other family members for their faith in me, their help and support. I am eternally grateful for your unconditional love!

Contents

List of Figures

List of Tables

Nomenclature

Greek symbols

α thermal expansion coefficient

Δ local grid scale

δ length scale

δ_{ij} Kronecker delta

η Kolmogorov length scale

κ von Kármán constant

λ wavelength of the flow structures in the narrow gap or thermal conductivity

μ dynamic viscosity

μ_t turbulent viscosity or eddy viscosity

ν kinematic viscosity

ω specific dissipation rate

ρ density

τ shear stress

τ time scale

τ_0 time scale of large Scales Eddies with Length Scale l_0

τ_w wall shear stress

ε dissipation rate

Latin

$\langle u'v' \rangle, \langle u'w' \rangle, \langle v'w' \rangle$ turbulent shear stress components

C Courant number

D diameter

D_h hydraulic diameter

f frequency

k turbulence kinetic energy

L characteristic length scale

l_0 length scale of largest eddies

l_0 length scale of largest eddies

P/D pitch to diameter ratio

P rod pitch

T temperature

T_b bulk temperature

u, v, w spanwise, transverse and axial velocity components, respectively

u characteristic velocity

$u^{'}, v^{'}, w^{'}$ fluctuating velocity components

u_η Kolmogorov velocity

u_τ friction velocity

u_b bulk velocity

y distance from the wall

Dimensionless quantities

Pr Prandtl number

Pr_t turbulent Prandtl number

Re_τ friction Reynolds number

Re_b bulk Reynolds number

Re Reynolds number

Other symbols

$[\,]^{'}$ turbulent fluctuation term

$[\,]^{+}, [\,]^{*}$ dimensionless term

$\langle \cdot \rangle$ mean or Reynolds average

Acronyms

2D Two dimensional

3D Three dimensional

BC Boundary condition

CFD Computational Fluid Dynamics

CFL Courant-Friedrichs-Lewy

CHT Conjugate Heat Transfer

CIŚ Świerk Computing Centre

DNS Direct Numerical Simulation

LDV Laser Doppler Velocimetry

PSD Power Spectral Density

RANS Reynolds Averaged Navier-Stokes

RSM Reynolds Stresses Model

SST Shear Stress Transport Model

URANS Unsteady Reynolds Averaged Navier-Stokes

Author's contribution

The present thesis is based on the publications listed below.

List of journal publications:

*J*1) Afaque Shams, **Tomasz Kwiatkowski**, "Towards the Direct Numerical Simulation of a closely-spaced bare rod bundle", Annals of Nuclear Energy, Volume 121, 2018, Pages 146-161, doi:https://doi.org/10.1016/j.anucene.2018.07.022 [1]

*J*2) Afaque Shams, Dante De Santis, Adam Padee, Piotr Wasiuk, Tobiasz Jarosiewicz, **Tomasz Kwiatkowski**, and Slawomir Potempski, "High- Performance Computing for Nuclear Reactor Design and Safety Applications", Nuclear Technology, 206(2):283–295, 2020, doi:https://doi.org/10.1080/00295450.2019.1642683 [2]

List of conference papers:

*C*1) Thiago Cardoso De Souza, Afaque Shams, Ferry Roelofs, and **Tomasz Kwiatkowski**, "Calibration Of High fidelity bare rod bundle simulations for various PRANDTL fluids", Proceedings of the 16th International Topical Meeting on Nuclear Reactor Thermal Hydraulics 2015, NURETH-16, volume 4, pages 2774–2787, 2015. [3]

*C*2) Afaque Shams and **Tomasz Kwiatkowski**, "Design of a Closely-Spaced Rod Bundle for a Reference Direct Numerical Simulation", Proceedings of the 2018 26th International Conference on Nuclear Engineering, Volume 8: Computational Fluid Dynamics (CFD); Nuclear Education and Public Acceptance, London, England. July 22–26, 2018. V008T09A002. ASME. doi:https://doi.org/10.1115/ICONE26-81049 [4]

*C*3) Afaque Shams, Dante De Santis, Adam Padee, Piotr Wasiuk, Tobiasz Jarosiewicz, **Tomasz Kwiatkowski**, and Slawomir Potempski, "High- Performance Computing for Nuclear Reactor Design and Safety Applications", Proceedings of the conference: Advances in Thermal Hydraulics (ATH 2018), ANS Winter Meeting Embedded Topical, Orlando, Florida, USA [5]

*C*4) Adam Padee, **Tomasz Kwiatkowski**, Piotr Wasiuk, Tobiasz Jarosiewicz, Slawomir Potempski and Afaque Shams, "Assesment of high performance computing for nuclear reactor thermal-hydraulics applications", Proceedings of the 18th International Topical Meeting on Nuclear Reactor Thermal Hydraulics, NURETH 2019, Portland, USA [6]

*C*5) **Tomasz Kwiatkowski** and Afaque Shams, "Towards the accurate prediction of flow and heat transfer in a tightly spaced bare rod bundle configuration", Proceedings of the International Congress on Advances in Nuclear Power Plants - ICAPP2021, 2021, Khalifa University, Abu Dhabi (UAE) [7]

$C6$) **Tomasz Kwiatkowski** and Afaque Shams, "The Formation Of The Gap Vortex Street In Square Arranged Rod Bundles", Proceedings of the International Congress on Advances in Nuclear Power Plants - ICAPP2021, 2021, Khalifa University, Abu Dhabi (UAE) [8]

$C7$) **Tomasz Kwiatkowski**, Michał Spirzewski and Afaque Shams, "Validation of RANS Based CFD Modelling Approach for Flow in a Tightly Spaced Bare Rod Bundle with Heat Transfer in Various Prandtl Fluids", 13th International Topical Meeting on Nuclear Reactor Thermal-Hydraulics, Operation and Safety (NUTHOS-13 2022)., Hsinchu in Taiwan (under-review) [9]

Other scientific publications associated with the Computational Fluid Dynamics (CFD) but not directly related to the PhD topic:

$O1$) Dante De Santis, Andrea De Santis, Afaque Shams and **Tomasz Kwiatkowski**, "The influence of low Prandtl numbers on the turbulent mixed convection in an horizontal channel flow: DNS and assessment of RANS turbulence models", International Journal of Heat and Mass Transfer, 127, 345-358, 2018, doi:https://doi.org/10.1016/j.ijheatmasstransfer.2018.07.150 [10]

$O2$) Afaque Shams, Dante De Santis, D. Rosa, **Tomasz Kwiatkowski** and Ed J.M. Komen, "Direct numerical simulation of flow and heat transfer in a simplified pressurized thermal shock scenario", International Journal of Heat and Mass Transfer, 135, 517-540, 2019, doi:https://doi.org/10.1016/j.ijheatmasstransfer.2019.01.144 [11]

$O3$) Piotr Szymczak, Kamil Kwiatkowski, Marek Jarosinskí, **Tomasz Kwiatkowski**, and Florian Osselin, "Wormhole Formation During Acidizing of Calcite-Cemented Fractures in Gas-Bearing Shales", SPE Journal, volume 24, number 02, pages: 795-810, 2019, doi:https://doi.org/10.2118/191376-PA [12]

In particular Section 4 is based on $J1)$, $C1)$, Section 5 is partially based on $J2)$, $C2)$, $C3)$, while the Section 6 is partially based on the results presented in $C5)$, $C7)$.

The results obtained in the thesis (DNS database result) will be used in the part of the work carried out within the framework of the Preludium-17 project, which has received funding from the National Science Center (Poland) under grant agreement No 2019/33/N/ST8/00530. The author of the thesis is the Principal Investigator of this project.

The conducted research has been appreciated by the international nuclear community. The author was nominated by NUGENIA Forum 2019 to Young Generation Awards 2019. The awards were offered by the NUGENIA (NUclear GENeration II & III Association) and ENEN (European Nuclear Education Network) Associations, March 2019, Paris, France. Furthermore, author was selected to represent the NUGENIA Young Generation Community at the FISA-EURADWASTE 2019 conference, June 2019, Pitesti, Romania (participation fully funded by the European Commission).

In 2021, the author of a doctoral dissertation was awarded the prize of **the Future Scientist 2021** in the category: Science and Technology for an Innovative Future. The award was granted by the jury of the competition of the Intelligent Development Forum. (Nagroda: Naukowiec Przyszłości 2021, w kategorii: Nauki ścisłe i techniczne dla innowacyjnej przyszłości. Forum Inteligentnego Rozwoju).

Abstract

An accurate prediction of the flow distribution inside fuel rod bundles is required for both design and safe operation of innovative as well as conventional nuclear systems. The unsteady axial characteristic flow pulsations which appear in the bare rod bundle configuration have been investigated (experimentally and numerically) over the last 70 years and remain a research topic up to the present time.

In the past, the majority of studies of flow and heat transfer inside the fuel rod bundles have been performed experimentally. However, most of them were conducted on the simplified geometries and under conditions that are not the same as in normally operating reactors.

A good prediction of the flow and heat transfer inside the rod bundle is a challenge for the available and commonly used RANS (Reynolds-Averaged Navier-Stokes) turbulence models and these models need to be validated and improved accordingly. Although the measurement techniques are constantly getting improved, the CFD-grade (Computational Fluid Dynamics) experiments of flow mixing and heat transfer in the subchannel scale are often impossible or quite costly to be performed. In addition, lack of experimental databases makes it impossible to validate properly and/or calibrate the available RANS turbulence models for certain flow situations. In that context, Direct Numerical Simulation (DNS) can be served as a reference for model development and verification.

In this thesis, a numerical experiment for a tight lattice bare rod bundle case using different Prandtl fluids (air, water, liquid metal) is designed. In the next step, the high fidelity database by means of DNS is generated. The obtained DNS results serve as a reference database to validate and calibrate/improve the available and commonly used low order turbulence models. The RANS turbulent models are thoroughly investigated in order to understand their capabilities and limitations. Finally, the comprehensive CFD methodology toward the accurate prediction of turbulent flow and heat transfer phenomena at sub-channel level with the set of the best practices guidelines is developed.

Streszczenie

Poprawne modelowanie przepływu chłodziwa wewnątrz kasety paliwowej reaktora jądrowego jest jednym z głównych problemów badanych zarówno przy projektowaniu nowych reaktorów, jak i w analizach bezpieczeństwa tych istniejących. Przepływ w ściśle upakowanych kasetach paliwowych charakteryzuje się występowaniem pulsacji płynu pomiędzy sąsiadującymi prętami paliwowymi. Zjawisko to badane było (eksperymentalnie oraz numerycznie) przez ostatnich 70 lat i wciąż pozostaje nie do końca rozwiązane.

W przeszłości badania przepływu i wymiany ciepła wewnątrz kasety paliwowej realizowane były zazwyczaj eksperymentalnie. Niestety, większość z tych eksperymentów rozważała jedynie uproszczone geometrie w warunkach odbiegających od warunków normalnej pracy reaktora jądrowego.

Poprawne modelowanie przepływu i wymiany ciepła wewnątrz kasety paliwowej reaktora jądrowego jest wyzwaniem dla dostępnych i powszechnie stosowanych uśrednionych modeli turbulencji, tzw. modeli RANS (Reynolds-Averaged Navier-Stokes). Modele te wymagają walidacji oraz udoskonalenia. Chociaż eksperymentalne techniki pomiarowe są stale poprawiane, to eksperymenty przepływowe klasy CFD (numeryczna mechanika płynów) są często niemożliwe lub zbyt kosztowne do przeprowadzenia. Ponadto brak eksperymentalnych baz danych uniemożliwia prawidłową walidację i/lub kalibrację dostępnych modeli turbulencji RANS dla konkretnych zastosowań. W tym kontekście rozwiązaniem staje się podejście CFD. Stosując najbardziej wyrafinowaną technikę tzw. Direct Numerical Simulations - DNS, można stworzyć numeryczne referencyjne bazy danych, które utożsamiane są z danymi pozyskanymi z eksperymentów fizycznych.

W niniejszej rozprawie zaprojektowano eksperyment numeryczny dla geometrii ściśle upakowanej kasety paliwowej, w której chłodziwem są płyny o różnych liczbach Prandtla (powietrze, woda, ciekły metal). Wygenerowana została numeryczna baza danych wysokiej wierności za pomocą techniki DNS. Pozyskane w ten sposób dane mogą służyć jako dane referencyjne do walidacji i kalibracji dostępnych i powszechnie stosowanych modeli turbulencji niższego rzędu. W tym sensie szereg modeli typu RANS zostało dokładnie sprawdzonych w celu określenia ich możliwości i ograniczeń. Opracowana została także kompleksowa metodologia CFD w celu dokładnego modelowania zjawiska turbulentnego przepływu i wymiany ciepła w geometrii ściśle upakowanej kasety paliwowej z zestawem kryteriów dotyczących tzw. najlepszych praktyk.

1 Introduction

1.1 Motivation and research questions

Rod bundles form the basic configuration for most of the fuel element designs used in the existing and future nuclear reactors. They consist of tightly packed arrays of rods, which contain the nuclear fuel and are surrounded by flowing coolant. Coolant flowing through the channels within the fuel assemblies removes the heat generated by the nuclear fission. In an ideal scenario, the temperature distribution through the fuel assemblies should remain uniformly distributed under normal operating conditions of a nuclear reactor. However, in reality this does not happen, and accordingly, it leads to inter-subchannel mixing phenomena.

Given the high priority of safety in the operation of nuclear reactors, it is necessary to have a comprehensive understanding of the coolant flow behavior. The interesting geometry of the rod bundles, with the presence of wide and narrow regions results in a unique flow profile, with the presence of large-scale swirling structures, so-called gap vortex street [13]. These structures are known to be coherent in nature and result in cross-flow zones in the otherwise axial flow in rod bundles.

These peculiar flow patterns differ from the ones encountered in regular channel and pipe flows. The correct prediction and control of these flow distribution is essential for the reactor design and safety assessment, and has been an active area of research in reactor thermal-hydraulics.

Additionally, to the flow characteristics there is another very important phenomena, namely turbulent heat transfer. Turbulent heat transfer is an extremely complex phenomenon that has challenged turbulence modellers for various decades. Both turbulent momentum and heat transfer are based on the same physical mechanism of cross-streamwise mixing of fluid elements. Therefore, modellers have often assumed that the turbulent heat transfer can be predicted from the knowledge of momentum transfer; this

approach is known as the Reynolds analogy. Even though this approach is overly simplistic, it has been successfully adopted for several decades in a large majority of industrial applications of Computational Fluid Dynamic (CFD), which are based on Eddy Diffusivity models (EDM). This success is justified because for fluids with a Prandtl number (Pr) close to unity and particularly in wall-bounded forced convection flows, this approach has provided reasonable predictions of global parameters such as Nusselt numbers and mean temperature distributions.

Fig. 1 provides an overview of the Pr for different working fluids used in different reactor types [14]. It is clearly noticeable that apart from the gas-cooled reactor, none of the working fluids exhibit equality in the momentum and the thermal boundary layer. Therefore, one should always be careful in applying the Reynolds analogy to non-unity Pr fluids, particularly to low-Pr fluids and must realize its limitations with respect to accuracy. Nevertheless, the obvious limitations of this assumption for natural and mixed convection flow regimes have become more evident and are highlighted in [15, 16].

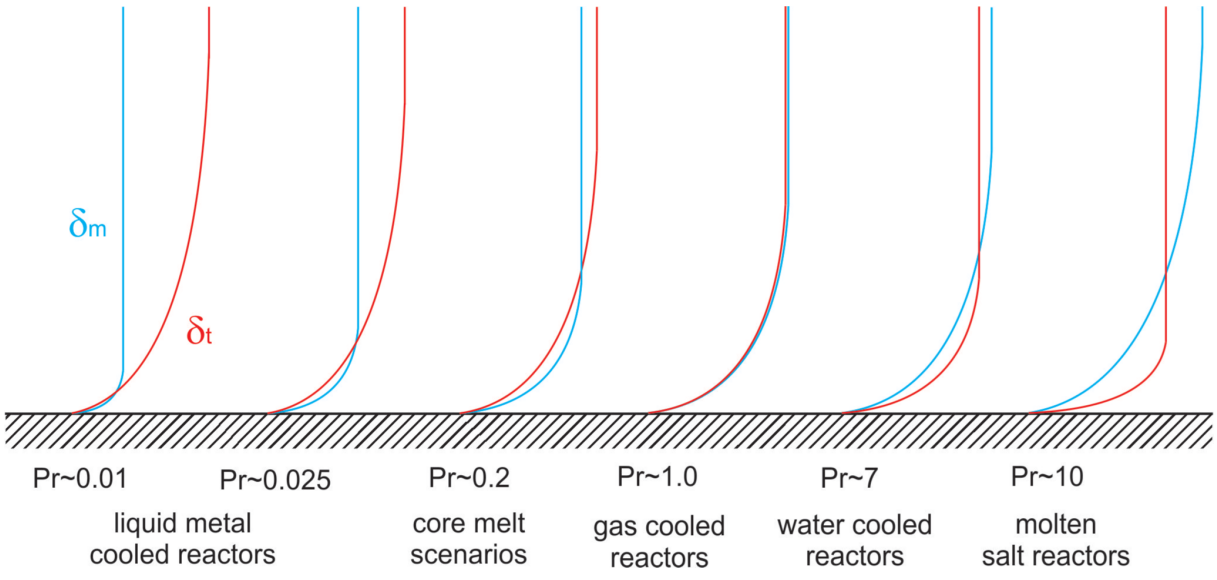

Figure 1: Comparison of momentum (δ_m) and thermal (δ_t) boundary layers for different working fluids in various reactor applications [14].

Several investigations have been undertaken to study the velocity and temperature fields associated with the thermal mixing in the bare rod bundle configuration. However, the available experimental databases are not sufficient to describe the involved physics in adequate detail, and, due to experimental limitations, accurate data on velocity and temperature fluctuations in regions close to the wall are not available. CFD can play an important role in predicting such complex flow features. However, predicting complex thermal and momentum phenomena is a challenge for the available pragmatic turbulence models. Therefore such models need to be extensively validated and, if needed, improved accordingly.

Taking this into account, the author decided to develop the comprehensive methodology regarding the validation approach of URANS turbulent models. As a first step in a validation approach toward fuel assembly level and ultimately reactor core level modelling, a CFD methodology needed to be developed which provided accurate predictions for heat transport and unsteady flow phenomena (gap vortex street formation) at sub-channel level. The high fidelity CFD (by means of Direct Numerical Simulations - DNS) provided reference data for RANS approaches validation. Those were objectives of the research project which are more extensively described in the following subsection 1.2.

The author conducted a comprehensive analysis of this concept and formulated the following **Thesis Statement:** "The accurate prediction of turbulent flow and heat transfer phenomena inside nuclear rod bundles is very challenging for "off-the-shelf" URANS models. Therefore this models need to be properly validated and if needed accordingly improved. This is especially important for non-unity Prandtl number (Pr) flows, particularly in the liquid metal flows."

1.2 Objective of the study

There are four main objectives of the present PhD project.

The first is to design a numerical experiment for a tight lattice bare rod bundle case using different Prandtl fluids, which is used in order to generate DNS type reference database. This takes into account the turbulent mixing and the evolution of the temperature distribution for fluid flow. In order to do this the calibration methodology is developed. In the calibration procedure the geometrical configuration as well as boundary conditions have been investigated. Eventually, the final closely-spaced rod bundle configuration, which is feasible for the available computational resources have been set up.

The second objective was to generate the high fidelity database by means of Direct Numerical Simulations (DNS). The obtained DNS results served as a reference database to validate and calibrate/improve the available and commonly used low order turbulence models.

The third objective is the validation of pragmatic CFD turbulent models. To the date, none of the commonly used turbulence models have been validated for this particular case of a turbulent flow in a tightly spaced bare rod bundle configuration. To make the most appropriate choice of model for specific application, one needs to understand the capabilities and limitations of the various options and models.

The last objective, which in a way is the essence and the resultant of the aforementioned three objectives, is the development of comprehensive CFD methodology toward the accurate prediction of turbulent flow and heat transfer phenomena at sub-channel level with the set of the best practices guidelines.

1.3 Outline of the thesis

The dissertation consists of seven chapters. The comprehensive **scope** of work is outlined below.

The first chapter presents the theses, objectives, and scope of the dissertation.

The second chapter describes the state of the art considering flow and heat transfer in the rod bundles. This chapter consists of two subsections - the first one is devoted to the experimental findings while the second one describes the results of the numerical simulations.

The third chapter contains the general description of turbulent approaches used in the calculations performed in the dissertation. Additionally the used turbulence models are briefly presented.

Chapter four describes the whole procedure and methodology developed in order to design a numerical experiment. Performing a DNS computation requires a huge amount of computational power. Hence, a wide range of unsteady RANS study has been performed to calibrate and optimize the case for the targeted DNS study. As a first step, the Reynolds number of the original experimental Hooper case is scaled down in such a way that the overall phenomenology of the flow field remains the same, i.e. the very existence of the axial flow pulsations. Afterwards, the calibration of the computational domain with the respective boundary conditions is performed in order to obtain an optimized Hooper case, which is feasible for the available computational resources. In addition to the flow field, a parametric study for four different passive scalars is performed to take into account the heat transfer analysis, which was not included in the original Hooper case. These passive scalars correspond to the Prandtl numbers of three different working fluids, i.e. air, water and liquid metal fluids. The

heat transfer of these three fluids has been studied in combination with two different boundary conditions at the walls, i.e. a constant temperature and a constant heat flux. Accordingly, the final DNS set-up has been assessed.

The fifth chapter, based on the previously prepared parameter configuration, the DNS of the Hooper case are performed. As it was already mentioned, the thermal boundary conditions used in this work are both iso-thermal and iso-flux conditions which correspond to the two extreme scenarios of a Conjugate Heat Transfer (CHT). The fluid properties are assumed to be constant. Hence, the temperature is treated as a passive scalar. Thanks to this assumption in one single DNS computation, multiple passive scalars have been included. These passive scalars correspond to the Prandtl numbers of three different working fluids, i.e. water, air and liquid metal fluids, i.e. Pr = 2, 1 and 0.025, respectively. The heat transfer of these three fluids has been studied in combination with two different boundary conditions at the walls, i.e. a constant temperature and a constant heat flux. Therefore, in total, the DNS computation consists of six thermal fields. Thus, the final DNS yield in an extensive validation database for flow and the thermal fields representing different reactor coolants.

In the sixth chapter the validation of pragmatic RANS turbulent models is presented. The aim of the validation study is to assess the capabilities of different turbulence models for prediction of turbulent flow and heat transfer in a tightly spaced bare rod bundle. It is worthwhile to mention that none of the considered turbulence models is tuned for a particular case of a turbulent flow in a tightly spaced bare rod bundle configuration.

The last chapter is a summary of the work. The results presented in the previous sections are comprehensively discussed and analyzed.

2 Turbulent flow and heat transfer in rod bundle

The patterns, which are formed in a moving fluid have fascinated people since the earliest recorded observations of Leonardo da Vinci. In order to portray the random and chaotic behavior of these unique patterns, he used the word **turbulence** ("la turbolenza" - in Italian, originating from Latin "turba", which means turmoil).

Turbulence is commonly observed in everyday phenomena such as fast flowing rivers, billowing storm clouds, or smoke from a chimney, and most fluid flows occurring in nature or created in engineering applications are turbulent. Turbulent flows could exhibit organized motion of different scales. The figure 2 depicted the diversity in the scale of these organized patterns for flow past different obstacles:

- an island - in nature (source: Image by USGS, Public domain). The flow pattern visualized by clouds off the Chilean coast near the Juan Fernandez Islands (also known as the Robinson Crusoe Islands) photographed by the Landsat 7 satellite on September 15, 1999.
- a cylinder - in the laboratory [17].

An interesting feature of these vortical patterns is their coherence, i.e., they retain their identity for a significant lifetime and appear repeatedly in more or less the same form (henceforth-coherent vortices or vortex street).

The coherent vortices, despite its aesthetic appearance, have the potential of affecting the transport and mixing of passive particles (water masses, temperature, pollutants, etc.). Passive particles, mean particles that take on the velocity of a fluid very rapidly without a significant influence on the flow field. This property marks the practical significance of the coherent vortices in meteorology, oceanography and different engineering applications. For example, environmental dispersion of pollutants, sediment transport along the banks of a flood plain and heat transfer in the core of a nuclear reactor (often being a tube bundle geometry).

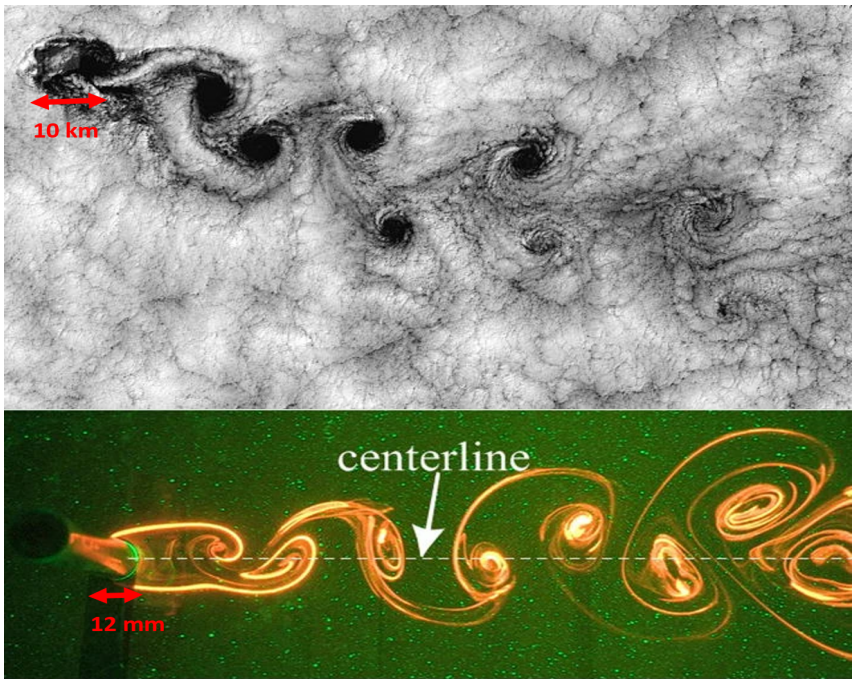

Figure 2: Vortex street in the wake of an island (upper - source USGS) and cylinder (bottom - [17]).

Development of a deep understanding of the transport by coherent structures in the core section of a nuclear reactor is one of the primary aim of the work presented in this thesis.

2.1 Vortex street in rod bundle

Nuclear fuel rods in the most of existing and future nuclear reactors are grouped into fuel assemblies, characterized by their geometric arrangements. Mainly, it is either square or triangular configuration, where coolant is flowing axially through the bundles. The flow area bounded by four or three fuel tubes defines a sub-channel as depicted in Fig. 3. Two adjacent sub-channels are connected by a gap between two rods. This gap spacing is defined as a pitch (P) to rod diameter (D) ratio (P/D). The fuel rod assembly belongs to the class of compound geometries, where flow is identified by a peculiar patterns, which are not encountered in pipes or simple channels.

Depending on the P/D ratio, the axial coolant flow in a bare rod bundles

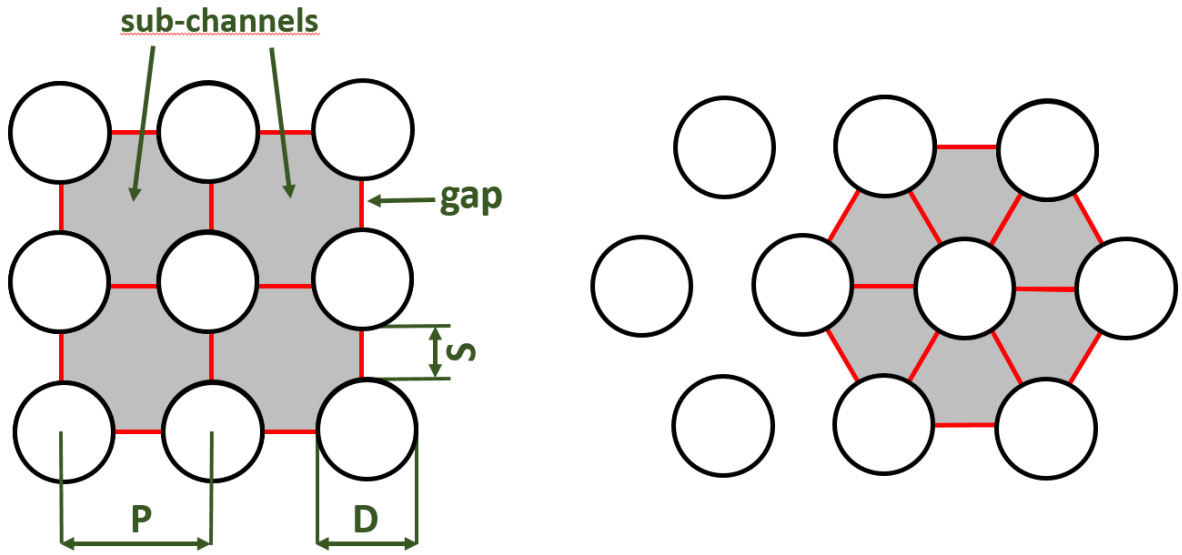

Figure 3: Cross-sectional view of a square (left) and triangular (right) pitched tube bundle defining gaps and sub-channels.

is characterised by strong, transverse, large-scale motions across the gaps between neighbouring fuel assemblies, which extremely enhance the mixing between flows in adjacent sub-channels (see Fig. 4). An appropriate term to characterize these flow patterns is gap vortex street [13]. These vortices are profitable from the heat transfer point of view. However, the gap instability [13] could cause flow-induce vibrations in rod bundles, which in turn could result in temperature pulsations.

These temperature pulsations may result in a fatigue of structure materials of fuel cladding [18]. It is worth pointing that coolants ranging from liquid metals to molten salts, yield a wide variety of heat transfer conditions. Keeping the above aspects in mind, it is crucial to accurately predict flow and temperature distribution inside fuel rod bundles from design and safe operation point of view. The unsteady axial flow pulsations/structures, which appear in the bare rod bundle configuration, have been investigated (experimentally and numerically) over the last 50 years and remain a topic of interest up to the present time [19].

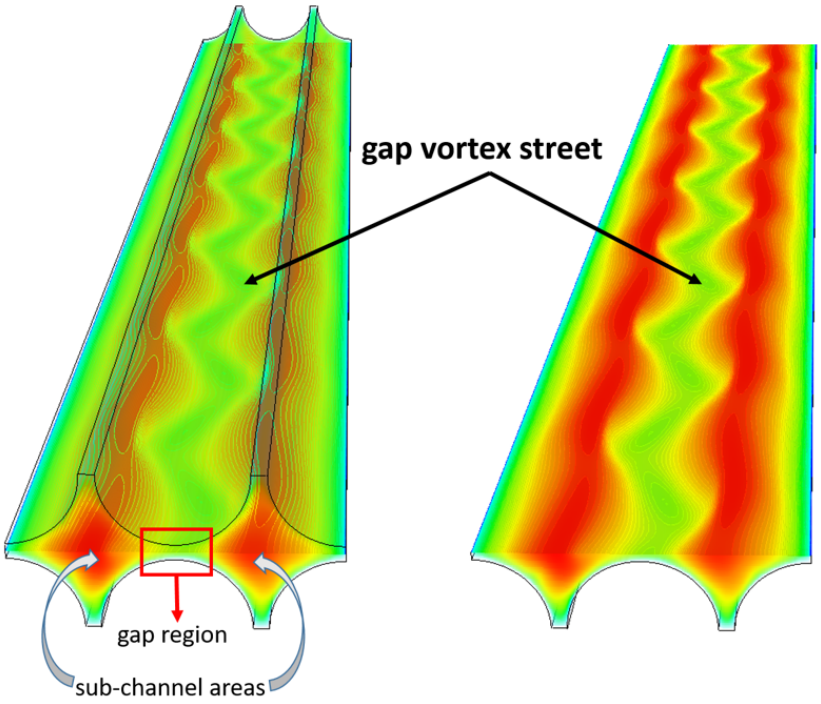

Figure 4: Gap vortex street created in the gap region between two adjacent sub-channels.

2.2 Experimental observations

Numerous experiments have been carried out to investigate a fully developed turbulent flow in the bare rod bundles. A mechanism constituting the single-phase crossflow in a bare rod bundle and influencing the process of inter-subchannel mixing was identified by Rogers and Todreas [20]. In the following years the existence of large-scale coherent vortices near the gap region in a bare rod bundle geometry has been verified by a different research groups around the world.

In 1973, Rowe [21] specified the implications on the existence of periodic flow pulsation in the bare rod bundle with the use of two-component Laser Doppler Velocimetry (LDV). Moreover, he showed, that *the P/D ratio is the most significant geometric parameter* affecting the flow structure.

Trupp and Azad, in 1975 [22], checked the spatial distribution within a primary flow cell of the mean velocity and Reynolds stresses as a function of Reynolds number and tube spacing [22].

In an experimental study of Hooper [23], it was found that the departure of the turbulent flow structure from axisymmetric pipe flow, especially in the rod gap region, *strongly depends on the P/D ratio.* In particular the axial and azimuthal turbulence intensity in the rod gap region, for developed turbulent flow through parallel rod bundles, increase strongly with decreasing rod spacing [24, 25]. Additionally, Hooper and Wood [26] showed that the wall shear stress distribution is determined primarily by the pressure gradient and the transverse shear stress ($\overline{uw}$), which in turn confirmed the negligible size of the mean secondary flow.

In 1991, Möller [27] pointed out that flow pulsations have a characteristic frequency, which depends on the rod bundle geometry (P/D ratio) and on the flow velocity.

In 1995, Lee at al. [28] developed a linear relationship between turbulent normal stresses and turbulent kinetic energy for fully turbulent flow through regularly spaced bare rod arrays.

Additionally to the mentioned studies, researchers were investigating the spatial correlations of coherent structures in the rod-wall gap region. In the following works [29–35], it was confirmed that the flow near the narrow gaps between rods and between rods and surrounding duct was dominated by quasi-periodic transverse flow pulsations, and these pulsations contributed significantly to the velocity fluctuations across the gap. The source of the flow pulsations are large-scale vortices, which form in pairs on either side of each gap. A "coherent" structure is a connected, large-scale turbulent fluid mass with a phase-correlated vorticity over its spatial extent [36]. That is, underlying the three-dimensional random vorticity fluctuations characterizing turbulence, there is an organized component of the vorticity which is phase correlated (i.e., coherent) over the extent of the structure.

The proper prediction of the flow behaviour in rod bundles is of fundamental concern in a variety of engineering fields. It is especially important, if the heat transfer is taken into account. Inside heated rod bundles, co-

herent structures across the gap region would prominently enhance the mixing of fluid between two adjacent sub-channels and local convective heat transfer. This results in extracting more heat from the rod walls and decreasing the average fluid temperature in the gap region. Any distortion in the geometries of gap region (such as flow-induced vibrations or thermally induced rod deformation) could lead to local overheating [37], which in consequence, can lead to boiling and dryout, and further can catastrophically affect the operation of the system. The effects of the turbulent temperature fluctuation were extensively investigated in [38–41].

2.3 Numerical simulations

Nowadays, with the expansion of the computer technology, the Computational Fluid Dynamics (CFD) simulations are another widely used methodology to study the flow and heat transport which can substitute/replace experiments. In fact, numerical modeling, in the form of CFD, represents an essential tool which can allow overcome the limitations of traditional experimental techniques. This is because experiments are very often performed on the idealized geometries, under normal conditions (ambient conditions) or measurements are limited to points, lines or single planes. In this regard, CFD has been considered as an attractive alternative.

The most accurate and reliable CFD method is the Direct Numerical Simulation (DNS). In the past, only a few DNS studies have been performed [42, 43]. Besides, these computations were limited to low Reynolds number and the selected computational domain was relatively small.

Another method, Large Eddy Simulation (LES) approach is computationally less demanding than DNS and it enables simulating flow at relatively larger Reynolds number and a bigger rod bundle computational domain. Numerous researchers have utilized the LES approach to simulate momentum and heat transfer in different rod bundle configurations [42, 44–53].

It is important to realize that a successful prediction of flow pulsations requires relatively long streamwise computational domain, which allows the development of large axial coherent structures. Therefore, most of the simulations aiming to reproduce pulsations in rod bundles applied a computationally less demanding approach, i.e. Unsteady Reynolds-Averaged Navier-Stokes (URANS) simulation. Several URANS studies [3, 18, 43, 49, 51,54–58] have been performed to predict the appearance of flow pulsations in rod bundles (particularly in the closely packed bundles).

CFD techniques are realized as more ond more reliable tools in nuclear engineering. The papers of [19, 59, 60] provided an extensive reviews of the experimental and numerical analysis for the thermal hydraulic phenomenon in tight lattice sub-channels and in particular turbulent models prediction capabilities. The authors summarized that the URANS modelling approach, especially based on anisotropic models, was able to predict the overall flow characteristics in tightly packed rod bundle. It is worthwhile to mention that these conclusions are mainly related to the flow field prediction. An accurate prediction of heat transfer in rod bundle configuration is an additional issue that needs more attention in terms of numerical studies. Turbulent heat transfer is an extremely complex phenomenon and has challenged turbulence modellers for many decades [19]. The modellers have often assumed the possibility that turbulent heat transfer may be predicted only from the knowledge of momentum transfer, in what is known as the Reynolds analogy. Although this assumption is overly simplistic, it has been successfully adopted for the last four decades in the large majority of industrial applications of CFD, which are based on Eddy Diffusivity models (EDM). The success is related to the fact that for fluids with a Prandtl number close to unity, this approach has provided reasonable predictions.

Nevertheless, a good prediction of the flow and heat transport inside the rod bundle is a challenge for the available URANS turbulence models and these models need to be validated and improved accordingly. Although

the measurement techniques are constantly getting improved, the CFD-grade experiments of flow mixing and heat transfer in the sub-channel scale are often impossible or quite costly to be performed. In addition, lack of experimental databases makes it impossible to validate properly and/or calibrate the available RANS turbulence models for certain flow configuration/application. In that context DNS can serve as a reference for model development and verification. However, despite the advancement in the super computing, performing a DNS for a realistic rod bundle at a high Reynolds number is not foreseeable in the near future. In this regard, a research program has been initially set up between Nuclear Research and Consultancy Group (NRG), the Netherlands, and National Centre for Nuclear Research (NCBJ), Poland, to generate a high-quality DNS database for a rod bundle configuration. The project started in 2017 and has been lasting up to spring 2022. In 2021 NRG proposed some parameter changes in the basic DNS set-up in order to accelerate the simulations. At the same time, the author decided to continue the calculations with the base settings, which took into account very restrictive settings regarding the time step, so as not to lose the accuracy of the final calculations. The results of the DNS with the base configuration are presented in this thesis.

3 Turbulence theory and turbulence modelling

3.1 Brief introduction

Turbulence is the apparent chaotic motion of fluid flows. Fluid flows can be laminar, when they are regular and flow in an orderly manner. When the speed or characteristic length of the flow is increased, the convective forces in the flow overcome the viscous forces of the fluid and the laminar flow transitions into a turbulent one. The ratio between convective and viscous forces is called the Reynolds number. This number can be used to classify the type of flows, the higher the number the more turbulent the flow is.

In general, fluids flows can be categorized into laminar, transitional and turbulent flow. Most of the flows around us are turbulent flows, e.g. a strong wind, the flow in the river, even the wind generated by funs. The turbulent flow is prevalent in industrial applications mainly due to its high mixing rate compared to laminar flow. For example, the flows in the nuclear reactor core or in the jet engine or in the pipe of oil refinery are all turbulent flows. The turbulence theory included in the section is very brief, more details can be found in several textbooks, for instance Pope (2000) [61, 62].

3.2 Characteristic of turbulent flow

Although the turbulent flow widely exists in the world and has been studied over a century, no one can give a precise definition of turbulence. However some common characteristics of it have been established, which are listed below.

Randomness - all of the turbulent flows are random or irregular, which makes the statistical tools important in turbulence studies. However, not all of the irregular flows are turbulent.

Diffusivity - one of the main differences between the turbulence and laminar flow is that turbulence can result in more efficient fluids transport and mixing, which are important features concerned in many applications.

Rotational and three dimensional - all of the turbulent flows contain high level of turbulent vortices. As a result, the irrotational random waves cannot be classified into turbulence.

Dissipation - the kinetic energy of turbulence is dissipated by the viscous shear stress and added as internal energy to fluids. So the continuous supply of energy from the mean flow is needed to maintain the existence of the turbulence vortices.

Continuous - turbulence is a continuous phenomenon, governed by the Navier-Stokes equations [62].

Turbulence is the characteristic of the flow - turbulence is a feature of the flow. It can be characterized by using the dimensionless parameter Reynolds number (Re), proposed by Osborne Reynolds (1894) and defined as

$$Re = \frac{uL}{\nu} = \frac{\rho u L}{\mu}, \tag{3.1}$$

where: u is the flow speed, L is the characteristic dimension, ν is the kinematic viscosity, ρ is the density if the fluid, $\mu = \nu\rho$ is the dynamic viscosity.

No matter what fluid it is, the dynamics of the turbulence is similar, if the Reynolds number is the same. According to the observation in Reynolds's experiment, the flow remains laminar when $Re < 2300$, but becomes turbulent when $Re > 4000$. The turbulence arises from the instability

mechanism in the high Reynolds number flows, which would cause three-dimensional disturbances. The local three dimensional disturbances would merge with each other forming a turbulence flow field [62].

3.3 Energy cascade and turbulent scales

Turbulent flows are unsteady and three dimensional in nature. One of the main advantage turbulence offers in industrial applications is enhanced mixing. Inside a nuclear reactor, it is important that the coolant is well mixed and the heat is distributed evenly. The flow in physics of interest is essentially characterized by turbulent transfers (e.g., momentum and energy transfers). Turbulent flows are characterized by a full spectrum of space and time scales, ranging from large scales, driven by the geometry and boundary conditions, down to the smallest scales where the energy is finally dissipated. This phenomenon is named as energy cascade. The idea of energy cascade was first suggested by Richardson (1922) [63] and later quantified by Kolmogorov (1941) [64].

This statistic-based theory relies on local isotropy and similarity assumptions. The energy cascade means that because of the nonlinear interactions between the different scales, the energy transfer takes place from the large scales to the small ones. At some point, depending on the Reynolds number, the energy transfer competes with the viscous dissipation of the energy into heat, and this latter effect becomes dominant. The final dissipation occurs at a scale defined by Kolmogorov and called the Kolmogorov scale. This energy cascade is represented by a relation between the local characteristic wavenumber k of eddies and the turbulent kinetic energy contained by such eddies $E(k)$ (see Fig. 5).

The large wavenumber range (e.g., the large scales) is the production range where the energy is injected into turbulence because of existing gradients in the mean flow or any external forcing. Thus, one can find here the largest eddies containing most of the energy. The high wavenumber range

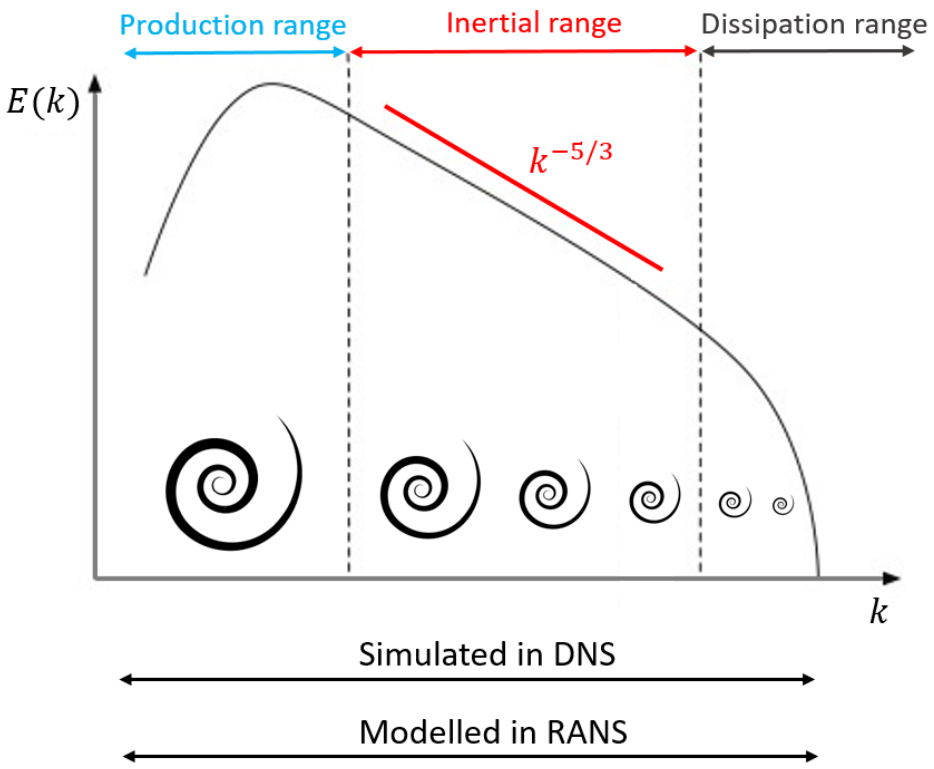

Figure 5: The energy cascade of turbulence.

or small scales is the dissipation range where the smallest eddies could be found and where viscosity is playing an important role. Between these two zones is the inertial range where the energy transfers from the larger scales to the smallest ones. The extent of this zone is function of the Reynolds number as it gives an idea of the difference between the largest scales and the smallest scales present in the flow. Actually, as the Reynolds increase the smallest scales become even smaller while the large scales are not significantly modified because they are more related to the geometry. The largest eddies of this range (inertial range) are proportional to the physical geometry, while the smallest are determined by the viscous dissipation and viscosity. Along the inertial range, under an equilibrium assumption, the transfer rate of energy between scales equals the dissipation rate ε.

The dimension of $E(k)$ is $(m^3 s^{-2})$. In the inertial range $E(k) = f(k, \varepsilon)$. As k has the dimension (m^{-1}), and the dissipation ε has the dimension $(m^3 s^{-3})$ it gives:

$$E(k) \sim \varepsilon^{2/3} k^{-5/3}. \tag{3.2}$$

This finally gives the so-called Kolmogorov law $E(k) = C_K \varepsilon^{2/3} k^{-5/3}$ with $C_K = 1.6$ and explains the $-5/3$ slope in Fig. 5 for the inertial range.

According to Richardson's theory, the various turbulent vortices in the turbulent flow can be characterized by their length scale. For the eddies with a length scale l, its characteristic velocity can be written as u_l, and then, the time scale can be defined as $\tau = \frac{l}{u_l}$. The large scales vortices have the length scale l_0, which is comparable to the flow scale L, while their characteristic velocity u_0 has the same order of the root mean square (r.m.s.) of the fluctuating velocity. So, the time scale of the largest eddies can be defined as $\tau_0 = \frac{l_0}{u_0}$. The Reynolds number of these eddies is large, so the dissipation effect of molecular viscosity is small enough to be ignored.

However, the large eddies are unstable due to the existence of the strain field. They would break into smaller eddies with energy transfer. These smaller eddies follow the same mechanism, transferring the energy to even smaller eddies. This process continues until eddies are sufficiently small, while the molecular viscosity can effectively dissipate the kinetic energy. This means that the energy just dissipates at the end of process. The rate of dissipation ε is determined by the rate of transfer of energy at the first step of the process, which can be written as

$$\varepsilon = \frac{u_0^2}{\tau_0} = \frac{u_0^3}{l_0}. \tag{3.3}$$

There are some questions remaining in Richardson's theory. What is the size of eddies which molecular viscosity can effectively dissipate the energy from? What is the relations between the length scale of eddies and the characteristics velocity/time scale? These questions were answered by Kolmogorov [64] in the form of three hypotheses.

Kolmogorov's hypothesis of local isotropy - the small scale turbulent motions are statistically isotropic, if the Reynolds number is high enough.

Kolmogorov's first similarity hypothesis - in every turbulent flow at sufficiently high Reynolds number, the statistics of the small-scale motions have a universal form that is uniquely determined by ν and ε. Then the so-called Kolmogorov scales can be defined as

$$\eta = (\frac{\nu^3}{\varepsilon})^{1/4}, \tag{3.4}$$

$$u_\eta = (\varepsilon\nu)^{1/4}, \tag{3.5}$$

$$\tau_\eta = (\frac{\nu}{\varepsilon})^{1/2}, \tag{3.6}$$

where: η, u_η, τ_η are the Kolmogorov length scale, the Kolmogorov velocity scale, and the Kolmogorov time scale, respectively. It is easy to conclude that the Reynolds number evaluated by the Kolmogorov scales is equal to unity.

Combining equation (3.3) with equations (3.4), (3.5), (3.6), the relation between the scales of smallest eddy and largest ones can be written as

$$\frac{\eta}{l_0} \simeq Re^{-3/4}, \tag{3.7}$$

$$\frac{u_\eta}{u_0} \simeq Re^{-1/4}, \tag{3.8}$$

$$\frac{\tau_\eta}{\tau_0} \simeq Re^{-1/2}. \tag{3.9}$$

Kolmogorov second similarity hypothesis - in every turbulent flow with sufficiently high Reynolds number, the statistics of the motion of scale of l in the range $\eta \ll l \ll l_0$ have a universal form that is uniquely determined by ε, independent of ν. The velocity scales and time scales can be formed by l and ε:

$$u_l = (\varepsilon l)^{1/3}, \tag{3.10}$$

$$\tau_l = \left(l^2/\varepsilon\right)^{1/3}. \tag{3.11}$$

3.4 Navier-Stokes equations

The motion of fluids can be described by a set of equations, named after Claude-Louis Navier and George Gabriel Stokes, which are based on three basic physical principles: mass conservation, second Newton law, and energy conservation. The incompressible forms of the equations are listed below.

The continuity equation (mass conservation):

$$\frac{\partial u_i}{\partial x_i} = 0. \tag{3.12}$$

The momentum conservation equation (Newton law):

$$\frac{\partial u_i}{\partial t} + u_j \frac{\partial u_i}{\partial x_j} = -\frac{1}{\rho}\frac{\partial p}{\partial x_i} + \nu \frac{\partial^2 u_i}{\partial {x_j}^2}, \tag{3.13}$$

where: ρ - density, ν - kinematic viscosity.

The energy conservation equation:

$$\frac{\partial T}{\partial t} + u_j \frac{\partial T}{\partial x_j} = \frac{\nu}{Pr}\frac{\partial^2 T}{\partial {x_j}^2}, \tag{3.14}$$

where: Pr - is the Prandtl number.

The Prandtl number (Pr) is a dimensionless number, named after the German physicist Ludwig Prandtl, defined as the ratio of momentum diffusivity to thermal diffusivity. The Prandtl number is given as:

$$Pr = \frac{\nu}{\alpha} = \frac{momentum \;\; diffusivity}{thermal \;\; diffusivity}, \tag{3.15}$$

where α - thermal expansion coefficient.

No analytical solution of Navier-Stokes equations is supplied by the mathematicians. This is mainly due to the non-linear convective term and pressure gradient terms in the equations. However, these equations can be solved numerically. A brief introduction on the simulation and turbulence modelling is included in Section 3.5.

3.5 Turbulence Modelling and Numerical Method

The turbulent flow can be studied either by experiment or by numerical simulation. In comparison with the experimental method, the numerical simulation is generally cheaper and more efficient, but it is necessary to check the reliability of the numerical models using experimental results. The most accurate computational approach is Direct Numerical Simulation (DNS), which solves the Navier-Stokes equations directly and resolves all of the scales of turbulence, as shown in Fig. 5. However the cost of this method is extremely high. From the CFD point of view, where space is discretized in a finite number of cells in each direction, equation (3.7) has a crucial consequence. Indeed, l_0 is proportional to L, the physical geometry length scale, which can be discretized by n points in each direction of space, $L = n\Delta h$, Δh being the grid size. This implies in 3D:

$$n^3 \sim Re^{9/4}. \tag{3.16}$$

From eq. 3.16 the number of mesh elements required for resolving the three dimensional flow is proportional to $Re^{9/4}$. For example, to investigate

a flow with $Re = 10000$, the total number of mesh element required by using DNS is in the order of 10^9, which makes this method too expensive for almost all industrial applications. More precisely, as a grid of size h could capture an eddy of size $2h$ (Nyquist theorem [65]), an ideal DNS grid would require $h_{DNS} \leq 2\eta$.

The opposite approach (e.g., the RANS) is based on the modeling of the full spectrum presented in Fig. 5. It means that (3D) turbulent fluctuations are not explicitly simulated, the effect of turbulence is simply mimicked by adding an extra diffusion to any transported variable. The grid has to be fine enough to capture gradients of the mean flow, which is far less demanding than DNS. Thanks to this feature, the RANS approach is widely used in engineering applications, where the interest is focused on the time averaged flow properties. More details on these two approaches can be found in textbooks, such as [61] and [66].

3.5.1 Reynolds averaged Navier-Stokes (RANS) model

The RANS methodology is focused on the mean flow and the effects of turbulence on mean flow properties [66]. In order to obtain an equation for the mean flow, Reynolds decomposition is applied to the Navier-Stokes equations. The vector and scalar fields are decomposed into a mean and a fluctuation component. The instantaneous velocity U_i, pressure P, temperature T, and density ρ can then be written as

$$U_i = \langle U_i \rangle + u_i^{'}, \tag{3.17}$$

$$P = \langle P \rangle + p^{'}, \tag{3.18}$$

$$T = \langle T \rangle + T^{'}, \tag{3.19}$$

$$\rho = \langle \rho \rangle + \rho^{'}, \tag{3.20}$$

where: $\langle\cdot\rangle$ express the mean component and $(\cdot)^{'}$ is the fluctuation component.

Applying the Reynolds decomposition to the Navier-Stokes equations, the Reynolds Averaged Navier Stokes equations (RANS) are obtained. The RANS equations for continuity, momentum, and scalar conservation are described by

$$\frac{\partial\langle U_i\rangle}{\partial x_i} = 0, \tag{3.21}$$

$$\frac{\partial\langle U_i\rangle}{\partial t} + \langle U_j\rangle\frac{\partial\langle U_i\rangle}{\partial x_j} = -\frac{1}{\rho}\frac{\partial\langle P\rangle}{\partial x_i} + \nu\frac{\partial^2\langle U_i\rangle}{\partial {x_j}^2} - \frac{\partial\langle u_i^{'}u_j^{'}\rangle}{\partial x_j}, \tag{3.22}$$

$$\frac{\partial\langle T\rangle}{\partial t} + \frac{\partial\langle U_j\rangle\langle T\rangle}{\partial x_j} = \frac{\nu}{Pr}\frac{\partial^2\langle T\rangle}{\partial {x_j}^2} - \frac{\partial\langle u_j^{'}T^{'}\rangle}{\partial x_j}. \tag{3.23}$$

The decomposition leads to additional terms in the momentum and scalar conservation equations. The newly appeared $\langle u_i^{'}u_j^{'}\rangle$and $\langle u_j^{'}T^{'}\rangle$ are named as the Reynolds stresses and turbulent heat flux. The Reynolds equations are not closed due to the Reynolds-stress term; a closure is required in terms of known flow parameters. Thus, additional equations are required to solve.

3.5.2 Wall-bounded turbulent flows

A brief overview of different terms used in wall flows is given. As the flow in rod bundles is affected by the gap region, the effect of the wall is very important. For a fully developed channel flow, the total shear stress, τ, is the sum of viscous stress, $\rho\nu\frac{d\langle u_i\rangle}{dx_j}$, and Reynolds-stress $-\rho\langle {u_i}^{'}{u_j}^{'}\rangle$.

$$\tau = \rho\nu\frac{d\langle u_i\rangle}{dx_j} - \rho\langle {u_i}^{'}{u_j}^{'}\rangle. \tag{3.24}$$

At the wall, $u_i = 0$, hence the Reynolds-stress goes to zero. Therefore, the viscous stress is the only contribution to the wall shear-stress (τ_w), given by

$$\tau_w = \rho\nu(\frac{d\langle u_i\rangle}{dy})_{y=0}, \tag{3.25}$$

where u_i is the streamwise velocity and y the wall-normal direction. The viscous velocity scale - u_τ and length scale - δ_τ are defined as the following:

$$u_\tau = \sqrt{\frac{\tau_w}{\rho}}, \tag{3.26}$$

$$\delta_\tau{}^+ = \frac{\nu}{u_\tau}. \tag{3.27}$$

On basis of the above defined velocity and length scales, the friction Reynolds number $Re_\tau$is defined as

$$Re_\tau = \frac{u_\tau \delta}{\nu}, \tag{3.28}$$

where: δ is the half width of the channel. The distance from the wall is measured in terms of wall units, y^+. It is given by

$$y^+ = \frac{u_\tau y}{\nu}. \tag{3.29}$$

Von Kármán [67] proposed that the average velocity of a turbulent flow at a certain point is proportional to the logarithm of the distance from that point to the wall. This is known as the law of the wall. In the viscous sub-layer in the region $0 < y^+ \leq 5$, the shear stress is dominant and the velocity is proportional to the wall distance as below:

$$u^+ = \begin{cases} y^+ & , \ 0 < y^+ \leqslant 5 \quad \text{(viscous sublayer)}, \\ \frac{1}{\kappa} \cdot ln(y^+) + C^+ & , \ y^+ > 30 \qquad \text{(log-law-region)}, \end{cases} \tag{3.30}$$

where: $\kappa \approx 0.41$ - von Kármán constant, $C^+ \approx 5.0$ - wall function constant, y^+ - dimensional wall distance (eq. 3.29).

$$u^+ = \frac{u}{u_\tau}, \tag{3.31}$$

u^+ is the dimensionless velocity.

With this assumption it is possible to model the velocity gradient in those regions without applying a full mesh resolution in this region. The law of the wall is valid for fully developed turbulent flow that is mainly parallel to a hydraulically smooth wall. The velocity gradient in stagnation flow cannot be predicted by this model. Figure 6 (source: Wikipedia, available at: `https://en.wikipedia.org/wiki/Law_of_the_wall`, accessed: 10 June 2022, CC BY-SA 3.0) shows the velocity distribution as function of the wall distance.

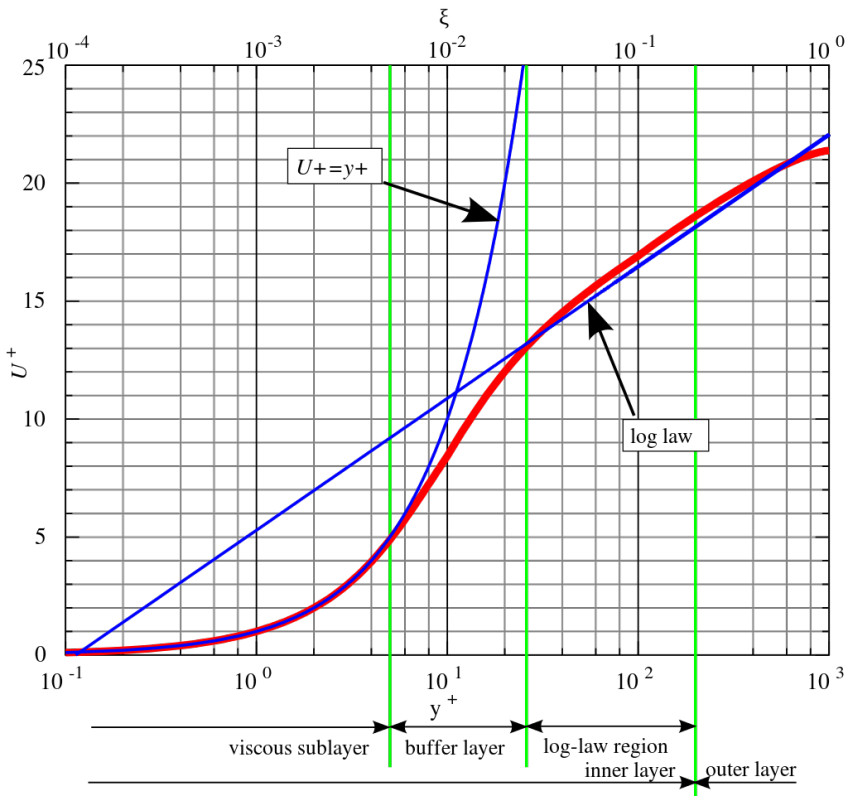

Figure 6: Dimensionless velocity u^+ as function of the wall distance y^+ (source: Wikipedia).

Table 1, constructed from [61], shows the different wall regions defined on the basis of wall units and the corresponding property there, where ${u_i}^+ = \langle u_i \rangle / u_\tau$.

Table 1: Wall regions.

Region	**Location**	**Property**
Inner layer	$y/\delta < 0.1$	$\langle u_i \rangle$ determined by u_τ and y^+, independent of bulk velocity and δ
Viscous wall region	$y^+ < 50$	Significant viscous contribution to total shear stress
Viscous sublayer	$y^+ < 5$	Reynolds shear-stress is negligible compared to viscous stress
Outer layer	$y^+ > 50$	Negligible effects of viscosity on mean flow
Overlap region	$y^+ > 50$, $y/\delta < 0.1$	Region of overlap between inner and outer layers
Log-law region	$y^+ > 30$, $y/\delta < 0.3$	${u_i}^+ = f(ln(y^+))$
Buffer layer	$5 < y^+ < 30$	Transition region between viscosity dominated and inertia dominated parts

3.5.3 Boussinesq Approach vs. Reynolds Stress Transport Models

The Reynolds stresses terms in the Reynolds averaged Navier-Stokes equations can be determined either via a model based on turbulence viscosity hypothesis/Boussinesq hypothesis or modelled directly (Reynolds Stress Model) [61].

In the Boussinesq hypothesis (proposed by Boussinesq in 1877), the Reynolds stresses are proportional to the mean rate of deformation [66], namely, the mean strain rate can be written as:

$$-\langle u_i^{'} u_j^{'} \rangle = \mu_t \left(\frac{\partial \langle U_i \rangle}{\partial x_j} + \frac{\partial \langle U_j \rangle}{\partial x_i}\right) - \frac{2}{3} k \delta_{ij}. \tag{3.32}$$

The Boussinesq hypothesis is used in the Spalart-Allmaras model, the $k-\varepsilon$ models, and the $k-\omega$ models. The advantage of this approach is the relatively low computational cost associated with the computation of the turbulent viscosity, μ_t. In the case of the Spalart-Allmaras model, only one additional transport equation (representing turbulent viscosity) is solved. In the case of the $k-\varepsilon$ and $k-\omega$ models, two additional transport equations (for the turbulence kinetic energy, k, and either the turbulence

dissipation rate, ε, or the specific dissipation rate, ω) are solved, and μ_t is computed as a function of k and ε or k and ω. The disadvantage of the Boussinesq hypothesis as presented is that it assumes that μ_t is an isotropic scalar quantity, which is not strictly true. However, the assumption of an isotropic turbulent viscosity typically works well for shear flows dominated by only one of the turbulent shear stresses. This covers many technical flows, such as wall boundary layers, mixing layers, jets, and so on.

The alternative approach, embodied in the Reynolds Stresses Model (RSM), is to solve transport equations for each of the terms in the Reynolds stress tensor. An additional scale-determining equation (normally for ε or ω) is also required. This means that five additional transport equations are required in 2D flows and seven additional transport equations must be solved in 3D.

In many cases, models based on the Boussinesq hypothesis perform very well, and the additional computational expense of the Reynolds stress model is not justified. However, the RSM is clearly superior in situations where the anisotropy of turbulence has a dominant effect on the mean flow. Such cases include highly swirling flows and stress-driven secondary flows.

In Section 6 different turbulent models will be thoroughly validated. Results obtained with different turbulence models will be compared with the reference DNS results as well as among each other. It will allow to assess the prediction capabilities of the gap vortex street formation and turbulent heat flux in the tightly packed bare rod bundles. A general description of the different types of RANS turbulent models is given in section 3.5.4.

3.5.4 Turbulence models

In practice, the RANS equations can be solved in two regimes:

1. steady;

2. unsteady.

In the steady RANS, the time dependent terms are not included, and it is useful for flows which do not contain any temporal dynamics. The unsteady RANS or URANS, on the other hand, solves the complete RANS equations including the time-dependent terms. In cases of wall resolved flows, the size of the mesh is very small close to the wall, and therefore small time-steps of the order of $10^{-3} - 10^{-5}$ s are required. This makes URANS computationally more expensive than steady-RANS, but still remains less expensive than DNS.

There exist different approaches to obtain a closure relationship for the Reynolds stresses. They can be roughly divided into the following three types:

1. based on the linear eddy-viscosity hypothesis;

2. based on the non-linear eddy-viscosity hypothesis;

3. solving equations for each Reynolds stress.

Linear eddy viscosity models

These are turbulence models in which the Reynolds stresses, as obtained from a Reynolds averaging of the Navier-Stokes equations, are modelled by a linear constitutive relationship with the mean flow straining field, as:

$$-\rho\langle u_i^{'} u_j^{'}\rangle = 2\mu_t S_{ij} - \frac{2}{3}\rho k\delta_{ij}, \tag{3.33}$$

where: μ_t - is the coefficient termed turbulence "viscosity" (also called the eddy viscosity);
$k = \frac{1}{2}(\langle u_1 u_1\rangle + \langle u_2 u_2\rangle + \langle u_3 u_3\rangle)$ - is the mean turbulent kinetic energy;
$S_{ij} = \frac{1}{2}[\frac{\partial U_i}{\partial x_j} + \frac{\partial U_j}{\partial x_i}] - \frac{1}{3}\frac{\partial U_k}{\partial x_k}\delta_{ij}$ - is the mean strain rate.

Non-linear eddy viscosity models

This is class of turbulence models for the RANS equations in which an

eddy viscosity coefficient is used to relate the mean turbulence field to the mean velocity field, however in a nonlinear relationship

$$-\rho\langle u_i^{'} u_j^{'}\rangle = 2\mu_t \mathcal{F}_{nl}(S_{ij}, \Omega_{ij}, \ldots), \tag{3.34}$$

where: $\mathcal{F}_{nl}$ is a nonlinear function possibly dependent on the mean strain and vorticity fields or even other turbulence variable;
$k = \frac{1}{2}(\langle u_1 u_1\rangle + \langle u_2 u_2\rangle + \langle u_3 u_3\rangle)$ - is the mean turbulent kinetic energy;
$\Omega_{ij} = \frac{1}{2}[\frac{\partial U_i}{\partial x_j} - \frac{\partial U_j}{\partial x_i}]$ - is the mean vorticity.

Reynolds Stress Model (RSM)

This is class of turbulence models for The Reynolds Stress Models (RSM), also known as the Reynolds Stress Transport Models, which are higher level turbulence closures, and represent the most complete classical turbulence model. The method of closure employed is usually called a Second Order Closure. In Reynolds Stress Models, the eddy viscosity approach is avoided and the individual components of the Reynolds stress tensor are directly computed. These models rely on the exact Reynolds stress transport equation. They are able to account for complex interactions in turbulent flow fields, such as the directional effects of the Reynolds stresses.

The Reynolds stress model involves calculation of the individual Reynolds stresses, $\rho\overline{u_i' u_j'}$, using differential transport equations. The individual Reynolds stresses are then used to obtain closure of the Reynolds-averaged momentum equation.

The exact transport equations for the transport of the Reynolds stresses, $\overline{u_i' u_j'}$, may be written as follows:

$$
\begin{aligned}
\frac{\partial}{\partial t}(\rho\overline{u_i'u_j'}) + \frac{\partial}{\partial x_k}(\rho u_k\overline{u_i'u_j'}) = \; & \frac{\partial}{\partial x_k}[\rho\overline{u_i'u_j'u_k'} + \overline{p'(\delta_{kj}u_i' + \delta_{ik}u_j')}] \\
& + \frac{\partial}{\partial x_k}[\mu\frac{\partial}{\partial x_k}(\overline{u_i'u_j'})] \\
& - \rho(\overline{u_i'u_k'}\frac{\partial u_j}{\partial x_k} + \overline{u_j'u_k'}\frac{\partial u_i}{\partial x_k}) \\
& + \overline{p'(\frac{\partial u_i'}{\partial x_j} + \frac{\partial u_j'}{\partial x_i})} \\
& - 2\mu\overline{\frac{\partial u_i'}{\partial x_k}\frac{\partial u_j'}{\partial x_k}} \\
& - 2\rho\Omega_k(\overline{u_j'u_m'}\varepsilon_{ikm} + \overline{u_i'u_m'}\varepsilon_{jkm})
\end{aligned}
\tag{3.35}
$$

or

$$
\begin{aligned}
\text{Local time derivative} + C_{ij} = \; & D_{T,ij} \\
& + D_{L,ij} \\
& + P_{ij} \\
& + \phi_{ij} \\
& - \varepsilon_{ij} \\
& + F_{ij}
\end{aligned}
\tag{3.36}
$$

where: C_{ij} is the Convection-Term, $D_{T,ij}$ equals the Turbulent Diffusion, $D_{L,ij}$ stands for the Molecular Diffusion, P_{ij} is the term for Stress Production, ϕ_{ij} is for the Pressure Strain, ε_{ij} stands for the Dissipation and F_{ij} is the Production by System Rotation.

The following terms, $C_{ij}, D_{L,ij}, P_{ij}$ and F_{ij} do not require modelling. However, $D_{T,ij}, \phi_{ij}$, and ε_{ij} have to be modelled for closing the equations. The fidelity of the Reynolds stress model depends on the accuracy of the models for the turbulent transport, the pressure-strain correlation and the dissipation terms.

The turbulence theory included in the section is very brief. More details can be found in several textbooks, for instance [61,62,66]. Some other turbulent models used in this thesis will not be presented in details. All the specific information can be found in given references. In the thesis, the following turbulence models are considered:

- **Linear eddy viscosity models:**
  - Realizable $k-\varepsilon$ ([68]) (hereafter **RKE**)
    with Menter-Lechner Near-Wall Treatment
  - Shear-Stress Transport $k-\omega$ ([69]) (hereafter **SST** $k-\omega$)
    with Corner Flow Correction option
  - Generalized $k-\omega$ ([70]) (hereafter **GEKO**)
    with Corner Flow Correction option
- **Non-linear eddy viscosity model**
  - $k-\varepsilon$ based model (hereafter **RG EASM**)
    with Enhanced Near-Wall Treatment
  - $k-\omega$ based model ([71])(hereafter **WJ-BSL-EARSM**)
    with GEKO option
- **Reynolds Stress Model** ([72–74])
  - Stress-BSL formulation (hereafter **RSM**)
    with GEKO option

None of the applied turbulence models have been tuned for a particular case of a turbulent flow in a bare rod bundle configuration. All the selected turbulence models have been used in the low Reynolds formulation, which means that the equations are solved up to the wall. ANSYS Fluent commercial software used to preform all the RANS type simulations provides many additional options for different turbulence models. However if not mentioned above only the default options for every model have been applied in the present study. The detailed description of turbulence models implementation in the use code can be found in [70, 75–77].

4 Design of a numerical experiment

In this section the design of a numerical experiment for a tight lattice bare rod bundle case is described. In the calibration procedure the set of the precursor RANS and URANS simulations were performed. As a result the optimal setup by means of geometrical configuration and boundary conditions for targeted DNS simulation was defined.

4.1 The Hooper case

As a starting point, Hooper′s hydraulic experiment [23, 25] of a bare rod-bundle is selected, hereafter it will be called as the **Hooper case**. For the sake of understanding some of the key parameters of the Hooper case are recalled here. The cross-section of the Hooper case, which consists of six rods arranged in a square configuration, is shown in Figure 7.

The diameter (D) of the rod is 14 cm and the pitch (P) between the two rods is 15.5 cm. Accordingly, the pitch-to-diameter ratio (P/D) of the considered case is 1.107, which makes itself a close-spaced rod bundle. The streamwise length of the test section is 9.14 m, which is equivalent to 128 hydraulic diameters. Air at room temperature was used as a working fluid for the Hooper case [23]. The bulk Reynolds number of the selected configuration is $Re_b \approx 49000$, which corresponds to the mean axial inlet velocity of 10.3 m/s. Performing a DNS of the Hooper case requires a huge amount of computational power. An initial mesh estimation of this case was performed (based on the obtained URANS results) and it would require a total of 14 billion grid points only for the flow field to perform a true DNS. Furthermore, additional constraints with respect to the simulation time-step etc. would make this DNS not feasible in the near future. Hence, a calibration of the Hooper case is performed to optimize the flow configuration in such a way that it preserves the essence of the Hooper experiment, i.e. the gap vortex street formation. Moreover, it will also

allow introducing the thermal field, which was not included in the Hooper case.

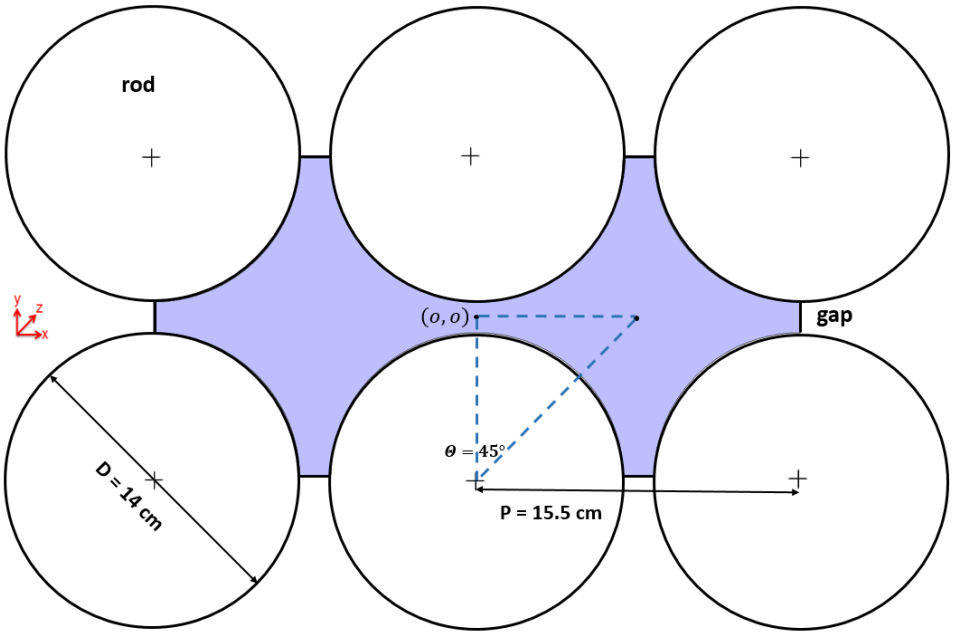

Figure 7: Cross section of the Hooper's hydraulic experiment of a tight lattice rod-bundle (based on [25]).

4.2 Numerical Methodology

4.2.1 Computational domain and boundary conditions

In the recent past, a number of attempts have been made by the researchers to numerically replicate and/or study the Hooper case [3, 18]. In these studies, the cross-section of the considered computational domain was reduced by only taking into account the narrowest gap between the rods, as highlighted in Figure 8. Further breaking-down of this domain (also shown in Figure 8) indicates that it consist of four primary flow cells. Nevertheless, authors of mentioned numerical studies were able to reproduce the appearing axial flow pulsations. However, recently [3] it was found out that for high fidelity type simulations (such as LES or DNS), this reduced cross-sectional domain of the Hooper case is not sufficient and may lead to unwanted numerical errors. This point is also highlighted by several

other high fidelity numerical simulations for different rod bundle configurations [52] and [78]. Hence, to avoid such unwanted numerical errors, the complete/full cross-sectional domain of the Hooper case is considered; this also includes the side walls (as highlighted in Figure 9).

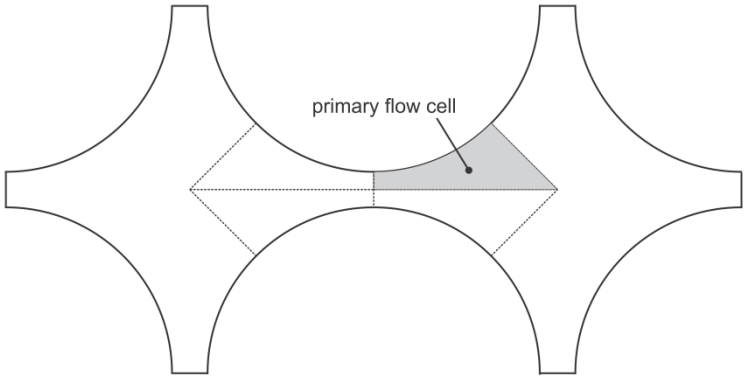

Figure 8: Cross-section of the Hooper case – the dashed lines represent the selected region for the previous CFD numerical analysis.

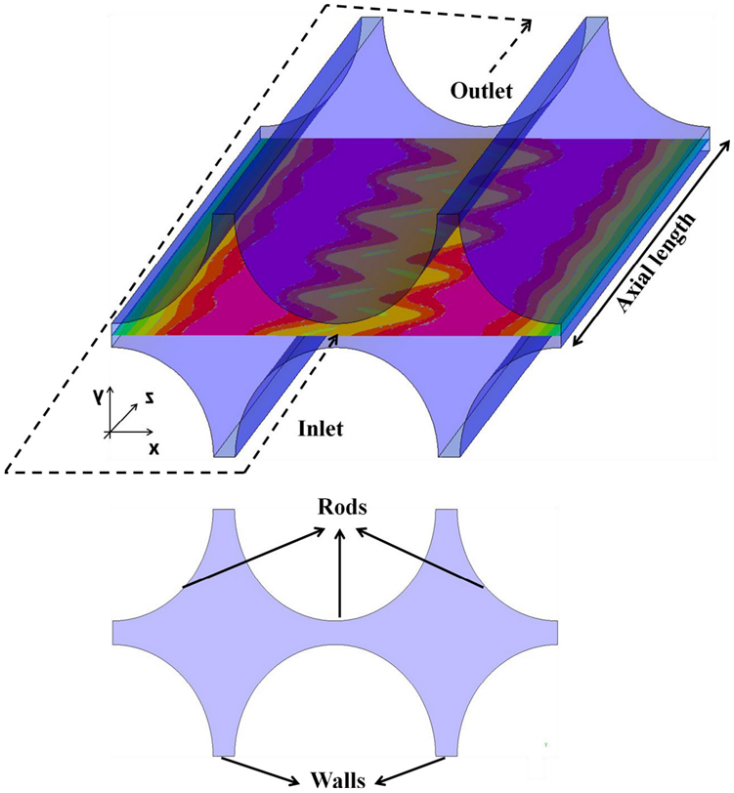

Figure 9: Computational domain corresponding to the Hooper case.

It is worthwhile to remind that the Hooper experiment was realized

with the application of a classical inlet-outlet boundary conditions and the corresponding streamwise length of the domain was 9.14 m. However, for the targeted DNS a periodic boundary conditions are imposed, which is indeed preferable to sustain the turbulence level. In addition, it will also allow the provision to reduce the computational domain and eventually the overall computational cost. Hence, for the present calibration study, a periodic boundary condition is employed by imposing a constant mass flow rate of 0.213 kg/s, which corresponds to the Reynolds number of 49 000. A list of other considered mass flow rates are given in Section 4.3.1. Moreover on the rods, a non-slip condition is used along the two different thermal boundary conditions, which are explicitly mentioned and discussed in Section 4.3.3. This selected computational domain along with the boundary conditions is given in Figure 9.

4.2.2 CFD Solver

The commercial software ANSYS Fluent version 17.2.0 [79] is selected to perform this calibration and optimization study. Since the design of the Hooper case would require a series of pre-cursor unsteady computations, the URANS turbulence modelling approach is considered and a linear SST $k-\omega$ model [69] is selected in this regard. With respect to the numerical schemes, a second order upwind scheme is used for the momentum and energy equations. The least square cell based scheme is used for gradients. This spatial discretization is performed by using a pressure-velocity coupling method combined with a SIMPLE-scheme algorithm. Moreover, a pressure-based solver is considered, which employs a second order pressure interpolation scheme. Lastly, for the temporal discretization, a second order implicit scheme available in the code ANSYS Fluent is selected. It is worth mentioning that for all the URANS computations presented in this article, the CFL (Courant-Fridrichs-Lewy) number is always kept less than 1 with 30 sub-iterations per time step. CFL - the convergence condi-

tion by Courant–Friedrichs–Lewy is a necessary condition for convergence while solving certain partial differential equations numerically. The CFL condition has the following form:

$$C = \frac{u\Delta t}{\Delta x} \leqslant C_{max}, \tag{4.1}$$

where the dimensionless number C is called the Courant number, u is the magnitude of the velocity, Δt is the time step, Δx is the characteristic length.

In total, 22 test cases of URANS computations are performed for this research work and each simulation has run for an average 0.3 million iterations. All the simulations are performed on the CIŚ (Świerk Computing Centre) [2] at the National Centre for Nuclear Research (NCBJ), Poland, by using an average of 130 processors. A total computational time of ~ 0.3 million core hours is used to perform this work.

4.2.3 Meshing strategy

The commercial software ANSYS Meshing version 17.2.0 [80] is used to generate meshes for the precursor simulations. A hexahedral meshing strategy is employed to generate the mesh. In this regard, a two-step approach is employed to generate the mesh, that is:

Step 1. A 2D mesh for the cross-section is generated, as shown in Fig. 10.

Step 2. Afterwards, this 2D mesh is uniformly extruded in the streamwise direction.

As mentioned previously that the calibration and optimization of the Hooper case involve a wide range of URANS computations, varying the Reynolds number and other geometric parameters, hence it is not optimum to perform the mesh sensitivity study at the forehand. Nevertheless, an

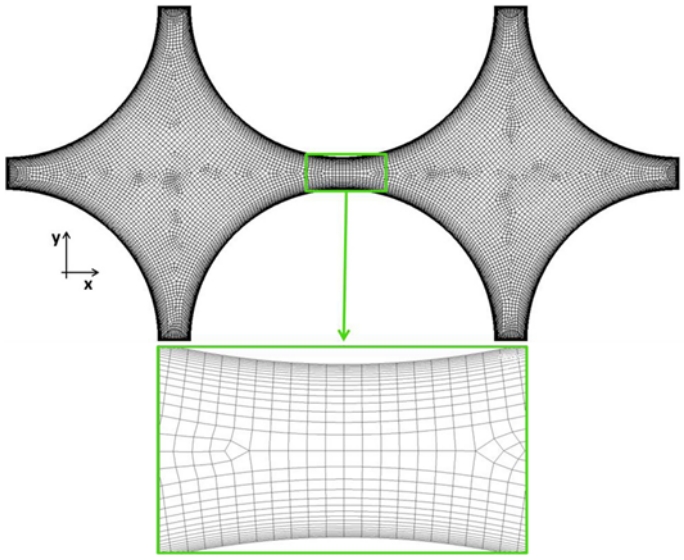

Figure 10: Computational mesh.

initial mesh is generated, which has to be good enough to correctly reproduce the overall flow features appearing in all considered test cases. This initial mesh is generated corresponding to the original Hooper case and it consists of 6.8 million grid points. The mesh includes a structured mesh boundary layer (16 grid points with a stretching ratio of 1.2) in the near wall region in order to better capture the flow gradients. The size of the first cell was computed such that the value of average y^+ is kept below 1 (y^+ represents the normalized distance from the nearest wall in the wall units and is defined as given in equation 3.29). This mesh is sufficiently fine to capture the appearing flow fields in considered flow configurations, which is also confirmed in the mesh sensitivity study reported in Section 4.5.

4.3 Calibration and optimization of the rod bundle

A series of test cases are performed in three steps in order to calibrate and optimize the Hooper case, i.e.:

Step 1. Scaling of the Reynolds number.

Step 2. Optimization of the computational domain.

Step 3. Introduction of the thermal fields.

These steps are explicitly discussed in the following sections.

4.3.1 Scaling of the Reynolds number

The first calibration is related to the scaling of the Reynolds number, more precisely the scaling-down of the Reynolds number is the goal here. As mentioned earlier, performing a DNS of the Hooper case with original flow parameters is not feasible and foreseeable in the near future. Hence, following the work of Shams et al. [81, 82], s scaling-down of the Reynolds number is performed in such a way that the main flow characteristics of the Hooper case are preserved and the flow field remains in the turbulent regime. Accordingly, URANS computations of ten test cases are performed by decreasing the Reynolds number in a systematic way and are given in Table 2. Among the listed test cases, case 1 represents the original Hooper case.

Table 2: List of test cases considered for the scaling of the Reynolds number.

Cases	Nomenclature	Scale down	Re	Mass flow rate [kg/s]
1	**R1**	**R1**	**49 000**	**0.2134**
2	R2	R1/2	24 500	0.1063
3	R3	R1/3	16 333	0.0708
4	R4	R1/4	12 250	0.0531
5	R5	R1/5	9 800	0.0425
6	R6	R1/6	8 167	0.0354
7	R7	R1/7	7 000	0.0304
8	R8	R1/8	6 125	0.0267
9	R9	R1/9	4 083	0.0178
10	R10	R1/10	3 063	0.0134
11	R11	R1/11	1 531	0.0067

For the sake of proper post-processing, two different cross-sectional planes are selected, which are highlighted in Fig. 11. Cross-section plane

represents a xy-plane view and is extracted at the mid length of the computational domain, whereas, streamwise plane is taken in the xz-plane along the streamwise direction to explicitly visualize the appearing gap vortex street in the domain.

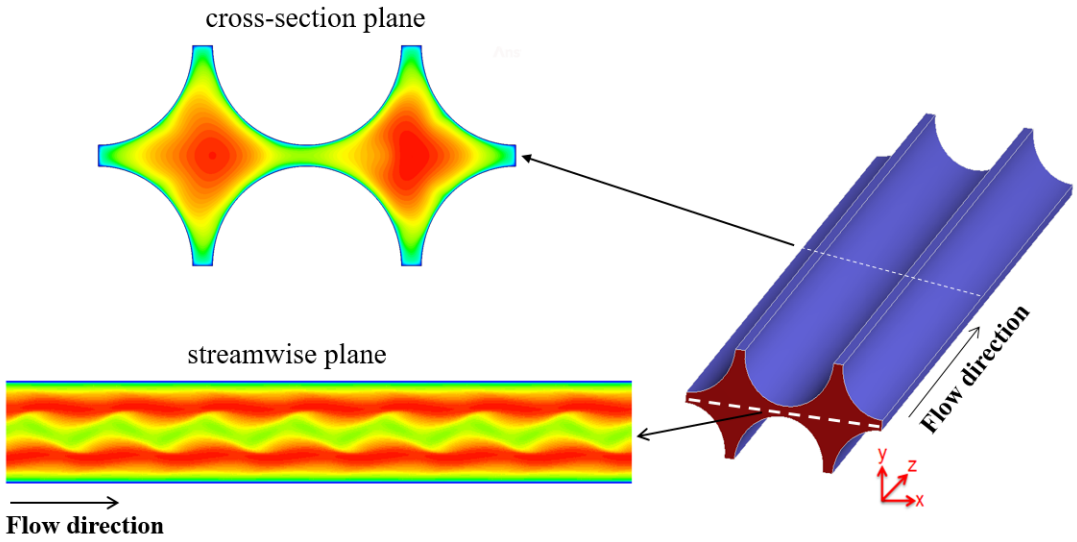

Figure 11: Location of the cross-section and streamwise plane for the post-processing purpose.

Before performing the scaling analyses, it is important to assess the prediction capabilities of the selected numerical method and the turbulence modelling. Hence, the obtained results corresponding to the original Hooper case Reynolds number are (qualitatively and quantitatively) compared with the available experimental data [25]. A qualitative comparison of the obtained velocity signal is shown in Fig. 12. By looking at the comparison, it can be seen that although the obtained numerical results are not exactly the same as the experimental ones (mainly because an isotropic URANS approach is used), the overall flow characteristics are correctly reproduced.

Particularly, a similar number of axial flow pulsations are captured by the numerical results. An average cycle frequency (f) of these flow pulsations is computed using the power spectral density (PSD), and is presented in Fig. 13. The PSD of the URANS results display a prominent frequency

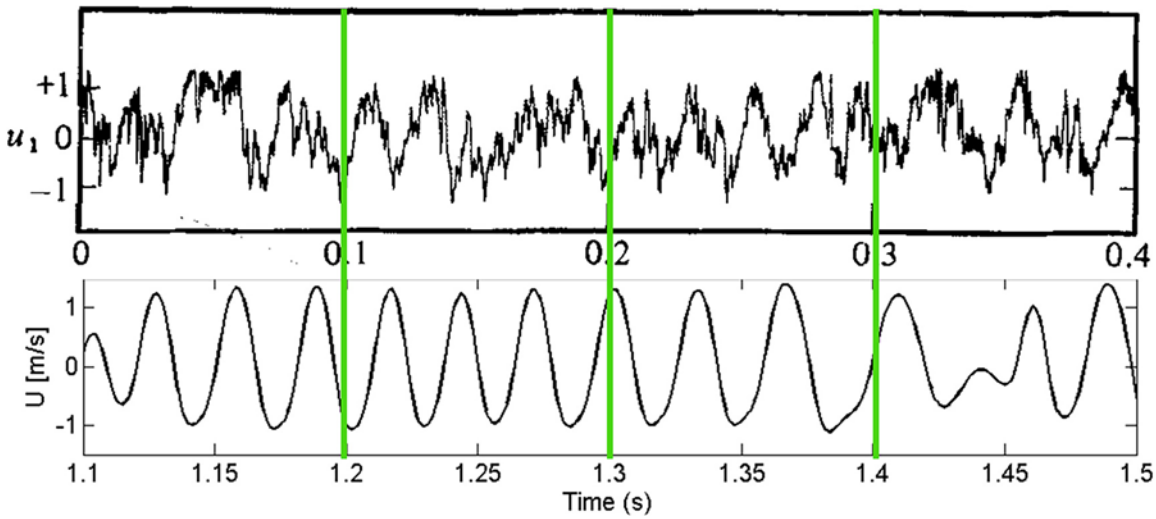

Figure 12: Comparison of the URANS (bottom) reproduction of flow pulsations versus the measured (top) turbulent-velocity component u located at the rod-gap centre [25].

of the appearing axial flow pulsations and show a peak around 30 Hz, which is found to be in a good agreement with the experimental data [25]. This suggests that the considered numerical methodology is good enough to reproduce the overall flow pulsations appearing in the Hooper case.

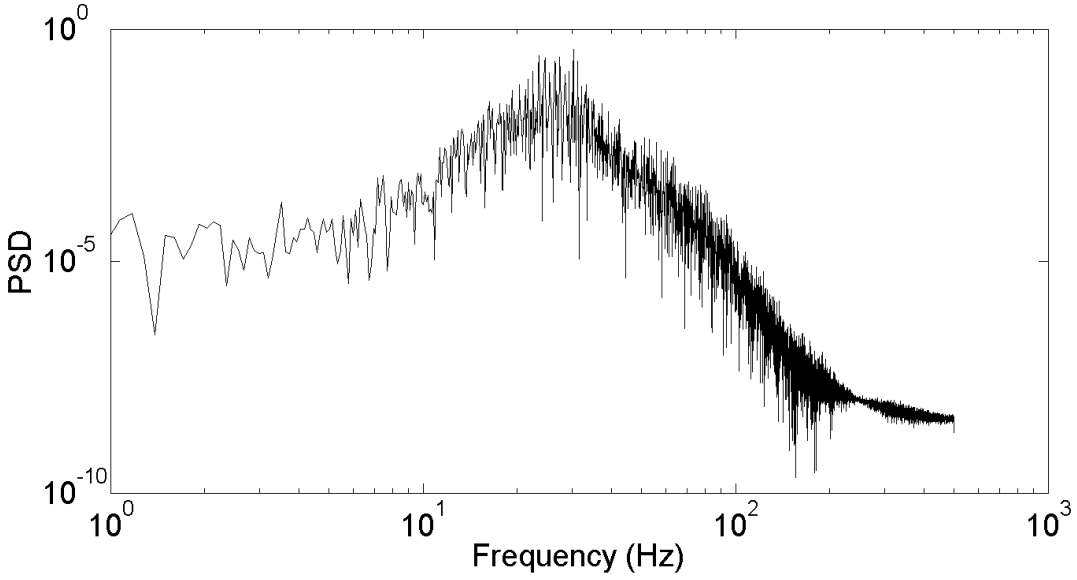

Figure 13: The PSD of analyzed axial velocity fluctuations for Re = 49 000.

Furthermore, Fig. 14 displays the iso-contours of the instantaneous velocity fields obtained from the URANS solutions corresponding to all

eleven Reynolds numbers listed in Table 2. These contours are shown for the streamwise plane (as per Fig. 11) highlighting the axial flow pulsations in the gap region. By looking at the results, it can be seen that for all the considered Reynolds number cases, the overall flow topology of the axial flow pulsations is preserved. Results depict that the flow pulsations in the centerline (narrowest gap) region progressively increase with the decreasing Reynolds number. Particularly, the low-velocity gap region becomes more prominent with the decreasing Reynolds number. The mean cyclic frequency corresponding to all the Reynolds number cases is computed and also compared with the available experimental measurements [25], see Fig. 15. The plot in Fig. 15 illustrates the measured characteristic frequency for a wide range of Reynolds numbers and indicates a linear correlation for a specific P/D ratio. A similar trend is also reproduced by all the performed URANS computations, however, with a slight under-prediction of the pulsation frequency.

It is important to mention that for all the cases, a similar initial condition is used to perform the URANS computations, i.e. first a RANS computation is performed to obtain a fully developed field and subsequently, the URANS computation is performed to observe the gap vortex street. Nonetheless, the exact physical time of the onset of the flow pulsations varies with the Reynolds number. Namely, Fig. 16 clearly shows that with the decreasing Reynolds number, the gap vortex street appearance time exponentially increases and leads to a maximum of 15 sec for the lowest considered Reynolds number. This, in turn, also increases the computational cost. Despite the delay in the appearance of the gap vortex, it is interesting to see that all the cases have shown the appearance of the axial flow pulsations.

To investigate each test case further, the obtained results were compared quantitatively. For the sake of any quantitative comparison presented in this thesis, the results are extracted along three different lines. The exact

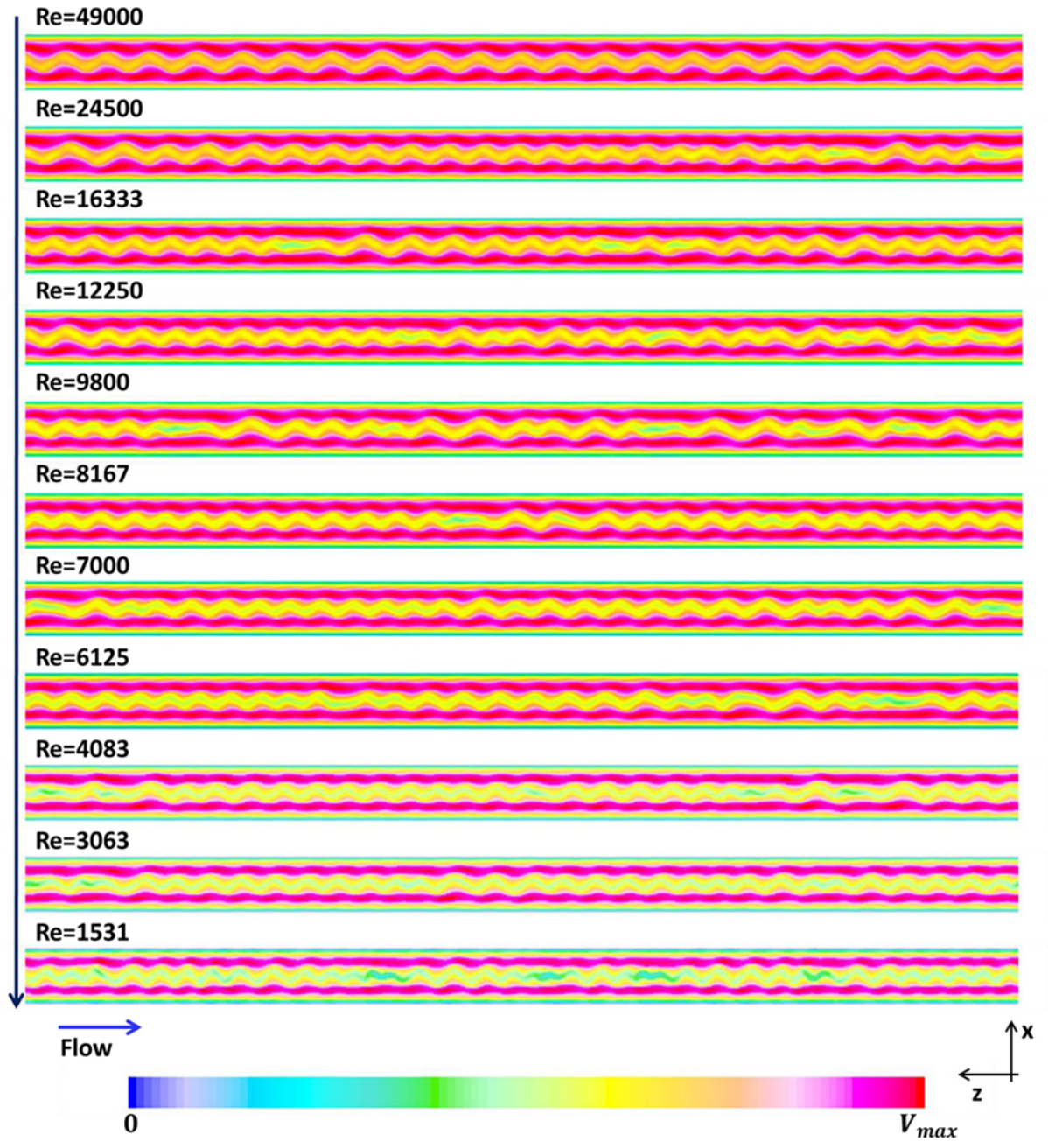

Figure 14: Iso-contours of velocity magnitude for different Reynolds numbers.

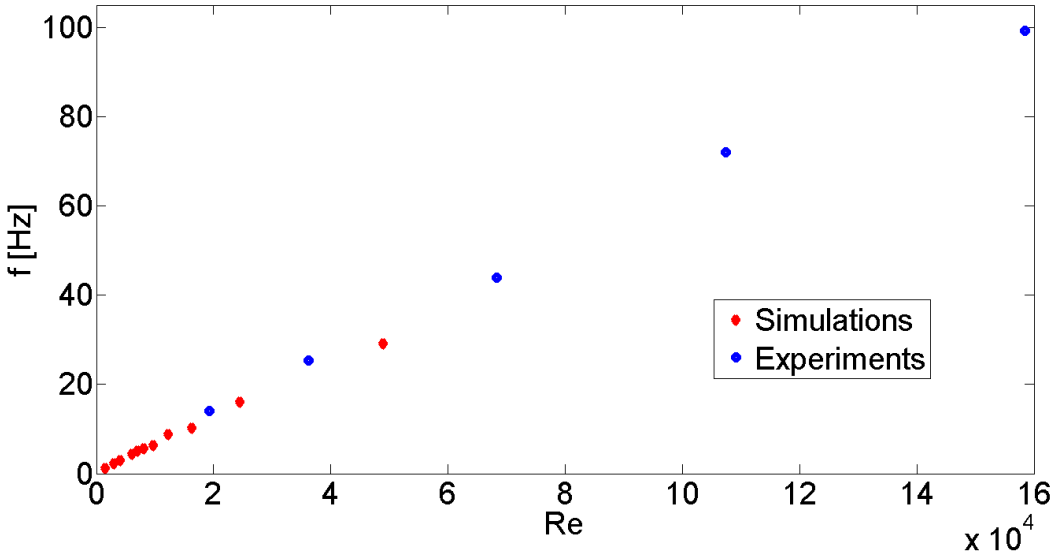

Figure 15: Mean cyclic frequency of large-scale turbulent structure in the open rod gap as a function of Reynolds number - experimental vs numerical results.

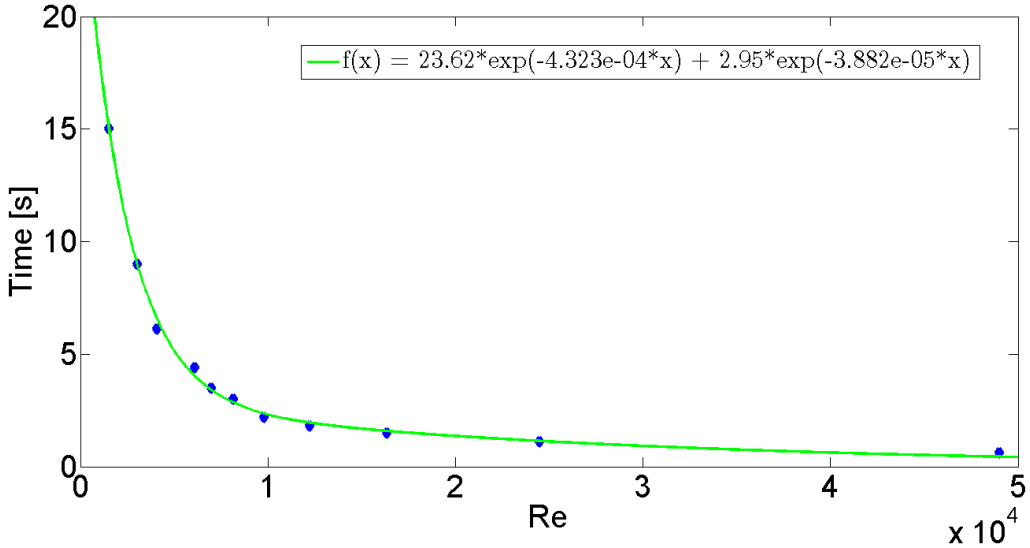

Figure 16: Evolution of the physical time for the appearance of the axial flow pulsations w.r.t. different Reynolds numbers.

location of these lines is shown in Fig. 17. Line 1 (denoted as **L1**) is taken at the mid of the computational domain and highlights the profiles in the narrowest gap region. Line 2 (**L2**) is taken in the mid of xy-plane. Whereas, Line 3 (**L3**) is taken in the diagonal direction to pass through the sub-channel region, where the maximum velocity field appears in the computational domain.

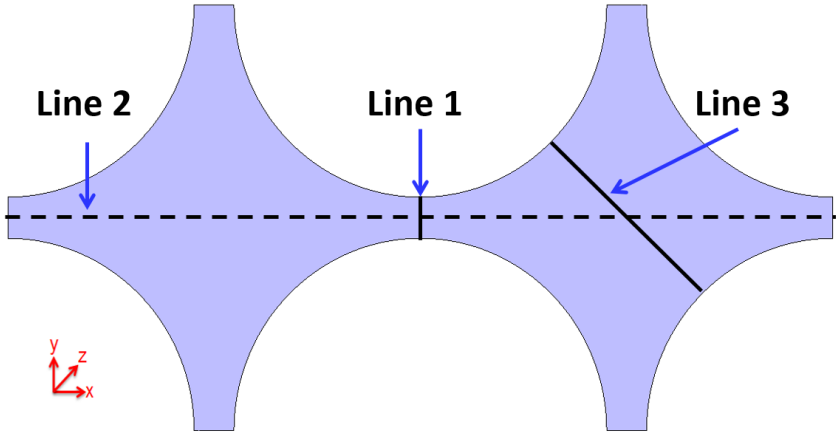

Figure 17: Lines location.

For the comparison purpose, the velocity profiles corresponding to L1 are extracted and given in Fig. 18. In a rod bundle flow, the maximum velocities appear in the center of the sub-channel region, whereas in the gap region, the observed velocities are relatively small. This means that the Reynolds number in the sub-channel region is always higher than in the gap region. Therefore, when the velocity in the gap region is non-dimensionalized with the respective bulk velocity (U_b), the corresponding ratio remains less than one.

Fig. 18 depicts that for the lowest Reynolds number, the flow is laminar and resembles with a typical parabolic profile. For the other two lowest Reynolds number configurations, i.e. $Re = 3063$ and $Re = 4083$, the flow can easily be categorized as laminar or transitional flow regime. However, for the rest of the considered Reynolds numbers, the flow is mostly depict-

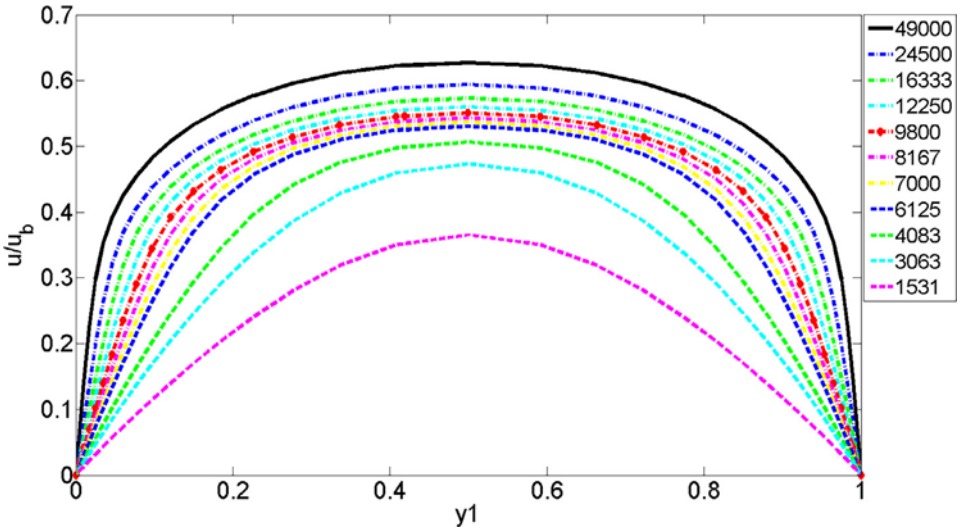

Figure 18: Velocity profiles along Line 1 for different Reynolds numbers [hereafter y1 corresponds to non-dimensionalized L1; y1 is non-dimensionalized by the length of the specific line as follows $y1 = y/y_{max}$].

ing a turbulent profile. With the decreasing Reynolds number, the velocity gradient close to the wall becomes less steep. A gradient of all the velocity profiles, in the wall normal direction, is calculated and given in Fig. 19. It is clearly visible that the lowest Reynolds number displays a linear gradient close to the wall, which is typical for the laminar flow regime. For the other two lowest Re cases, the observed profiles show a hint of an inflexion, nevertheless the flow can easily be categorized as being in laminar or transitional regime. The rest of the cases show clear non-linear trend followed by an inflexion point illustrating a turbulent velocity profile.

The turbulent kinetic energy of all the cases is computed and given in Fig. 20. Once again, for the lowest three Reynolds number cases, similar conclusions can be deduced. Namely, profiles for these Reynolds numbers are typical for the laminar flow regime. Interestingly, the cases R7 and R8 (i.e. $Re = 7000$ and $Re = 6125$) show clear signs of flow being very close to the transition region. It means that the flow regime corresponding to these two Reynolds number could be very sensitive to the prediction capabilities of different RANS models. In the work of Shams et al. [83]

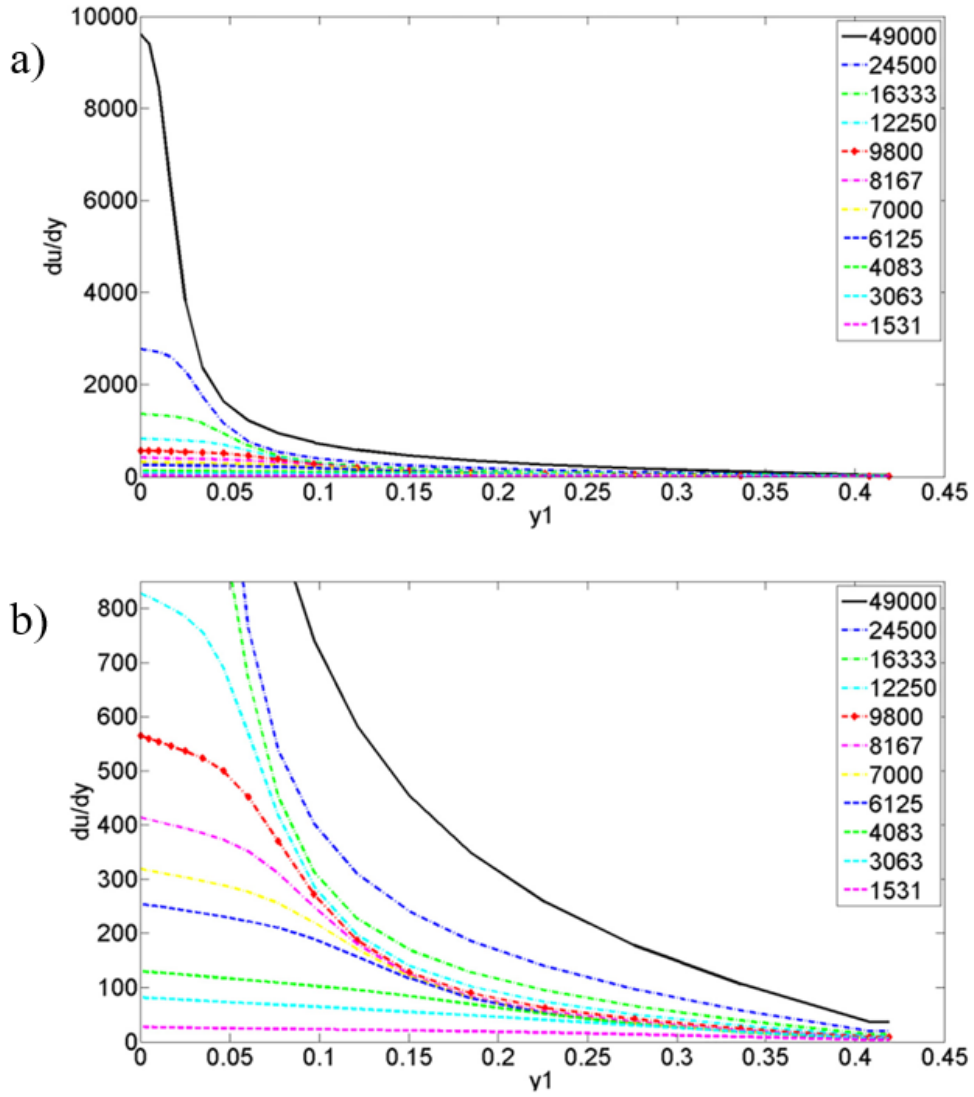

Figure 19: Gradients of the velocity across L1 (till the mid of the gap) for different Reynolds numbers - top *a*), bottom *b*) is a zoom of *a*).

where a low-Reynolds $k-\varepsilon$ model was used to reproduce flow in a turbulent channel flow, it was found out that the flows corresponding to low Reynolds numbers (i.e. close to $Re_\tau = 180$) were very sensitive to the applied model. This issue is also highlighted in the work of Shams et al. [82], however, for a wire-wrapped rod bundle. Hence, it is important to select a Reynolds number which is not sensitive to the RANS model, and consequently should not predict the flow relaminarize while performing the validation study. In that context, as a first step, the friction Reynolds numbers corresponding to all eleven Reynolds numbers are computed and listed in Table 3.

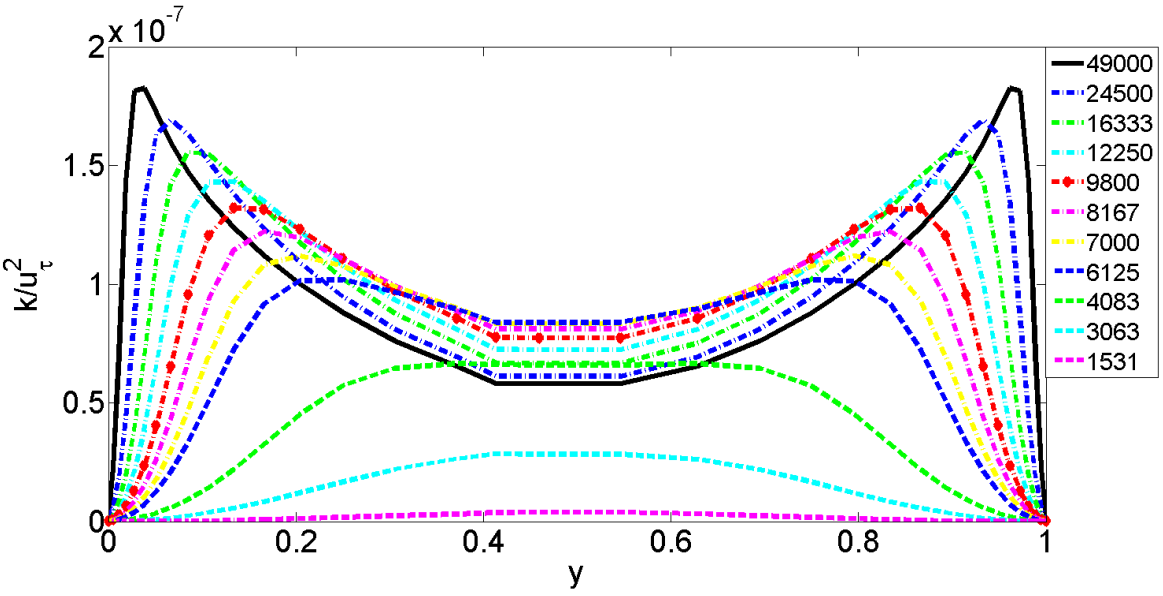

Figure 20: Turbulent kinetic energy profiles along L1 for different Reynolds numbers.

Table 3: Computed friction Reynolds number for the precursor simulations.

Re	R1	R2	R3	R4	R5	R6	R7	R8	R12	R16	R32
Re_τ	1812	973	683	532	439	376	330	295	211	167	100

Table 3 shows that the case R6 (which is also in the turbulent flow regime) corresponds to the friction Reynolds number of 376. This friction Reynolds number (eq. 3.28) is high enough in order not to be sensitive to the RANS models and become relaminarized. Nonetheless, in order to avoid this to happen, an additional URANS study for the R6 case is per-

formed using a linear $k-\varepsilon$ model [84], and the obtained velocity profile for L1 is compared with the SST $k-\omega$ model, see Fig. 21. It is clearly noticeable that for the case R6, this considered $k-\varepsilon$ model is not relaminarizing. Similar turbulent flow profiles were also observed in the work of Chang and Tavoularis [37, 85, 86], where an RNG $k-\varepsilon$ model was used.

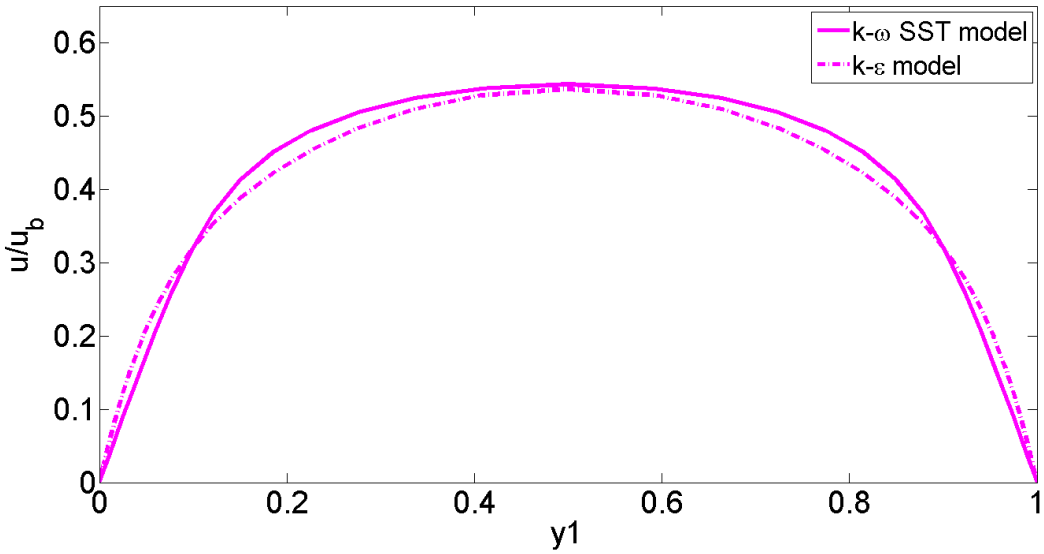

Figure 21: Velocity profiles along L1 for SST $k-\omega$ and $k-\varepsilon$ model for the case R6 (i.e. $Re = 8167$).

It must be acknowledged that the axial flow pulsations have been predicted for the considered rod bundle configuration, irrespective of the laminar, transition or turbulent flow regimes. To the best of author knowledge, this is the first time that the flow pulsations are numerically predicted in a laminar flow regime. These findings are in accordance with the experimental work of Gosset and Tavoularis [32], and Mahmood [87], who have also observed the axial flow pulsations in a laminar flow for a rod bundle configuration. Ramm et al. [88] theoretically predicted the onset and extent of laminarization in infinite square and triangular arrays as a function of bulk Reynolds number and the P/D ratio. In view of the capabilities of the theoretical approach they considered the following criteria to characterize the occurrence of laminarization: $(\overline{\epsilon_{Mr}}/\nu)_{\varphi=0}$, which represents the

gap average value of the eddy diffusivity of momentum in the radial direction normalized by the (molecular) kinematic viscosity. Fig. 22 presents the predicted transition curves based on the criterion $\overline{\epsilon_{Mr}}/\nu = 0.2$, which according to Ramm et al. [88] seems to describe the occurrence of the transition reasonably well. In the present study, a square arrangement of the rod bundle is considered with a P/D = 1.107, hence all the considered Reynolds numbers are also explicitly indicated in Fig. 22.

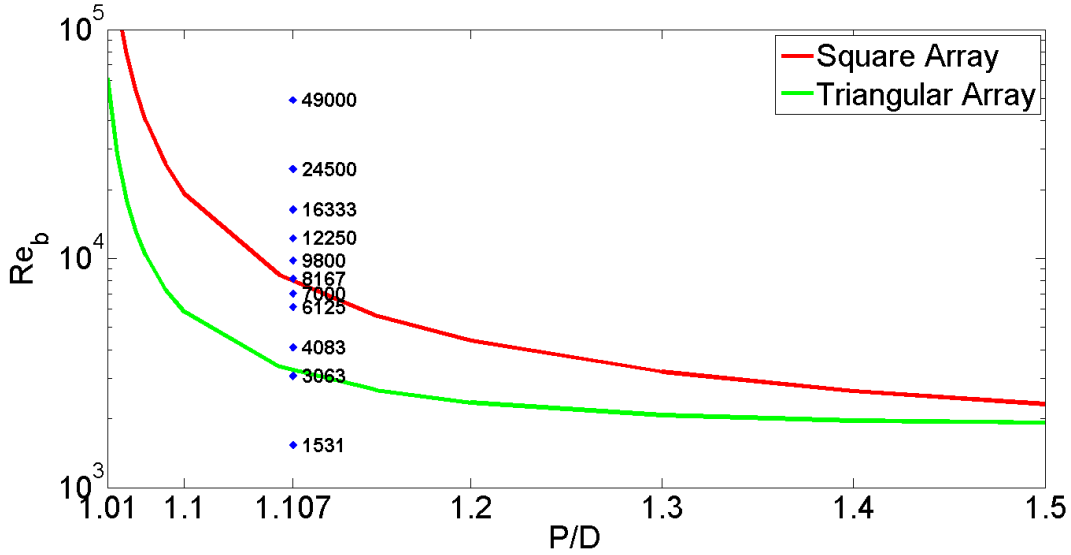

Figure 22: Prediction of the onset and extent of laminarization in infinite triangular and square arrays along with the Hooper case for different Reynolds numbers.

It is noticeable that for the considered flow configuration, Reynolds number above 8000 is clearly turbulent. Hence, to be on the safe side, the case R5 (i.e. Re = 9800) instead of R6 (i.e. Re = 8167) is considered for the targeted DNS computation. However, the feasibility of this Reynolds number has to be checked and is reported in the following sections.

4.3.2 Optimization of the computational domain

In this section, the optimization of the computational domain, particularly the streamwise length of the domain, is performed. In this regard, three additional test cases are computed by reducing the axial length (L $[m]$) of

the domain, i.e. $L/4$, $L/5$, $L/6$. These test cases are listed in Table 4 and the obtained results are presented in Fig. 23.

Table 4: List of test cases considered to optimize the (streamwise) length of the computational domain.

Cases	Re	Length [m]	Mesh [mln]	Mass flow rate [kg/s]
12	9800	2.285	1.7	0.042506
13	9800	1.828	1.35	0.042506
14	9800	1.523	1.13	0.042506

By looking at the iso-contours of the velocity field, it can be noticed that all the considered domains are sufficiently long to reproduce the expected axial flow pulsations. Moreover, the mean cyclic frequencies of all these cases are also computed and shown in Fig. 24.

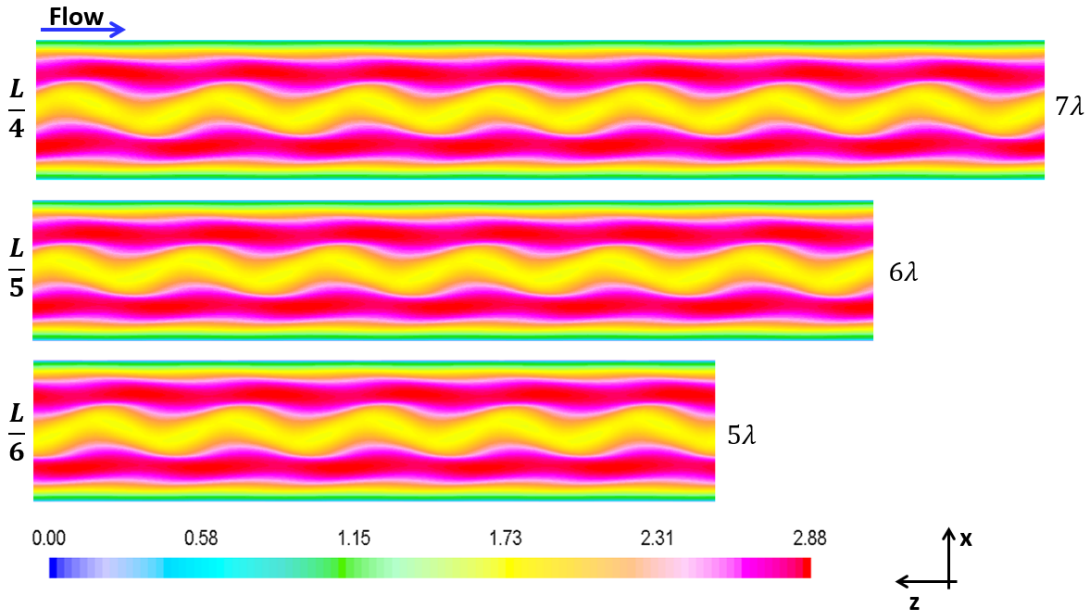

Figure 23: Iso-contours of velocity magnitude for different length of computational domain.

It is clearly noticeable that all the domains are able to predict the same dominant frequency of the axial flow pulsations. This highlights the fact that the considered domains are sufficiently long to reproduce the overall topology of the flow field.

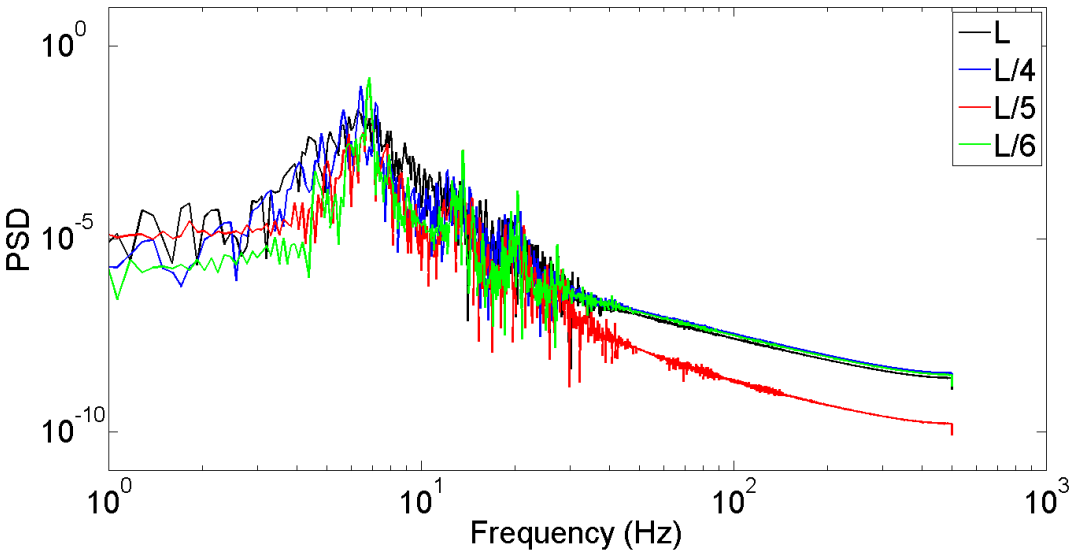

Figure 24: PSD for short domains.

As reported earlier, a periodic boundary condition has been applied in the streamwise direction for the considered computational domain. Accordingly, a two-point correlation is performed for all three computational domains (not presented in this thesis) and it seems that the domain is sufficiently long enough to uncorrelate the influence of the boundary conditions. However, according to [78] the axial (streamwise) length of the domain should be long enough to capture at least four wavelengths (4λ $[m]$) of the appearing gap vortex. Based on the frequency of the gap vortex street predicted for these three cases (see Fig. 24), the axial length of the domain is around 7λ, 6λ, and 5λ for $L/4$, $L/5$ and $L/6$, respectively. From Fig. 24, it can be noticed that these three cases predict the same frequency as the original domain: meaning that appearing axial flow pulsations are not influenced by the considered sizes of the domain. It is worth reminding that the targeted DNS will also include the thermal field analyses. In the work of [89], it was found that for low Prandtl fluids, the computational domains should be somewhat longer than the unity Prandtl fluid cases. Namely, the structures which appear in the low Prandtl fluids are larger than the structures in the unity Prandtl fluids and a domain, which is cal-

ibrated for the unity Prandtl fluid, may induce some numerical errors for low Prandtl flows. Nonetheless, it is important to mention that these errors were mainly observed for second order statistics of the thermal field [89]. By considering all these facts, an axial domain $L/4$, which corresponds to 7λ, is considered for the final DNS computations.

4.3.3 Introduction of the thermal fields

In the work of [40, 41], in addition to the existence of large-scale periodic fluctuations of velocity, fluctuations of temperature were intensively investigated. The authors found that these fluctuations are responsible for the high inter-subchannel heat and momentum exchange. Moreover, in some numerical simulations [37, 85, 86], it was demonstrated that the temperature fluctuations and turbulent kinetic energy increases with a decrease of the gap rod. Apart from that, in the nuclear industry, flow and heat transfer in the rod bundles are usually calculated with a sub-channel approach, in which the temperature, pressure and velocity in a sub-channel are averaged, and one representative thermal-hydraulic condition specifies the state of the sub-channel. Since these sub-channel codes are essentially based on solving one- or two-dimensional equations and are taking into account turbulent interactions between sub-channels by using empirical inter-subchannel mixing coefficients, then, they cannot take into account the complicated heat transfer phenomena and its contribution to the mixing process in the gap region. Therefore, it is important to take into account the thermal aspect of the rod bundle flow and provide a reference database for the validation purpose. Considering the fact the that selected flow configuration is a forced convection flow regime, it allows introduction of the thermal field as a passive scalar. Although in the original Hooper case air was considered as a working fluid, in our case, we make use of passive scalars, and so three different working fluids are selected to study the thermal effects. These passive scalars correspond to four different Prandtl

numbers of air, water at two different temperatures, and liquid sodium, i.e. $Pr = 1, 2, 7$, and 0.025, respectively. In order to thoroughly assess the effect of the thermal field in the final DNS, all four passive scalars are tested here for two different thermal boundary conditions at the surface of the rods, i.e. constant temperature and constant heat flux. In this regard, a total of eight simulations are performed and explicitly listed in Table 5. Periodic heat transfer is possible for both Dirichlet (in thermodynamics this type of boundary condition indicates a situation when a fixed temperature is held on the surface) and Neumann (prescribe heat flux from a surface) boundary conditions [90] and applied to the temperature field.

Table 5: List of test cases considered to introduce the thermal fields.

Cases	**Re**	**Length [m]**	**Mesh [mln]**	**Mass flow rate [kg/s]**	**Pr**	**T [K]**	**Heat flux** $[W/m^2]$
15	9800	2.285	1.7	0.042506	0.025	296	-
16	9800	2.285	1.7	0.042506	1	296	-
17	9800	2.285	1.7	0.042506	2	296	-
18	9800	2.285	1.7	0.042506	7	296	-
19	9800	2.285	1.7	0.042506	0.025	-	0.12
20	9800	2.285	1.7	0.042506	1	-	0.12
21	9800	2.285	1.7	0.042506	2	-	0.12
22	9800	2.285	1.7	0.042506	7	-	0.12

The periodic scaled temperature $\theta(\vec{r})$ is defined as:

$$\theta(\vec{r}) = \frac{T(\vec{r}) - T_w}{T_b(\vec{r}) - T_w} \tag{4.2}$$

where $T(\vec{r})$ $[K]$ is temperature in a certain position $\vec{r}$, T_b $[K]$ is bulk temperature, and T_w $[K]$ is temperature on the wall.

For Dirichlet boundary condition, the scaled temperature can be written as:

$$\frac{T(\vec{r}) - T_w}{T_b(\vec{r}) - T_w} = \frac{T(\vec{r} + \vec{L}) - T_w}{T_b(\vec{r} + \vec{L}) - T_w} = \frac{T(\vec{r} + 2\vec{L}) - T_w}{T_b(\vec{r} + 2\vec{L}) - T_w} = \cdots . \tag{4.3}$$

where $\vec{L}$ is a translation vector.

For Neumann boundary condition, the quantity $T_b - T_w$ is constant across modules. Thus, equation (4.3) can be simplified to:

$$T(\vec{r}) - T_b(\vec{r}) = T(\vec{r}+\vec{L}) - T_b(\vec{r}+\vec{L}) = T(\vec{r}+2\vec{L}) - T_b(\vec{r}+2\vec{L}) = \cdots . \quad (4.4)$$

Here the bulk temperature T_b $[K]$ is defined by the relation:

$$\frac{\iint_A |u_i e_{L,i}| T \, dA}{\iint_A |u_i e_{L,i}| \, dA} = 0 \quad (4.5)$$

where A $[m^2]$ is an area of cross-section, u_i is the $ith-$component of the velocity vector, and $e_{L,i}$ is the $ith-$component of the unity vector $\hat{e}_L$ in the direction $\vec{L}$.

4.3.4 Constant temperature on rods

For the constant temperature boundary condition, a temperature of 295 K has been imposed on rods. Simulations are performed for all four passive scalars and the obtained results are presented for two different planes: in cross-sections and streamwise, in Fig. 25 and 26, respectively.

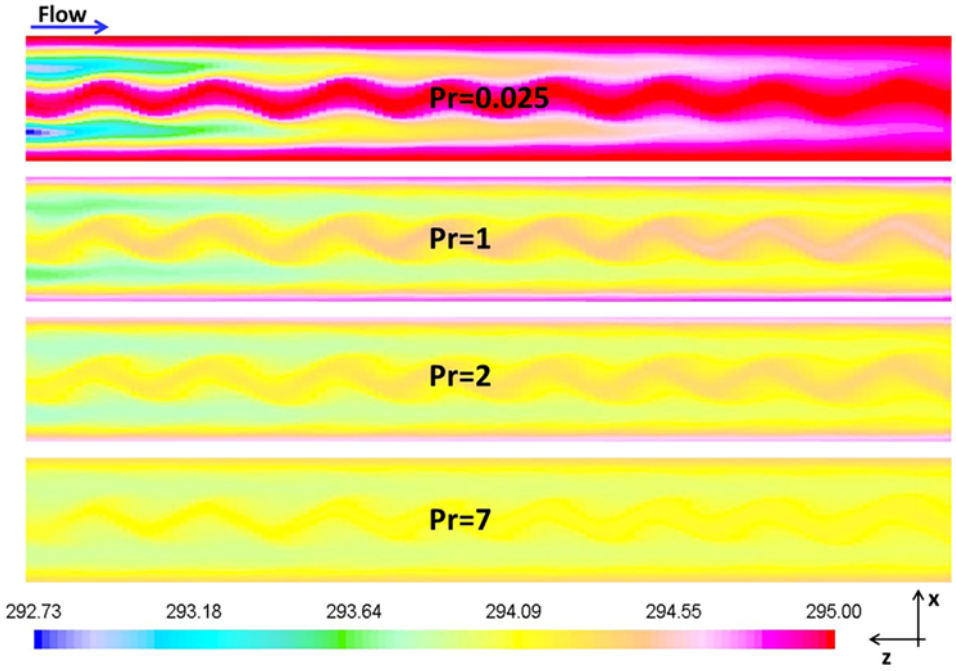

Figure 25: Streamwise iso-contours of static temperature.

In addition, temperature profiles are also extracted corresponding to Line 1 and 3 and are given in Fig. 27. By looking at the results, it can be

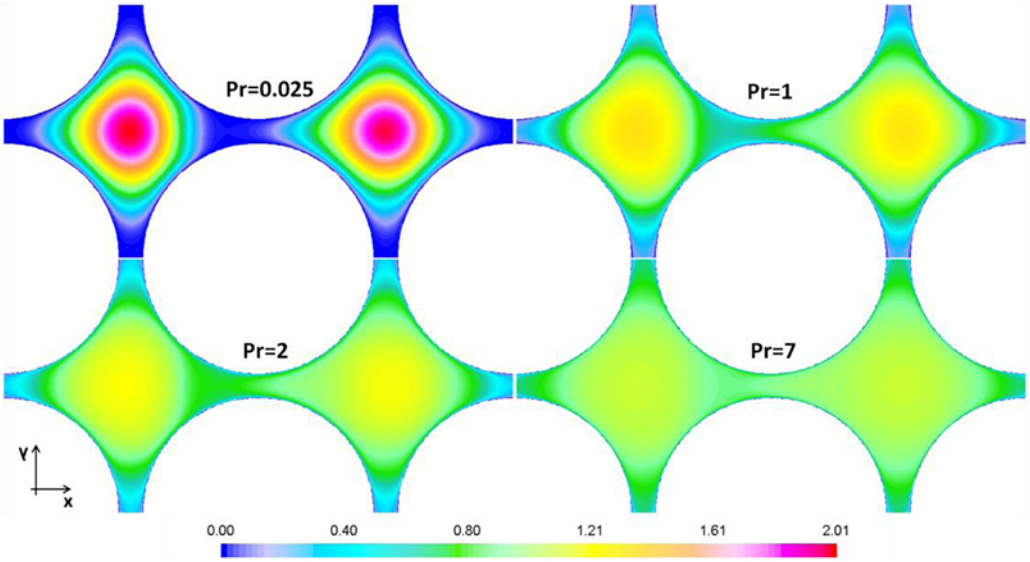

Figure 26: Iso-contours of scaled temperature for Dirichlet boundary condition on temperature at cross-section in the middle of the domain.

noticed that different temperature fields are obtained for different Prandtl fluids in comparison to the velocity field in Fig. 14: the thermal boundary layer is thicker for liquid sodium, the same for air, and thinner for water at T = 292.8 K and T = 355 K than momentum boundary layer. This suggests that in order to resolve all these small thermal scales, a much finer mesh would be required, which will eventually increase the overall computational cost of targeted DNS.

4.3.5 Constant heat flux on rods

In the case of constant heat flux boundary condition (Neumann condition), the heat flux of 0.12 W/m^2 has been imposed on rods. The obtained results are presented in Fig. 28 and 29. In comparison with the constant temperature boundary conditions, it is clearly noticeable that the predicted thermal boundary layers for the $Pr \geq 1$ are not so prominent. Although a similar trend is also visible for liquid sodium with $Pr = 0.025$, nonetheless the thermal boundary layer is still thicker than the momentum boundary layer, so the gradients are not so sharp. In summary, both thermal boundary conditions imply that a much finer mesh is required to

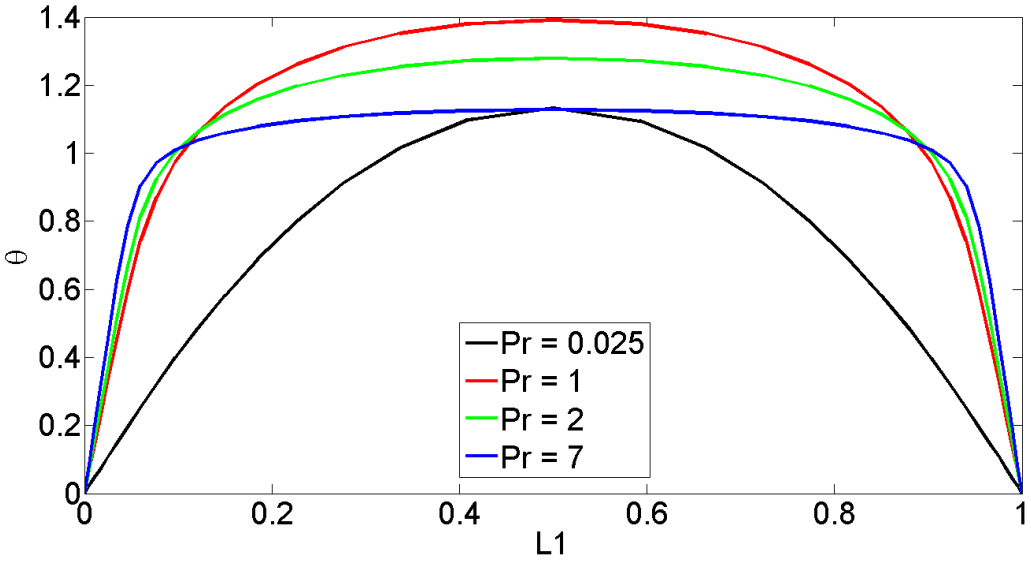

(a) along L1

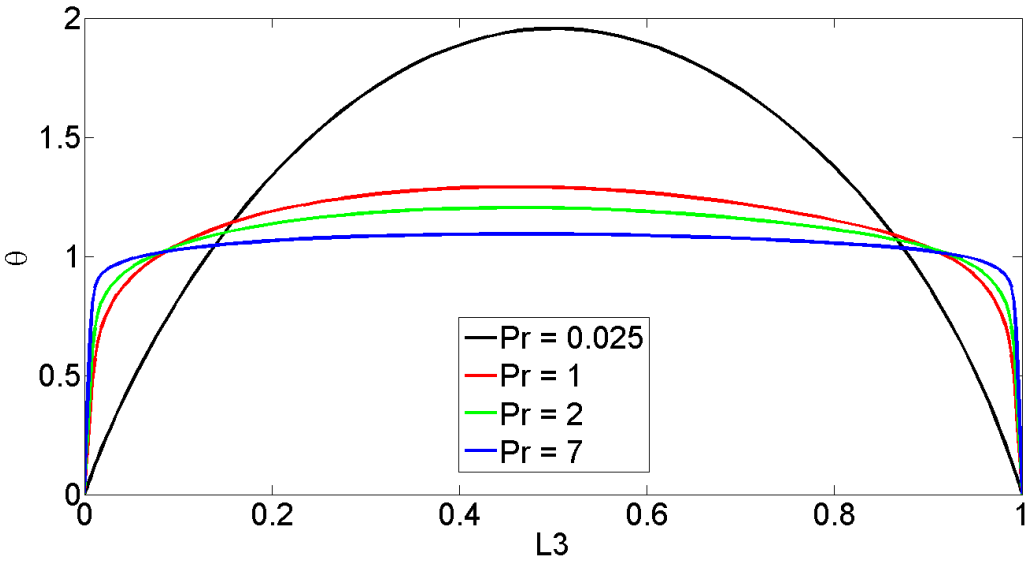

(b) along L3

Figure 27: Thermal boundary layer for constant temperature boundary condition.

resolve the smaller thermal scales present for $Pr \geq 1$ fluids. Other than that, **both boundary conditions display different thermal fields for the respective Prandtl numbers, hence, the resulting DNS seems to provide promising and extensive database for the validation purpose.**

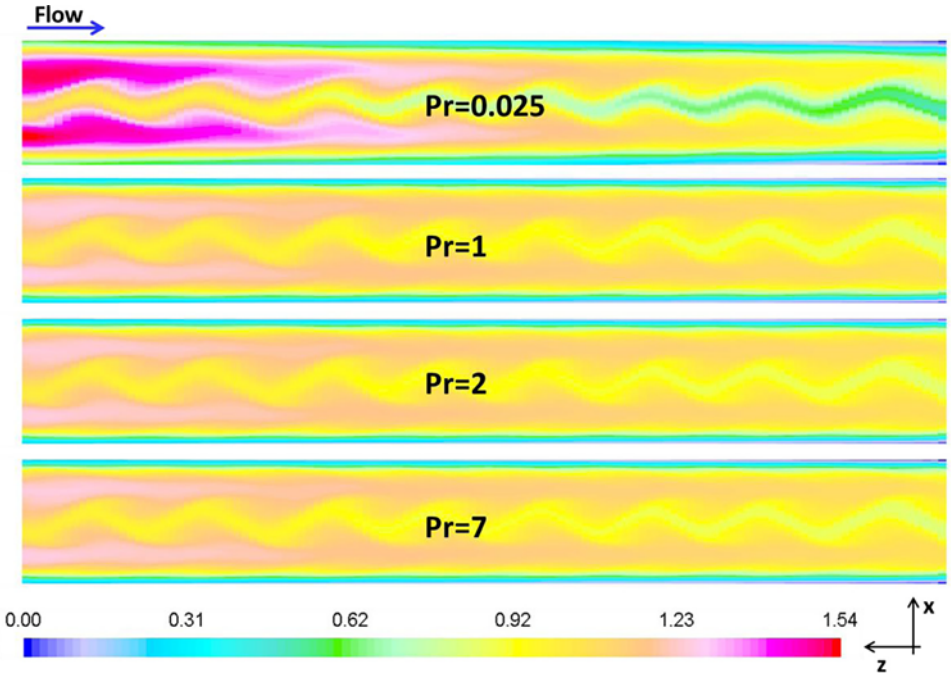

Figure 28: Streamwise iso-contours of scaled temperature for Neumann boundary condition.

4.4 Finalized rod bundle configuration for targeted DNS

Based on the wide range of URANS computations (precursor analysis) performed in the previous section, the Hooper case which is based on a tightly spaced bare rod bundle case, has been calibrated and optimized in order to perform a DNS computation involving flow and heat transfer analyses. The important parameters of this finalized design are summarized in Table 6.

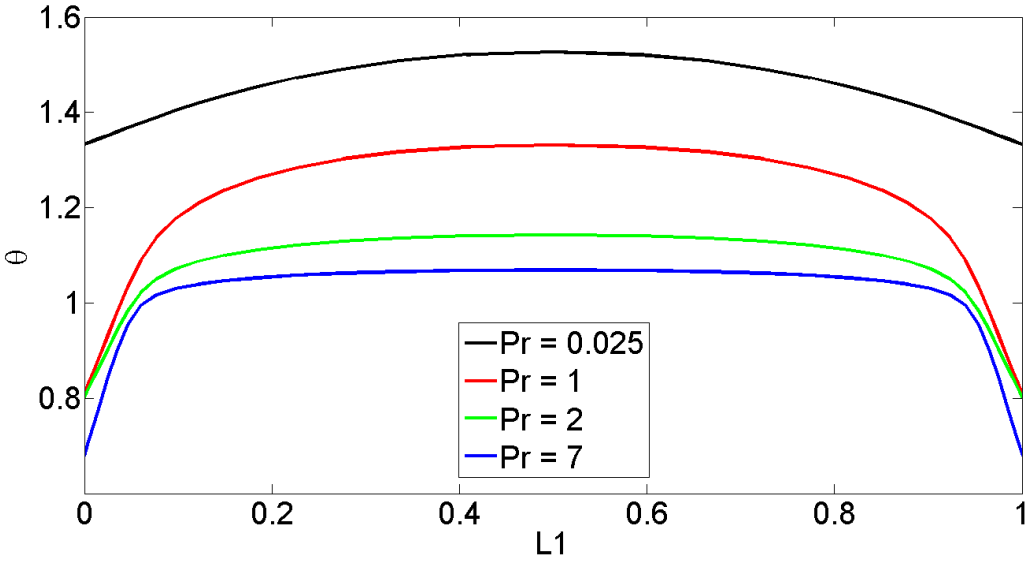

(a) along L1

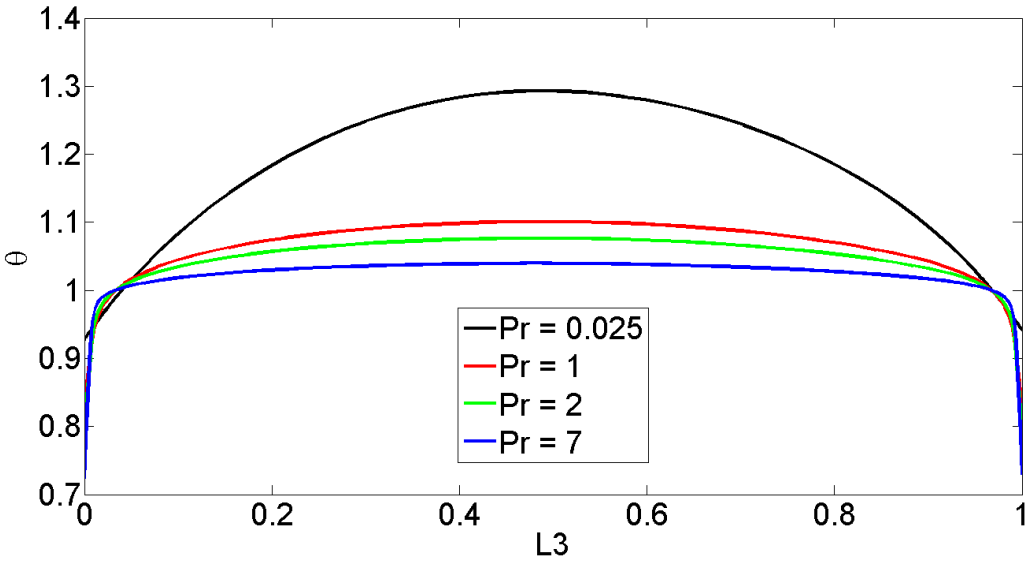

(b) along L3

Figure 29: Thermal boundary layer for constant heat flux boundary condition.

Table 6: Finalized parameters of the tightly-spaced bare rod bundle (based on the Hooper case) for the DNS study.

Parameter	Value	Units
Rod diameter (D)	14	cm
Pitch (P)	15.5	cm
P/D	1.107	-
Re	9800	-
Mass flow rate	0.043	kg/s
Axial length	2.285	m
Selected Pr numbers	7, 2, 1, 0.025	-
Temperature on the rods	15.5	K
Heat flux on the rods	0.12	W/m^2

4.5 Mesh estimation for the DNS

In order to assess the feasibility of the optimized rod bundle for the targeted DNS computation, in this section, an attempt is made to estimate the overall mesh requirement. Previously obtained URANS solution has been utilized to provide an insight into different length scales present throughout the computational domain. Particularly, the estimation of Batchelor and Kolmogorov length scales are the most crucial ones from the determination of the overall mesh requirement point of view. However, in order to gain the trust in these estimated length scales, it is essential to make sure that the obtained URANS or the RANS solutions are grid independent. Hence, a pre-requisite mesh sensitivity study of the finalized rod bundle case is performed and discussed in the following section.

4.5.1 Mesh sensitivity study of RANS precursor analysis

In order to perform a mesh sensitivity study for the considered flow configuration, it is important to perform the RANS computations rather than the URANS, which has been the case in the previous sections. In this regard, additional RANS computations are performed for three different meshes. The details of these meshes are listed in Table 7.

Table 7: Considered three different meshes for the mesh sensitivity study.

Mesh	No. of grid points (million)
M1	0.9
M2	1.7
M3	4.1

It is worthwhile to mention that in the previous sections, all the URANS computations corresponding to Re = 9800 have been performed on mesh M2. Fig. 30 and 31 show the comparison of the velocity magnitude along Lines 1 and 3, for these three meshes. The presented velocities were divided by the local bulk velocities u_b. It can be noticed that all the profiles overlap each other, which suggests that even M1 is good enough to capture the overall flow topology appearing for the Re = 9800.

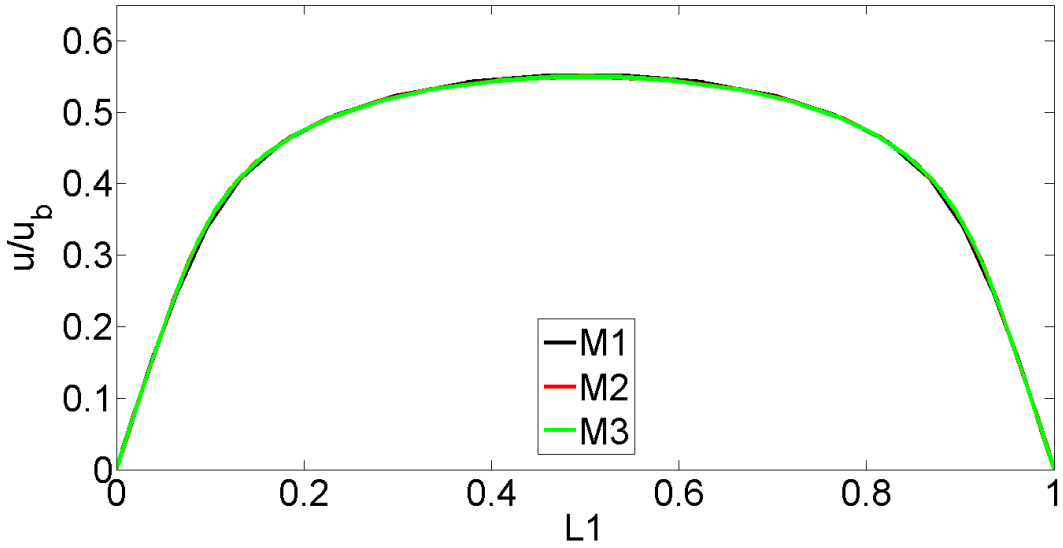

Figure 30: Comparison of the velocity magnitude for three different meshes along L1.

Such type of comparison is also performed for more parameters such as, turbulent kinetic energy and temperature. Looking at the results for turbulent kinetic energy presented in Fig. 32 and 32, and for the temperature presented in Fig. 34 and 35 the similar trend as for velocities is observed for all the meshes. However, along L1 (namely in the narrowest gap region) slight discrepancies are noticeable, nevertheless the profiles

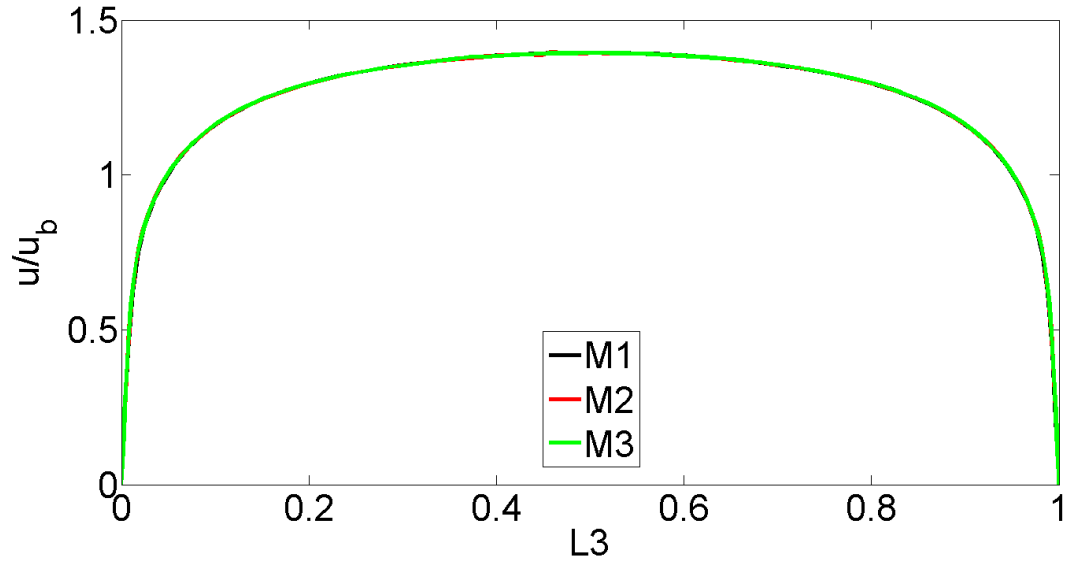

Figure 31: Comparison of the velocity magnitude for three different meshes along L3.

follow a consistent trend. While for the sub-channel region, where L3 was extracted, it is observed, that turbulent kinetic energy k close to the rod walls is moderately overestimated for M1.

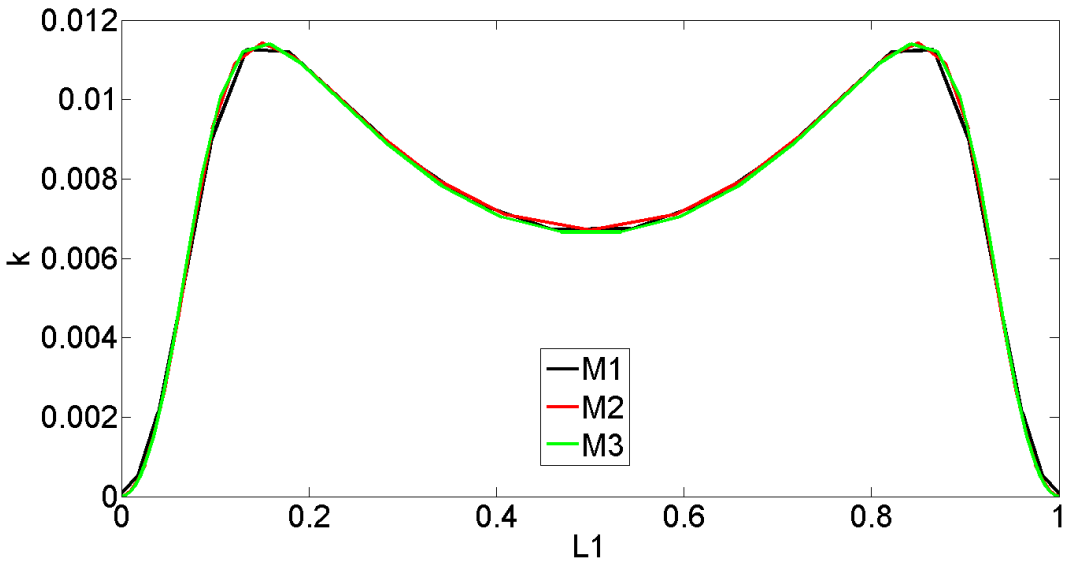

Figure 32: Comparison of the turbulent kinetic energy for three different meshes along L1.

It was found that even M1 is good enough to capture the overall flow topology and displays a difference of less than $\sim 1-3\%$ with respect to

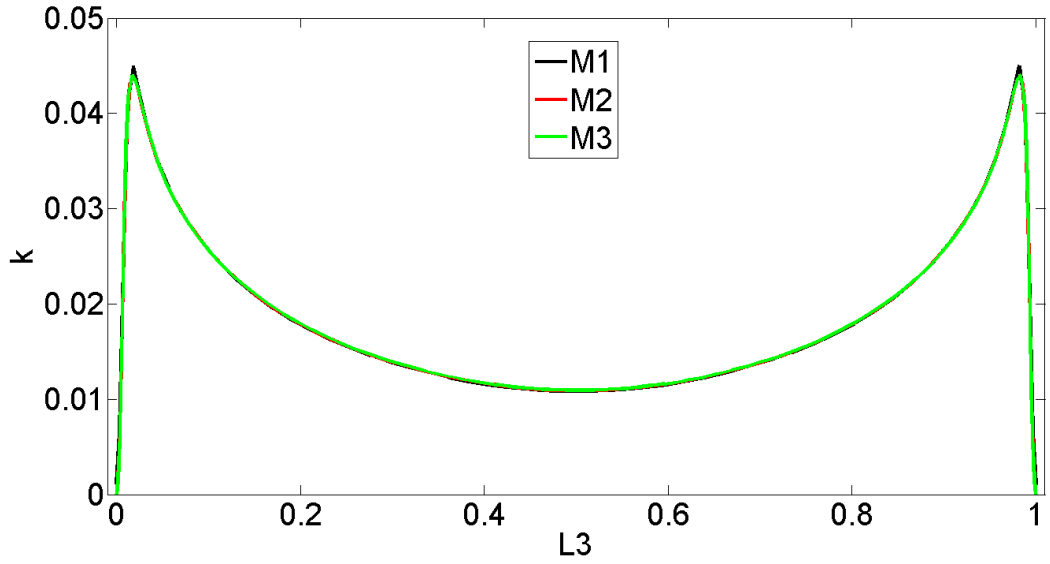

Figure 33: Comparison of the turbulent kinetic energy for three different meshes along L3.

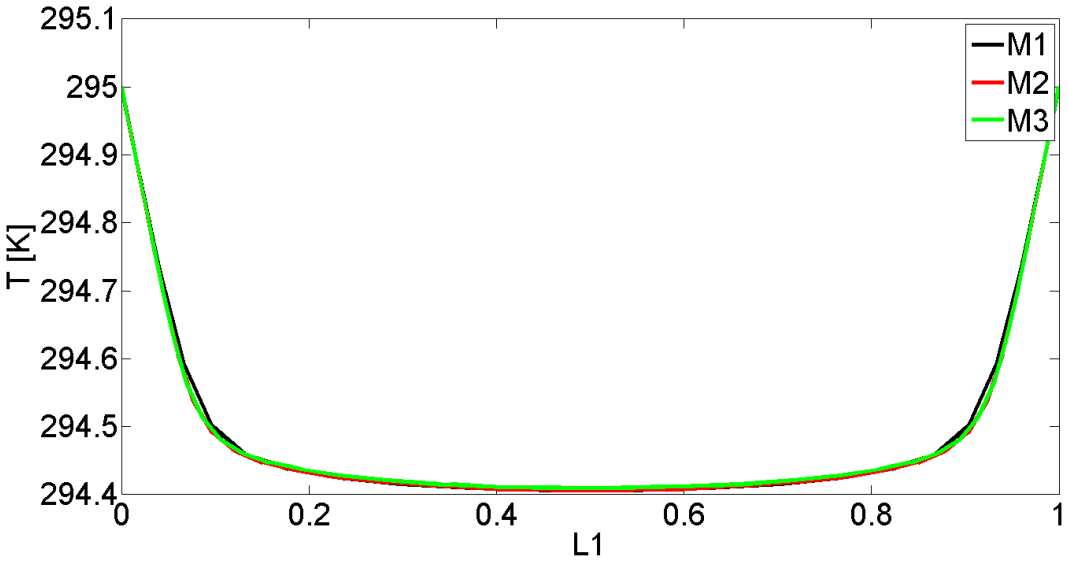

Figure 34: Comparison of the temperature for three different meshes along L1.

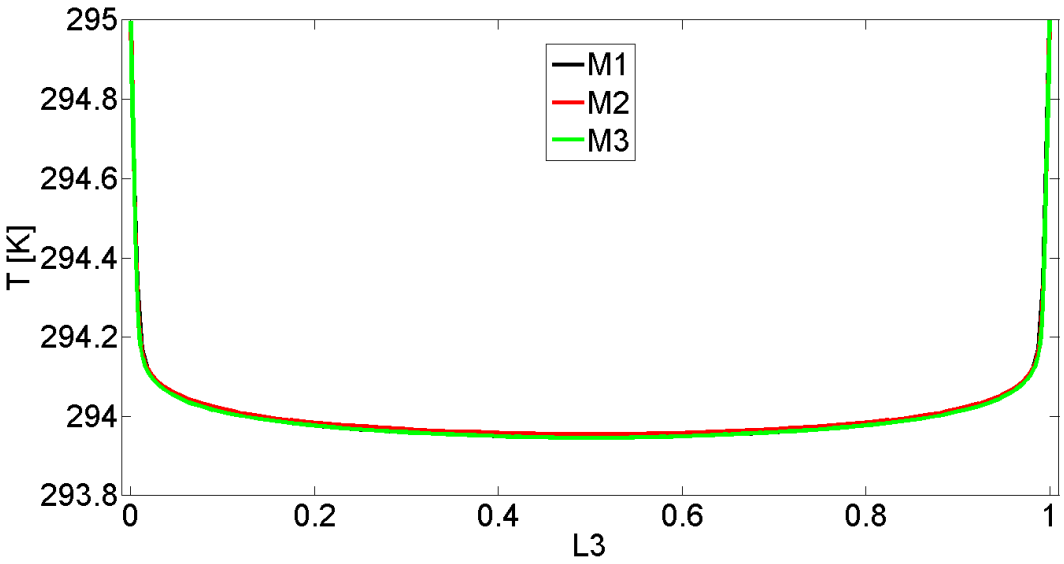

Figure 35: Comparison of the temperature for three different meshes along L3.

the other meshes. In summary, even though all the considered meshes are sufficiently fine to reproduce the overall flow topology, however, the finest mesh (i.e. M3) has been selected to extract the Kolmogorov and Batchelor length scales and are discussed in the next section.

4.5.2 Mesh estimation for DNS

Two important length scales, i.e. Kolmogorov and Batchelor, are computed to find out the mesh requirements for the targeted computation. In order to do this, the available classical formulas are used. Kolmogorov length scale (KLS) was already introduce, see equation 3.4. Batchelor length scale (BLS) is defined as:

$$\lambda_B = (\frac{\alpha^2 \nu}{\varepsilon})^{1/4}, \tag{4.6}$$

where ν is the kinematic viscosity, ε is the turbulence dissipation rate, and α is the thermal diffusivity. The obtained length scales are non-dimensionalized by using the mean friction velocity u_τ over the surface of the rod.

Figs. 36 and 37 display the iso-contours of non-dimensional Kolmogorov

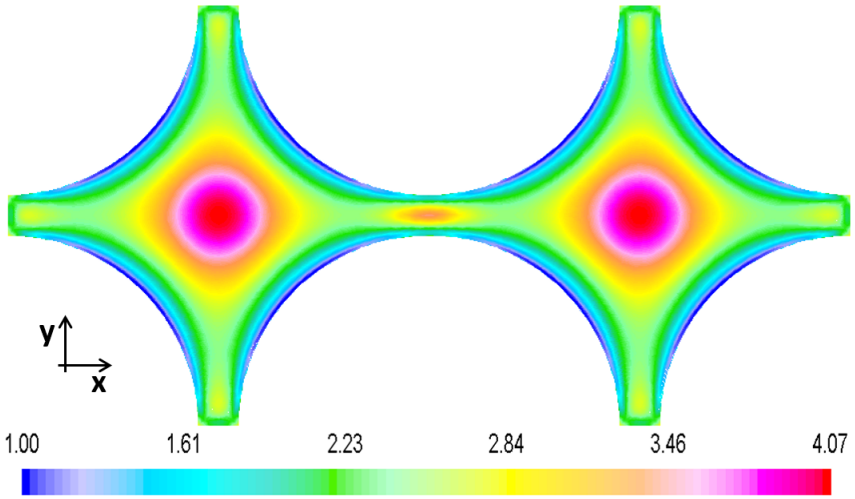

Figure 36: Cross-section iso-contours of KLS.

length scales for two different planes - cross-section and streamwise. The obtained results suggest a wide range of scales ranging from a minimum of 1 to the maximum of 4.07 in the center of the sub-channel region. Moreover, the profiles of these length scales are extracted corresponding to L1 and L3 line, explicitly shown in Fig. 38.

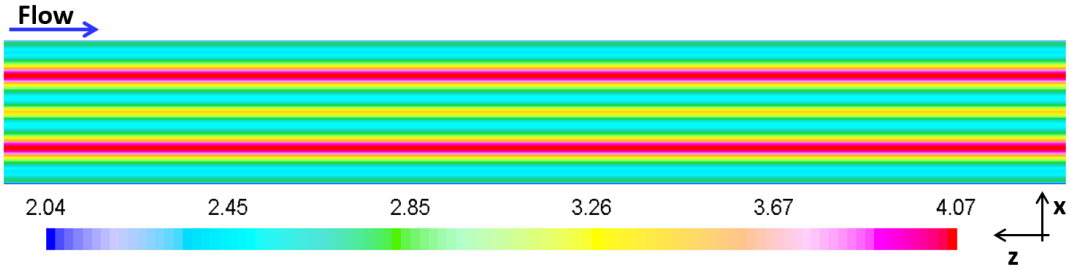

Figure 37: Streamwise iso-contours of KLS.

The non-dimensional KLS profiles corresponding to Lines 1 and 3, clearly shows that the KLS are relatively small in the gap region, (where the gap vortex street appears) than in the sub-channel region. Hence, it is important to resolve these smaller scales which appear in the the gap region, as it contributes to wall shear stress distribution which dictates the whole flow field.

Moreover, since the thermal field has been introduced with the use of

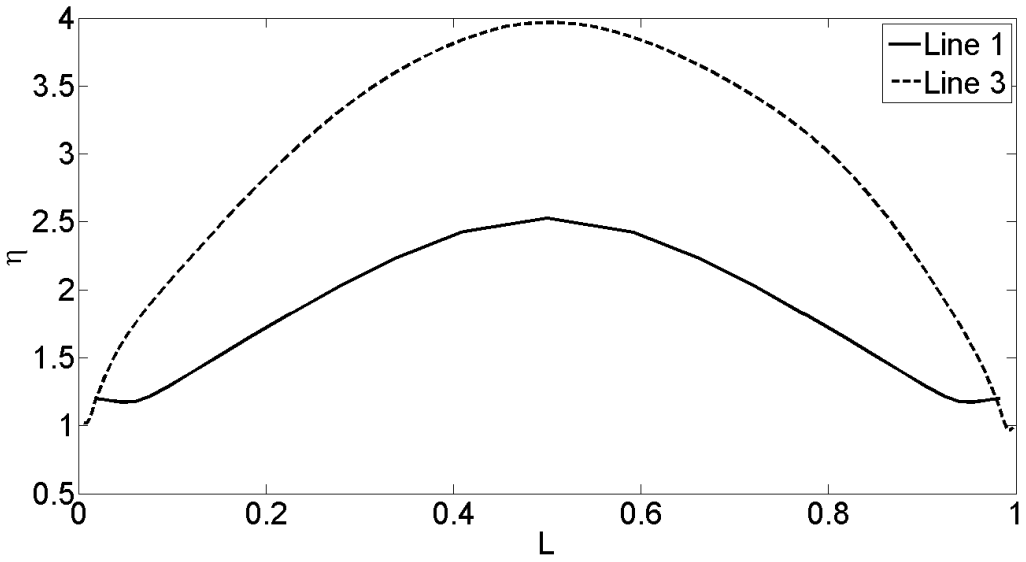

Figure 38: Non-dimensional Kolmogorov length scale in the gap and sub-channel region.

passive scalars, accordingly the momentum field corresponding to all the Prandtl fluids remains the same and subsequently same distribution of the KLS. However, the considered Prandtl fluids have different thermal diffusivity, thus the BLS are also computed for all four Prandtl fluids. The profiles of the computed BLS for L1 and L3 are presented in Figs. 39-42.

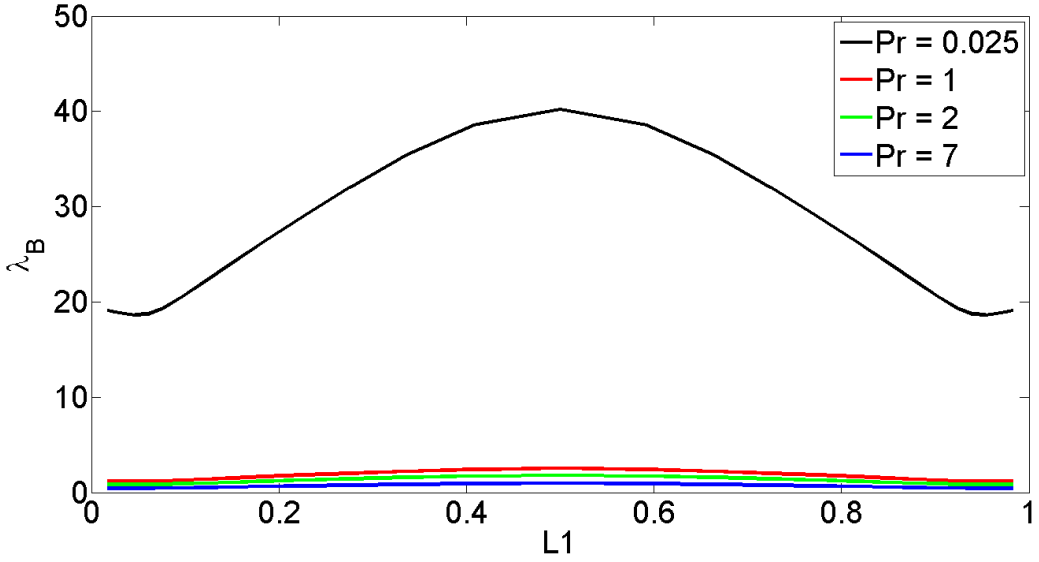

Figure 39: Non-dimensional Batchelor length scale in the narrowest gap region.

It is worth reminding that in Section 4.3.3, it was found out that the

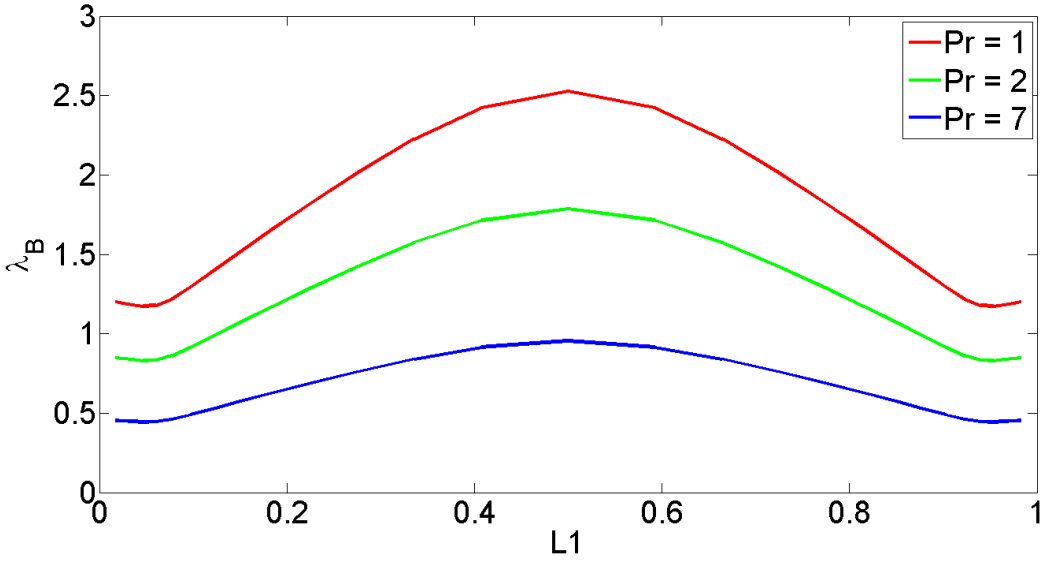

Figure 40: Non-dimensional Batchelor length scale in the narrowest gap region for fluids of Pr number = 1, 2, and 7.

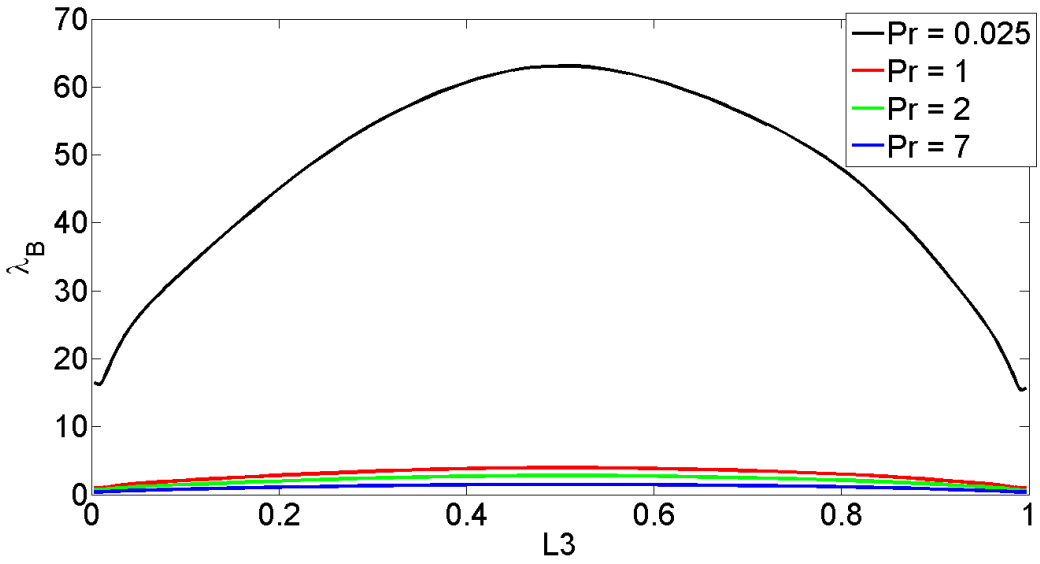

Figure 41: Non-dimensional Batchelor length scale along L3.

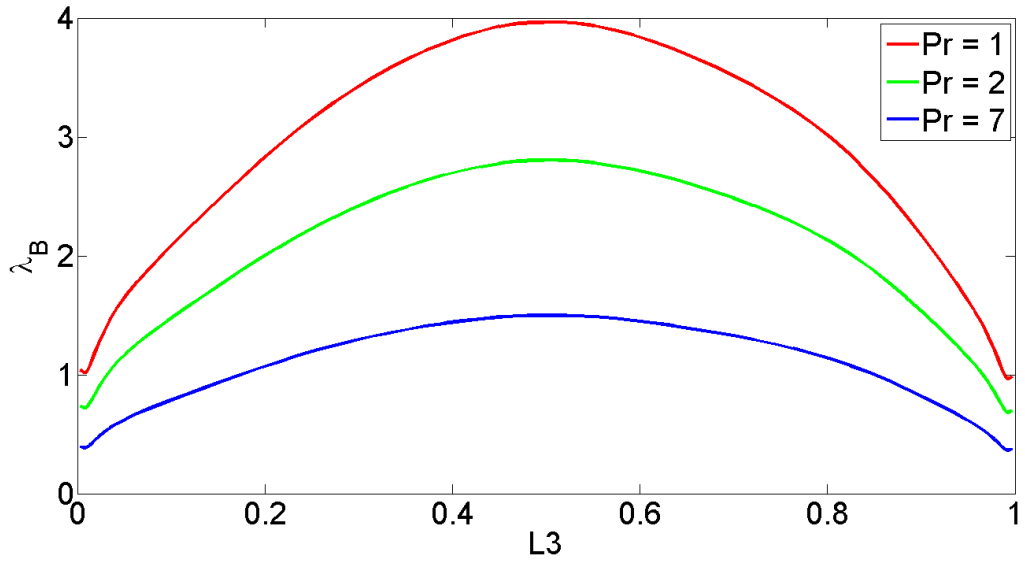

Figure 42: Non-dimensional Batchelor length scale along L3 for fluids of Pr number = 1, 2, and 7.

thermal boundary layer for the imposed constant heat flux boundary case is relatively thinner than what was observed for the constant temperature boundary condition. Accordingly, the BLS are computed corresponding to the heat flux boundary condition case. Nonetheless, by looking at the results, it is clearly visible that the case with Pr = 0.025 displays the largest BLS, which is expected because of its high thermal diffusivity and consequently larger scales of the thermal field. Whereas, for Pr = 1 both the KLS and BLS are similar. However, for the Pr > 1 the observed BLS are found to be much smaller than the KLS. Nonetheless for all cases, these scales are not uniformly distributed (as the observed flow field shows a very complex three dimensional distribution). Therefore, an ingenious meshing technique will be needed in order to create a computationally affordable mesh for a DNS computations. Accordingly, an estimation of the mesh is performed and it gives a total of $\sim$ 1 billion grid points in order to perform the targeted DNS including all four passive scalars. This number is mainly increased because of the Pr = 7, which exhibits smaller Batchelor length scales. If the case of Pr = 2 is considered then the overall mesh is

reduced to $\sim$ 600 million grid points. Taking into account the available computer resources, it was decided that the final DNS will include three passive scalars, namely up to the Prandtl fluid Pr = 2.

5 DNS of the Hooper case

5.1 Brief introduction to DNS setup

Performed DNS is based on the calibration and optimization settings described in Section 4. As mentioned in the previous section, the Reynolds number based on the bulk velocity and the hydraulic diameter is Re = 9800, which corresponds to a friction Reynolds number $Re_\tau = 605$. At the inlet/outlet of the computational domain, a periodic boundary condition has been imposed by means of mass flow rate. The rods are considered as no-slip walls.

The thermal boundary conditions used in this work are both iso-thermal and iso-flux conditions which correspond to the two extreme scenarios of a Conjugate Heat Transfer (CHT) [11]. The fluid properties are assumed to be constant. Hence, the temperature is treated as a passive scalar. Thanks to this assumption in one single DNS computation, multiple passive scalars have been included. It is to be noted here, that the temperature and other transport scalars used here are passive scalars. This means that they do not affect the velocity or the pressure fields, thus their governing equations can therefore be solved separately and are not coupled to the momentum equation. Such an approach reduces the computational effort, and also allows multiple passive scalars to be simulated.

These passive scalars correspond to the Prandtl numbers of three different working fluids, i.e. water, air, and liquid metal, i.e. Pr = 2, 1, and 0.025, respectively. The heat transfer of these three fluids has been studied in combination with two different boundary conditions at the walls, i.e. a constant temperature and a constant heat flux. Therefore, in total, the DNS computation consists of six thermal fields.

5.2 Numerical method

5.2.1 Governing equation and boundary conditions

Let us introduce the following dimensionless variables:

$\mathbf{u}^* = \frac{u}{U}$, $t^* = \frac{tU}{L}$, $T = \frac{T^* - T_0}{\delta T}$.

For the pressure scale we have two regimes:

- Convective effects are dominant i.e. high velocity flows $p^* = \frac{p}{\rho U^2}$
- Viscous effects are dominant i.e. creeping flows (Stokes flow) $p^* = \frac{pL}{\mu U}$

Under the assumption of constant fluid properties, the non-dimensional incompressible Navier-Stokes, and temperature equations read:

$$\nabla \cdot \mathbf{u}^* = 0, \tag{5.1}$$

$$\frac{\partial \mathbf{u}^*}{\partial t} + (\mathbf{u}^* \cdot \nabla)\mathbf{u}^* = -\nabla p^* + \frac{1}{Re}\nabla^2 \mathbf{u}^*, \tag{5.2}$$

$$\frac{\partial T^*}{\partial t} + (\mathbf{u}^* \cdot \nabla)\mathbf{T}^* = -\nabla p^* + \frac{1}{PrRe}\nabla^2 \mathbf{T}^*, \tag{5.3}$$

where $\mathbf{u}^* = (u^*, v^*, w^*)^T$ is the velocity, p^* is the pressure, and T^* is the temperature.

The no-slip boundary conditions on the walls are imposed by enforcing the zero velocity condition. The iso-thermal and adiabatic boundary conditions are enforced by imposing the wall temperature as a Dirichlet boundary condition and the zero heat flux as a Neumann boundary condition, respectively, as shown in Fig. 43 by arrows.

5.2.2 Discretization and solution method

The DNS has been carried out using the massive parallel code NEK5000 [91] which uses spectral element method (SEM) [92] to discretized the governing equations. In this approach, the domain is first discretized into

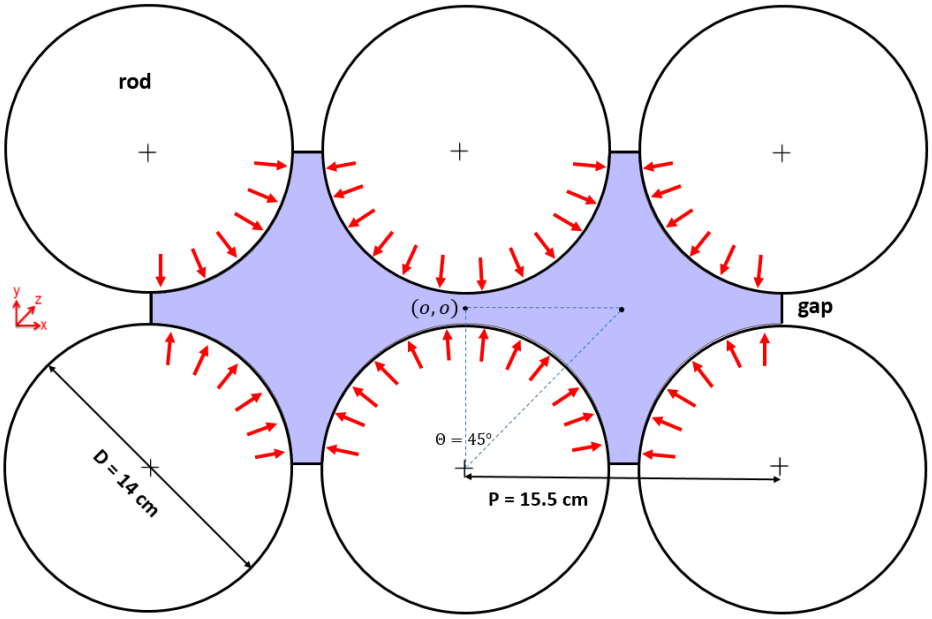

Figure 43: Schematic of geometric dimensions and thermal boundary conditions.

several hexahedral macro-elements. Subsequently, the variables of the governing equations are approximated using polynomial expansions of degree N used in each macro-element in order to approximate the solution. The Gauss-Lobatto-Legendre (GLL) polynomial expansion is used along each spatial direction and the same polynomial degree is adopted for the velocity and the pressure (PN/PN-2 formulation) and as standard practice, the over-integration and filtering stabilization schemes are used [92]. The semi-discretized equations are then integrated in time with a third-order scheme based on the use of an implicit backward difference formula (BDF) and an explicit extrapolation scheme for the viscous and the convective terms, respectively.

The NEK5000 code is well suited for High Performance Computing (HPC) applications due to its good parallel scalability even with a very large number of processors. Furthermore, the SEM formulation makes the NEK5000 code extremely accurate for DNS applications. To this purpose, the accuracy of NEK5000 has been studied in [93] where NEK5000 was used to perform DNS of planar channel flows and the effects of different

numerical parameters on the accuracy of the solutions were investigated. Furthermore, the accuracy of NEK5000 on skewed grids was studied. It was concluded that NEK5000 is able to produce high-quality DNS solutions even on distorted grids, therefore it could be used for applications that involve complex geometries. Additionally, dedicated performance tests [2] with usage of NEK5000 were done at the Świerk Computing Centre (CIŚ), located at National Centre for Nuclear Research, Poland. The tests assess the influence of the CPU architecture, cooling infrastructure, and interconnection performance on the solver running times. In general, the hardware configuration, software used for on-demand deployment of dedicated subclusters, and queuing systems were thoroughly tested. This was a very important step, before the final DNS computations started. In order to perform the targeted DNS, $\sim$ 10 000 processors were utilized. It was the biggest single case job run at CIŚ infrastructure so far. The DNS calculations started in the spring of 2018 and continued until spring 2022 (not counting the time of maintenance breaks and necessary repairs). A total computational time of $\sim$ 375 million core hours is used to perform DNS!

5.2.3 Meshing strategy and turbulence scales

In Fig. 44 mesh generated for DNS is shown. This 2D mesh is uniformly extruded in the streamwise (z-direction). A block-structured grid of macro-elements has been generated using a non-uniform wall-normal spacing in the computational domain. The spatial resolution required by the DNS simulation was estimated using Kolmogorov and Batchelor length scale as it was already presented in Section 4.5.2. The spatial resolution in the domain ranging from a minimum of 1 (close to the wall) to the maximum of 4 in the center of the sub-channel region. The obtained length scales are non-dimensionalized by using the mean friction velocity over the surface of the rod. There are: 8150 macro-elements in cross-section, 150 macro-elements in z-direction, thus in total there are 1222550 macro-elements.

Wall macro-element size is 0.3 mm and in the narrow gap region there are 42 macro-elements. Spectral element size scale with $1/N$, and total number of spectral mesh elements scale with $(N+1)^3$, where N is the polynomial order of the SEM calculation. In the other words, for an N-th polynomial order, each macro-element is split into $(N+1)^3$ GLL points. In order to take into account the contribution of the polynomial refinement, the average spatial resolution is computed by assuming a uniform point distribution within each macro-element. That is, for the present case with a polynomial degree N = 7, the average spatial resolution (Δ) is obtained by dividing each macro element with eight points distributed along each spatial direction as shown in Fig. 45. In total there are approximately 630 million elements of the computational mesh.

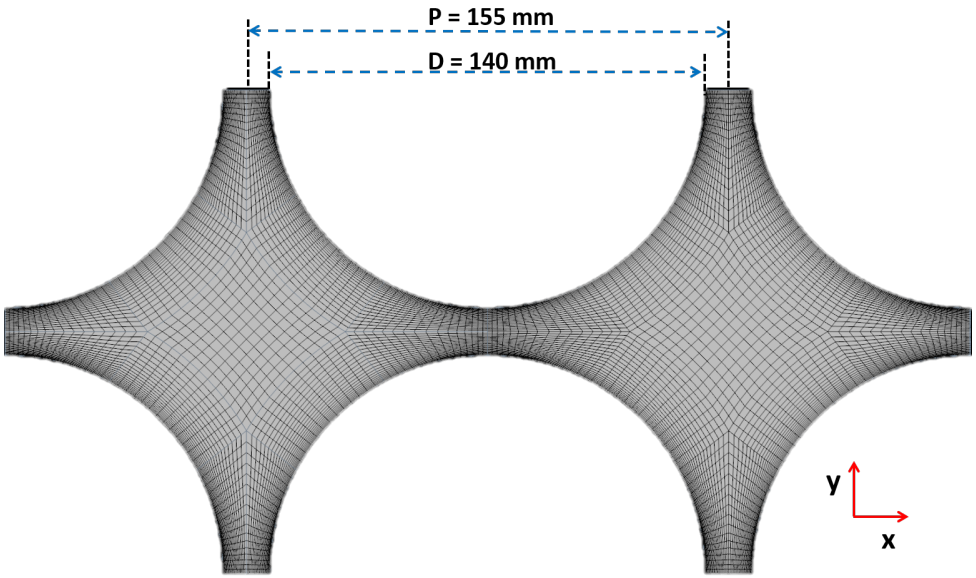

Figure 44: Mesh for DNS on the xy-plane.

Whence, the generated mesh was based on the precursor RANS simulations, as a next step, the spatial resolution was verified posterior against the Kolmogorov and Batchelor length scale computed from the DNS.

Fig. 46 depicted the comparison of Kolmogorov length scales predicted by RANS vs UDNS (UDNS stand for under-resolved DNS, which means DNS with N=3). It is easily noticed, that UDNS calculation provides an

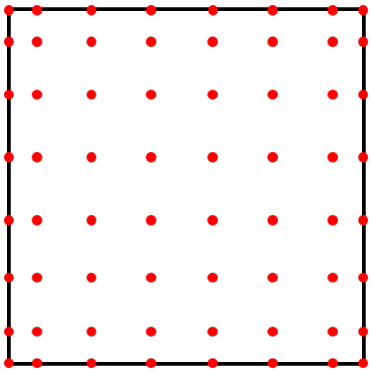

Figure 45: Distribution of Gauss-Lobatto-Legendre points within one element.

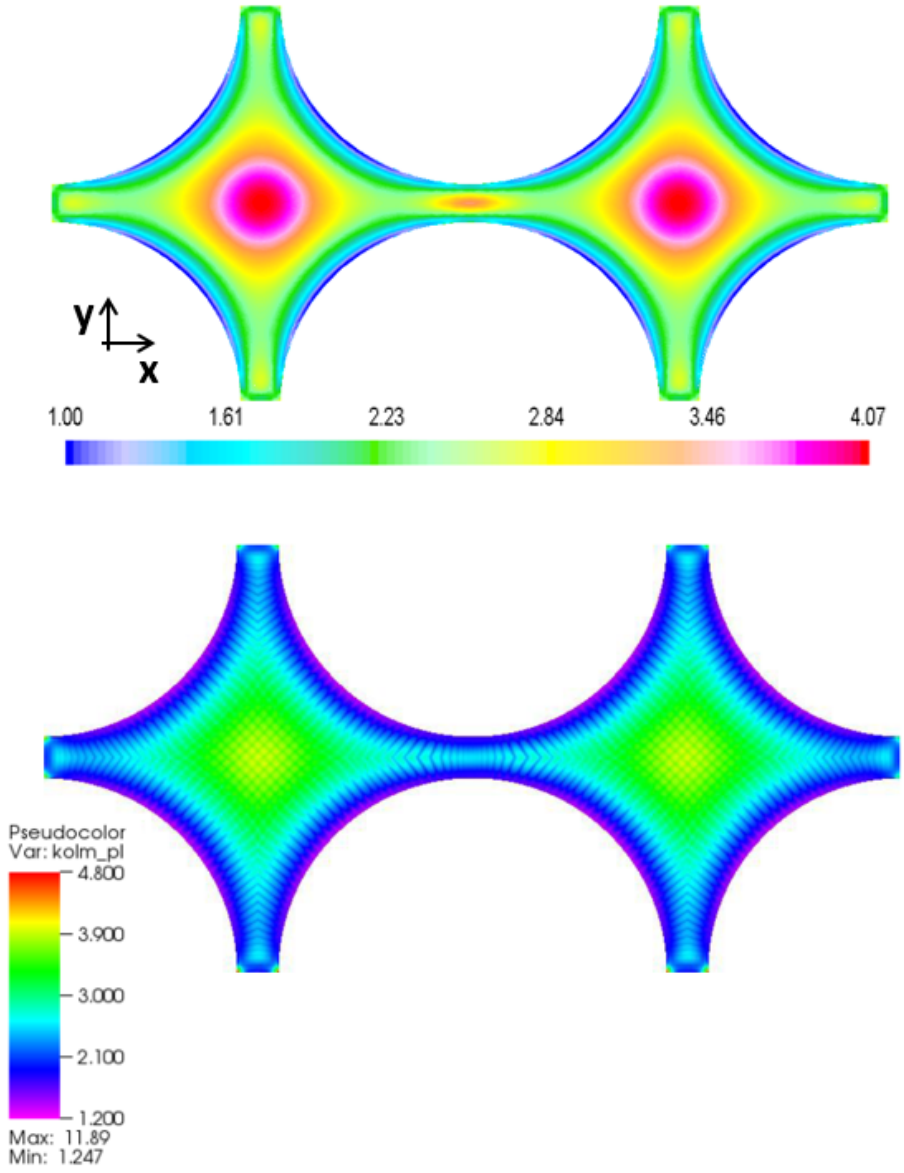

Figure 46: Comparison of Kolmogorov length scales predicted by RANS vs UDNS.

estimate of Kolmogorov scales similar to those predicted by RANS. Results are presented in non-dimensional units, namely:

$$\eta_k^+ = (\frac{\eta_k u_\tau}{\nu}). \tag{5.4}$$

Kolmogorov length scales:

- estimated from the Hooper UDNS simulation $\eta_k^+ = 1.2$
- predicted by the precursor RANS simulations [1] $\eta_k^+ = 1.0$

Cells size ($\Delta = \mathrm{Vol}^{1/3}$) calculated from fully-resolved DNS (DNS with N=7) is presented in Fig. 47.

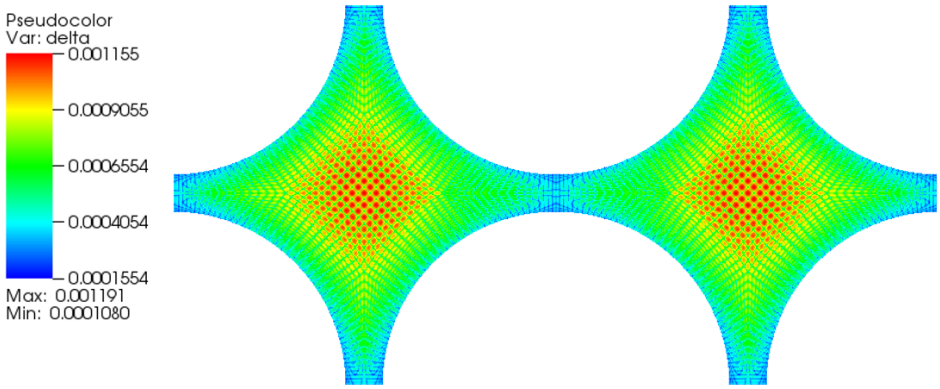

Figure 47: Cell size calculated from fully-resolved DNS.

Knowing the Kolmogorov length scale KLS (η_k) calculated from UDNS case and cell size calculated from fully-resolved DNS, the spatial resolution criterion was checked. According to Pope [61], fully-resolved DNS should satisfy the following criterion:

$$\Delta/\eta_k \sim \pi. \tag{5.5}$$

In Fig. 48 spatial resolution for fluid calculation, Δ/η_k, and spatial resolution for thermal calculation, Δ/η_B, for Pr = 2.0, is presented. It

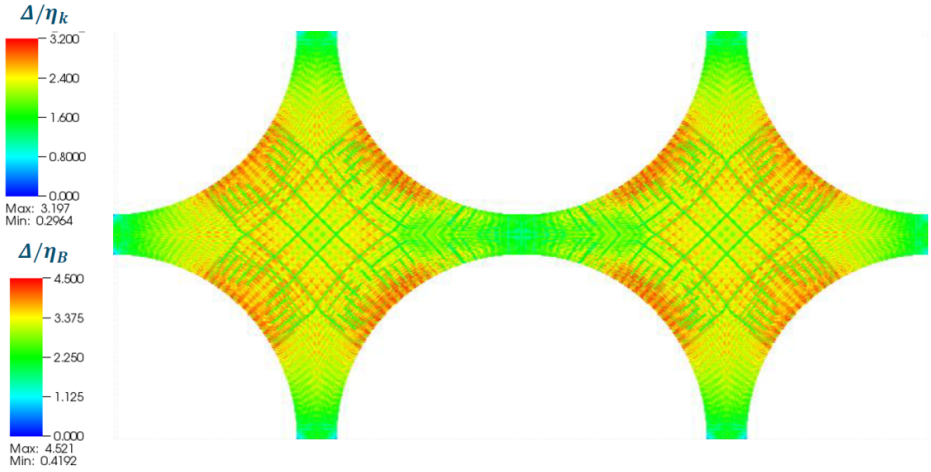

Figure 48: Spatial resolution for fully-resolved DNS.

can be concluded that the fully-resolved Hooper DNS is using a spatial resolution which follows the Pope criterion (5.5).

Additionally, in order to check the time resolution, the Kolmogorov time scale (KTS) and Batchelor time scale (BTS) were checked. In Fig. 49 non-dimensional Kolmogorov and Batchelor time-scales are presented.
Maximum value of non-dimensional KTS: $\tau_k^* = \frac{\tau_k U_b}{D_h} = 0.042$.
Maximum value of non-dimensional BTS: $\tau_B^* = \frac{\tau_B U_b}{D_h} = 0.021$.

For the current DNS calculations the criterion of Courant number $\mathrm{C} \leqslant 0.4$ was assumed. DNS simulation was initially performed with $\mathrm{C} = 0.1$ (as presented in Fig. 50). However the simulation proceeded very slowly, even when using 10 000 cores. Therefore, when the desired time-converged flow and temperature statistics have been achieved, the Courant number was increased to $\mathrm{C} = 0.4$. With this modification, simulation speeded up to achieve the time-convergence much earlier, while retaining the solution accuracy. For $\mathrm{C} = 0.1$, the time-step size $\Delta t^* \sim 6 \times 10^{-6}$, while for $\mathrm{C} = 0.4$, the time-step size $\Delta t^* \sim 1.3 \times 10^{-4}$. Thus, the criterion of $\mathrm{C} \leqslant 0.4$ restricts the time-step to a value two-four order of magnitude smaller than the Kolmogorov and Batchelor time-scales, in order to minimize numerical

errors of the integration and maintain high spatial and temporal accuracy.

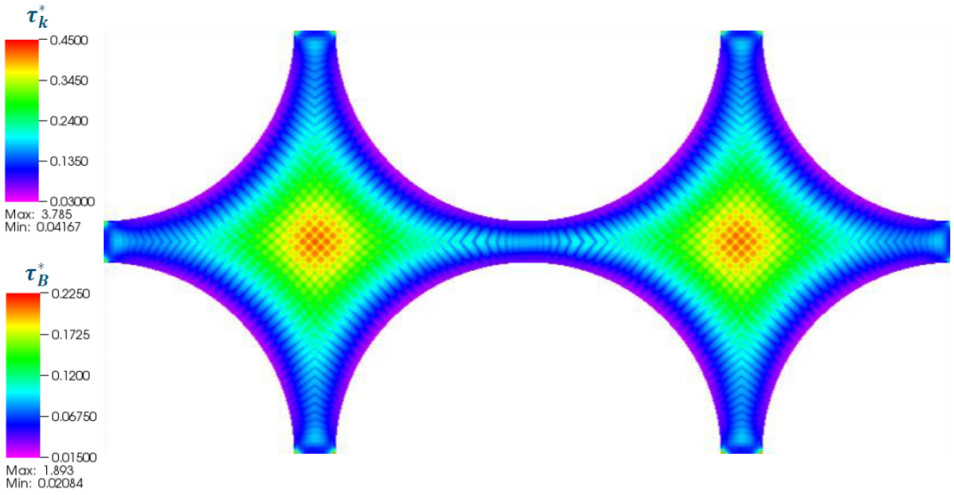

Figure 49: Kolmogorov and Batchelor time scales in DNS.

As a conclusion, it was proved that the mesh size is sufficient by calculating the relative mesh size and comparing it with the smallest Kolmogorov micro-scale at every time step. Overall, the mesh is judged to be sufficient for DNS at every location. The implemented resolution is recognized as sufficient for predictions of 3^{rd} and 4^{th} order statistics with DNS accuracy [94]. In this thesis the 1^{st} and 2^{nd} order statistic were only considered.

5.3 Approach toward the statistical steady state

The instantaneous fields of velocity and temperature are useless for any comparisons with other methods, different implementations of the same method, or even different runs of the same code with the same inputs. The results of the simulation therefore need to be averaged in time and the averages and higher moments of particular fields are then compared. In order to meaningfully present the averages and higher moments of the fields, the statistical properties of the flow have to be in a state, where they do not significantly vary with time. When this condition is reached, the simulation has reached a statistical steady state [61] or co-called quasi steady state. Similarly, a field is statistically homogeneous if all statistics

are invariant under a shift in position.

5.3.1 Temporal integration

The temporal integration is divided into two parts. The first part of the simulation was used to reach the statistical steady state. Once it was recognized that the simulation has reached the quasi steady state, time integration was performed with averaging the various fields through time. However, running DNS is not a straightforward procedure. Targeting to the high fidelity results, starting the simulation with high order polynomial (N) was not the best option. Thus, in the current study the following approach was adopted, in order to avoid the numerical divergence and let the flow properly developed:

1. As a starting point DNS with N=3 was computed. The implementation of passive scalars was tested, thus this phase is UDNS or testing phase. Simulation was run as long as the flow and thermal fields reached the quasi steady state.

2. In a second step, results from N=3 was interpolated to N=5 calculation.

3. Finally, the DNS with N=7 was run.

After a statistical steady state was reached, time averaging of results was performed. To determine when the simulation reached statistical steady state, a few parameters were calculated. These parameters are described below.

Steady state for the friction velocity u_τ

Fig. 50 illustrates the temporal integration history of the friction velocity u_τ computed on the rods surfaces. Fig. 51 shows the comparison of the instantaneous and time averaged friction velocity. Instantaneous profile perfectly depicts the turbulent nature of investigated flow.

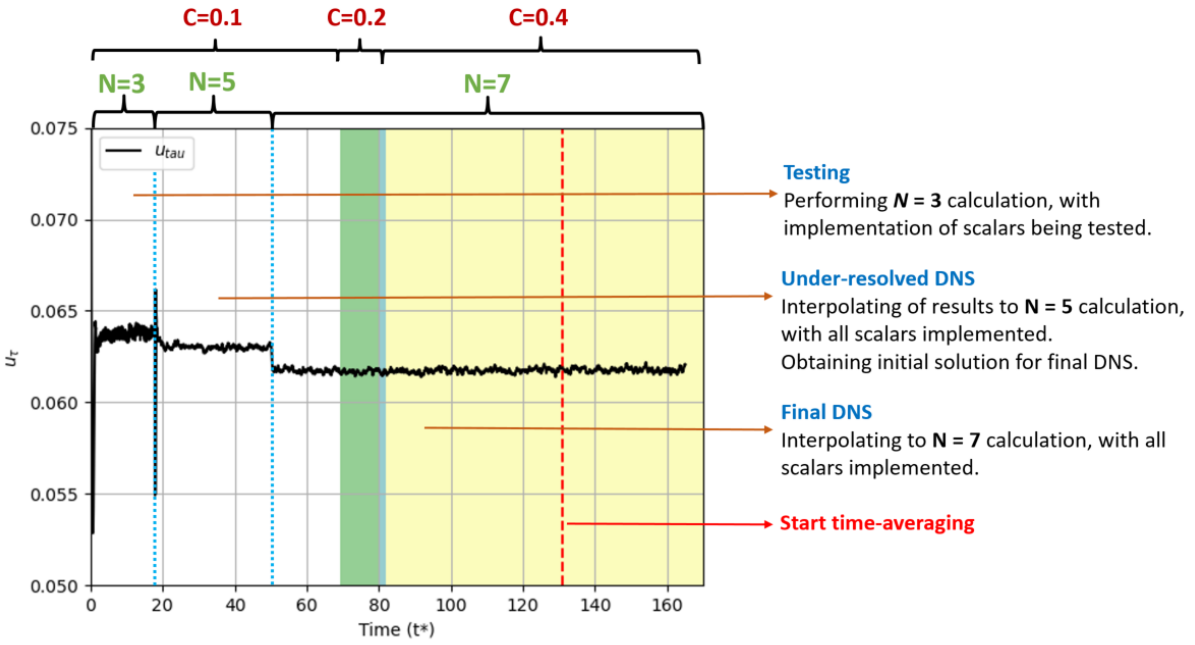

Figure 50: Evolution of friction velocity (u_τ).

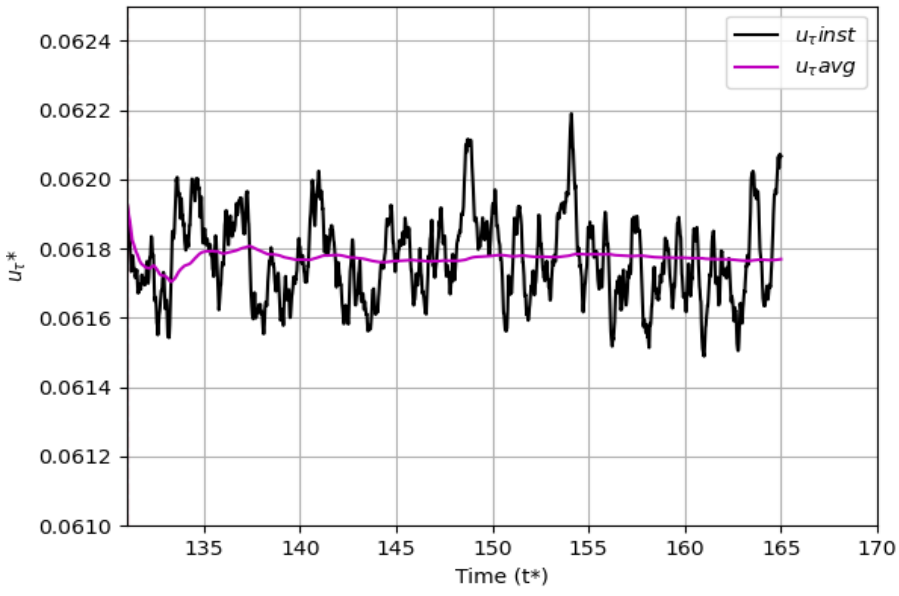

Figure 51: Evolution of friction velocity (u_τ) - comparison of instantaneous and time-averaged.

It can be easily noticed, that flow field reach quasi steady state at $t^* \sim 55$. However, time averaging could not be started yet. The reason of this was the fact, that the temperature fields were not developed. Finally the time averaging was started at $t^* = 131$

Steady state for the wall heat flux - constant temperature BC As it was mentioned before, in the present DNS six thermal fields were introduced as a passive scalars. These passive scalars correspond to the Prandtl numbers of three different working fluids, i.e. water, air, and liquid metal, i.e. Pr = 2, 1, and 0.025, respectively. The heat transfer of these three fluids has been studied in combination with two different boundary conditions at the rods walls, i.e. a constant temperature and a constant heat flux. For the sake of clarity the following naming for the certain passive scalars was introduced:

- for constant temperature (Dirichlet boundary condition):
  1. with Pr = 0.025 is denoted as **PS1**
  2. with Pr = 1 is denoted as **PS2**
  3. with Pr = 2 is denoted as **PS3**
- for constant heat-flux (Neumann boundary condition):
  1. with Pr = 0.025 is denoted as **PS4**
  2. with Pr = 1 is denoted as **PS5**
  3. with Pr = 2 is denoted as **PS6**

In Fig. 52 temporal integration history of the the wall heat flux for PS1-3. Large deviations were observed in interpolation of thermal scalars to higher polynomial (N-) order. In order to avoid divergence of solution, thermal fields were reset to initial condition with interpolation of only the flow field! This is the cause of large spikes seen in heat flux monitors.

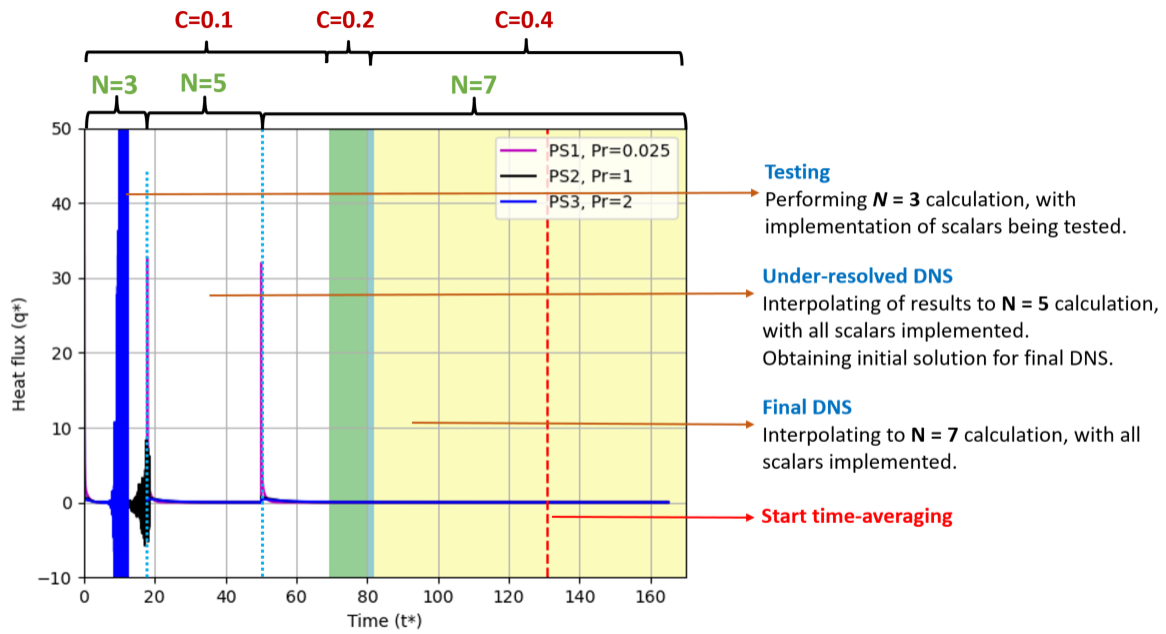

Figure 52: Temporal integration history of the wall heat flux.

Additionally, looking at Fig. 52 one can get the impression that the temperature fields, like the flow field, reached steady state very quickly. It is actually a misleading impression. The reality is completely different. Fig. 53 presented the integration history of the wall heat flux for PS1-3 with the zoomed area, where profiles were approaching the quasi steady-state condition. It is noticed that thermal field for the smallest Prandtl fluid, corresponding to liquid metal, reached statistical steady state relatively fast. This is correlated with the fact, that for fluids with $\mathrm{Pr} \ll 1$, the thermal boundary layer is much thicker than the momentum boundary layer (see Fig. 1). The opposite situation is for the cases with $\mathrm{Pr} > 1$. Here, the thermal boundary layer is much thinner than the momentum boundary layer. As a consequence longer time is required in order to reach quasi steady state. As shown on Fig. 53, the wall heat flux for PS3 reached steady stat at $t^* \sim 120$. This is why the time averaging was started only at $t^* = 131$. Fig. 54 presented the comparison of the instantaneous and time averaged wall heat flux.

The results presented in Figs 52-54 referred to constant temperature

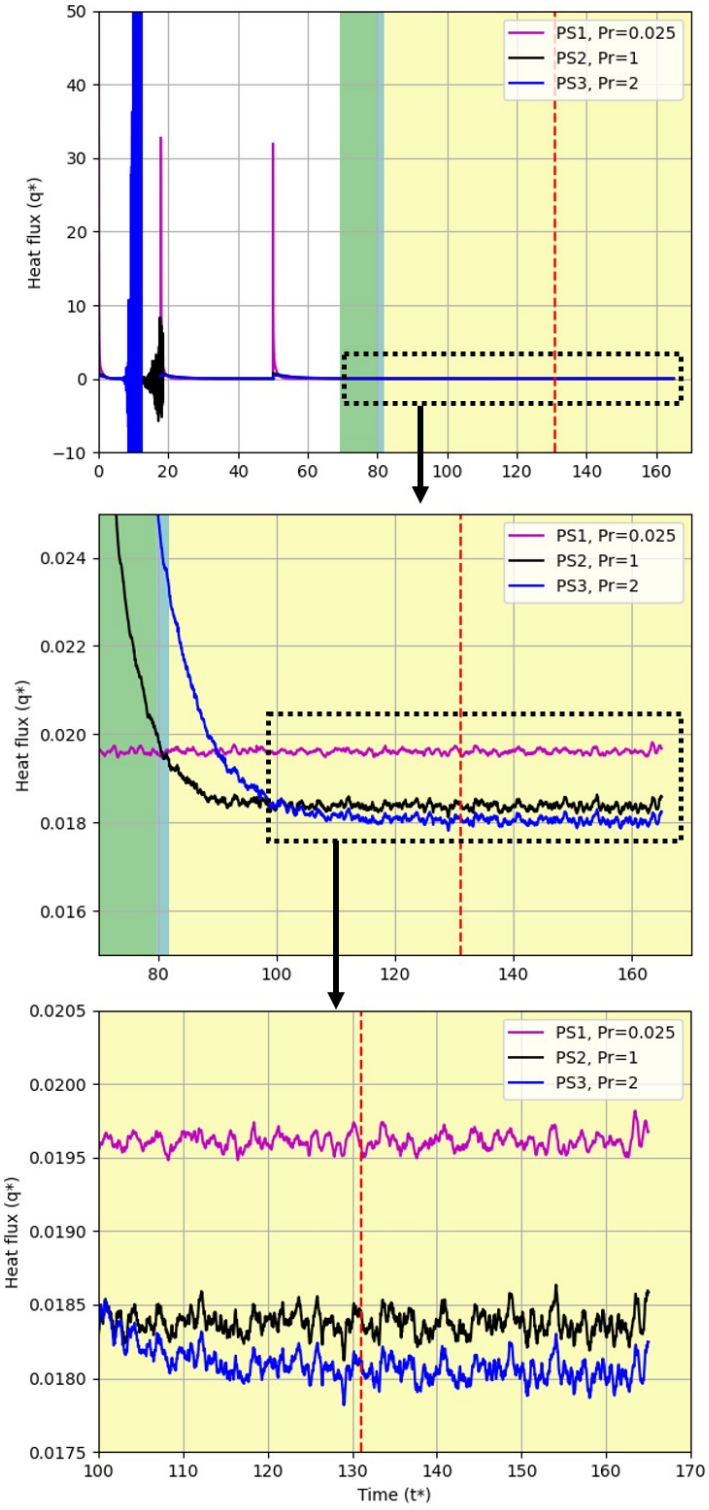

Figure 53: Temporal integration history of the wall heat flux - determination of the statistical steady state.

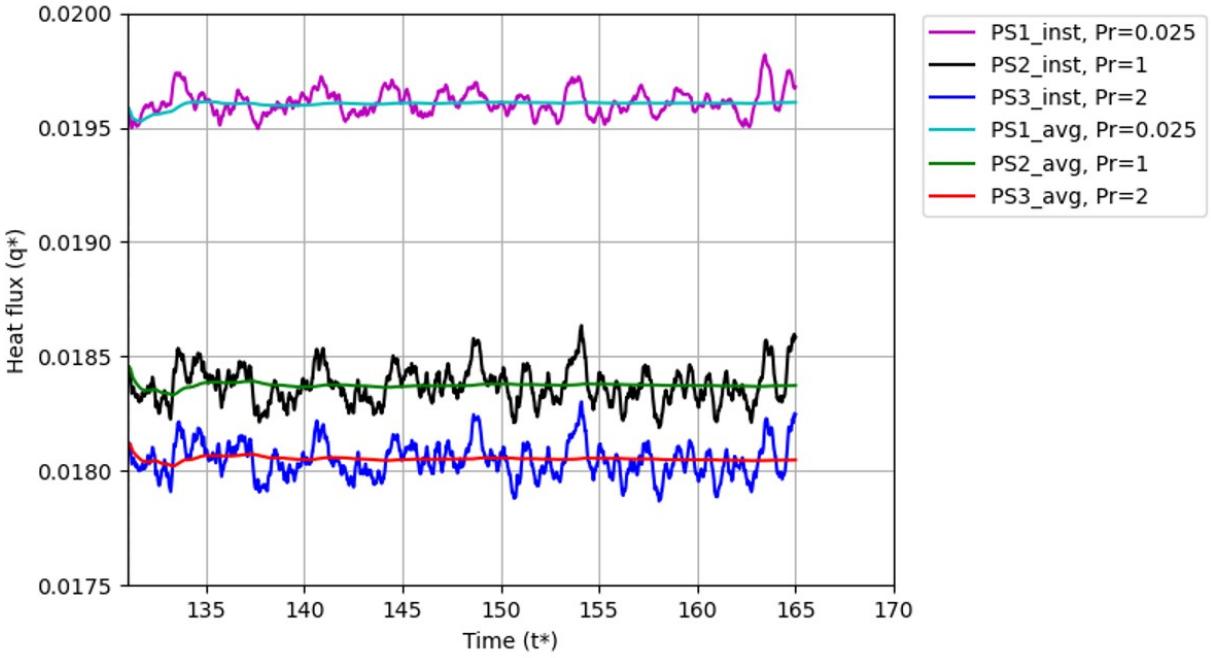

Figure 54: Temporal integration history of the wall heat flux - comparison of instantaneous and time-averaged.

boundary condition cases. Checking the wall heat fluxes for PS4-5 (with Neumann boundary condition) is pointless since this condition is constant heat flux by default. Therefore other monitors had to be proposed as a tool to check statistical convergence of the temperature fields for the PS4-6.

Steady state for the wall heat flux - constant heat flux BC

In order to check some parameters, dozen probes were placed in different locations in the domain. Probes were collecting point-wise different parameters at every time step. Such probes were used in order to check the statistical convergence for PS4-6 locally. As presented in Fig. 55 four point-probes were chosen, in the following locations:

- Probe #21 - exactly in the center of the sub-channel region
- Probe #68 - exactly in the center of the gap region

- Probe #25 - halfway between the gap and the sub-channel region
- Probe #40 - in the gap region very close to the rod wall

In the Fig. 55 probe monitor convergence history for PS1-6 is presented. On the subplots temporal integration history of PS1-6 at different probe locations is depicted. Additionally, the red solid lines indicated the time averaged values of certain passive scalars. As it was stated already, PS1-3 are fully developed. A different situation is observed for PS4-6 (with constant heat flux BC), here only PS4 (with Pr = 0.025) reached quasi steady stated. PS5 and PS6 still are characterized by a downward trend over time, which means that a statistical steady state has not yet been reached for these two passive scalars. Therefore, in this thesis the results only for PS 1-3 are presented and thoroughly discussed.

Explanation, why PS 5 and 6 need much more time in order to reach statistical steady state was given in Section 4.3.5. It was proved that: both boundary conditions display different thermal fields for the respective Prandtl numbers, hence, the resulting DNS would provide extensive database for the validation purpose. For example, looking at Fig. 55 and analyzing profiles for PS1 and PS4 and in particular from Probe #40 (close to the rod wall), one can observe very interesting feature. Namely, profiles characteristics from Probe #40 for Pr =0.025 are completely different for two different temperature BC. Such difference are not observed for Pr = 1 and 2.

5.3.2 Temporal averaging of results

Time averaging was performed over $\sim$ 15 flow-through times (FTT) of the domain. Computed statistical quantities of first and second order statistics are shown and commented in the next subsections. Several different approaches were used to estimate the quality of the gathered statistics. This is of particular importance due to the three-dimensional nature of the aver-

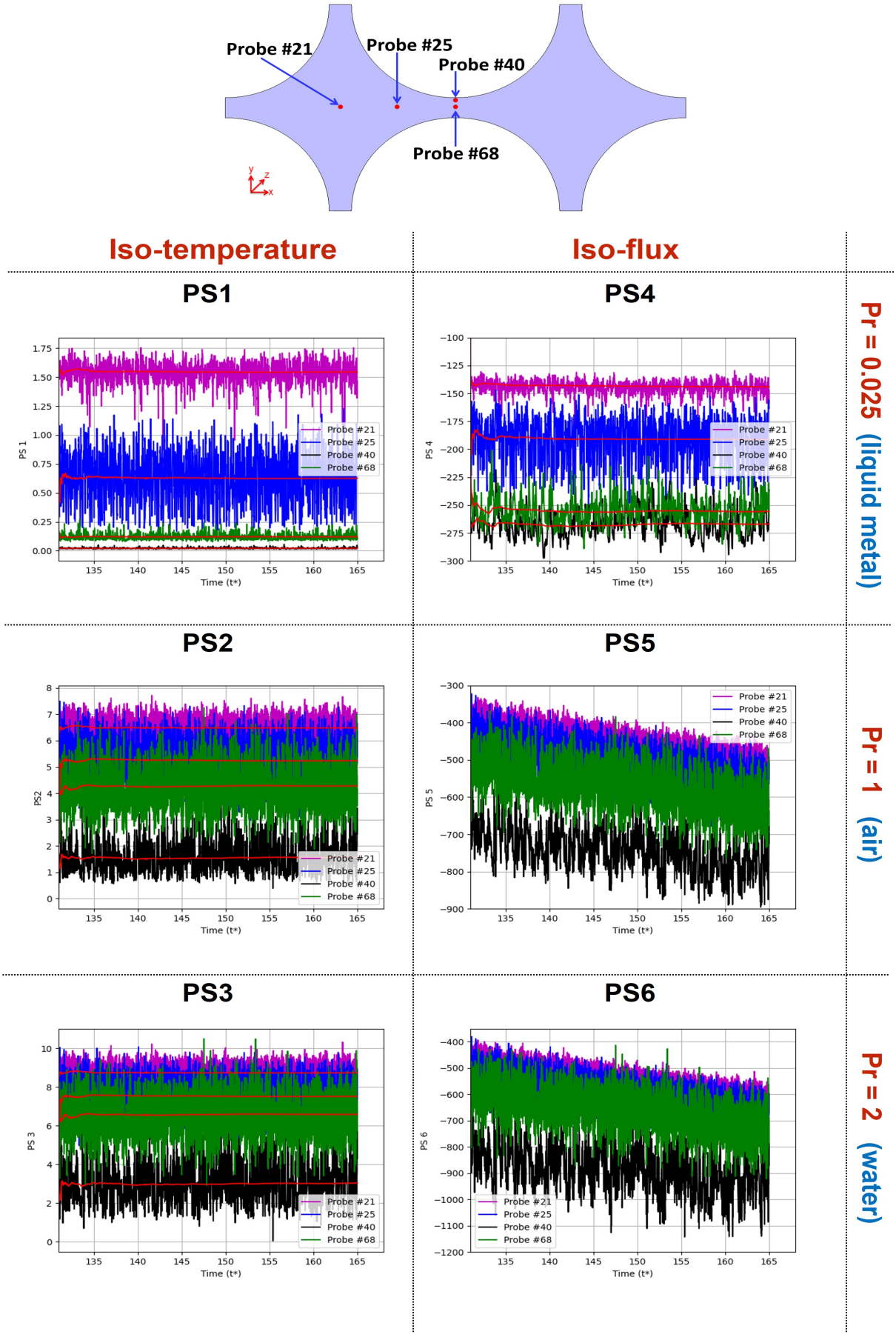

Figure 55: Probe monitors for PS1-6 - instantaneous and time-averaged.

age flow profile in the rod bundle. The vast majority of the contemporary DNS studies was performed in geometries with at least one homogeneous dimension or as per [95, 96] in the channel-flow, as one of the most popular geometries for theoretical DNS studies of the near-wall turbulence, contains two homogeneous directions. Spatial averaging over the homogeneous direction significantly reduces the requirements for long temporal averaging. In the study [97] with the backward-facing step (BFS) geometry with two-dimensional average flow pattern, the averaging times are below 10 flow-through times, which was declared as sufficient since the spatial averaging complements the temporal one.

The stochastic nature of turbulence essentially makes the time-averaging equivalent to spatial-averaging. Therefore performing a spatial averaging provided the converged statistics much faster. If spatial averaging is not performed, then time-averaging required a longer period. In current DNS, spatial averaging was performed in z-direction. This reduced the time-averaging period a lot. Additionally, the spatial averaging in the cross-section was introduced. This further reduces the time period needed to get the converged statistics.

The spatial averaging in the cross-section

In Fig. 56 the velocity fluctuations $u^{'}$ contour is presented. The observed flow pattern is actually symmetric around so-called a 'unit cell'. This unit cells is highlighted by dashed white lines. Lines #1a-3a are boundaries of single unit cell. In Hooper domain, 16 such unit cells can be mapped out as presented in Fig. 56 and 57.

However, averaging all 16 unit cells into one single cell cannot be done. It is because the shortest edge for the central (in gap region) four unit cells is not a wall. But for all other unit cells, the shortest edge is a wall as presented in Fig. 57 *a*). Therefore the unit cell cannot be averaged

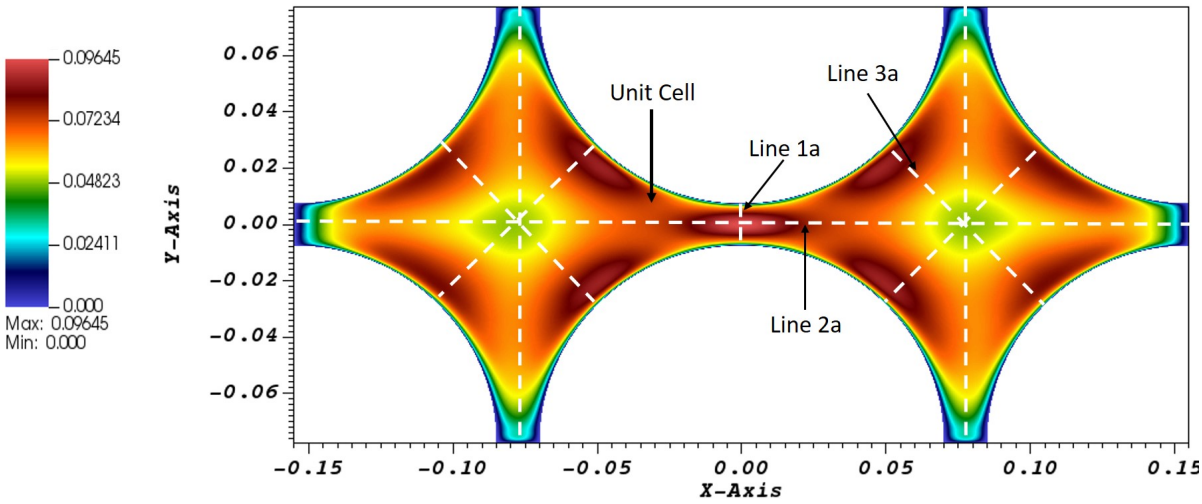

Figure 56: Mean velocity patterns in unite cells.

16 times. But it can be average of four times. Something like folding the 2D plane in y-direction and x-direction. That way, all the wall edges will only be averaged with other wall edges. The resulting domain would look like shown in Fig. 57 *b*). By doing this, the total time required for time-averaging was reduced even more. The results of cross-section averaging of velocity fluctuations $u^{'}$ contour is presented in Fig. 58. The colours are not exactly the same saturated because the images were rendered in different softwares.

Finally, the quality of the gathered statistics were checked along unitLines highlighted and defined in Fig. 57 *c*).

In typical statistical analyses, the errors are usually given as relative values. However, average values of several computed statistics in various monitoring points are around zero. Computing the relative errors does not make sense for such quantities in these monitoring points.
Error calculated in the entire field:

$$\varepsilon_{\phi} = \frac{|\phi_1 - \phi_0|}{\phi_1} \tag{5.6}$$

however, denominator in this equation approaches zero in certain regions.

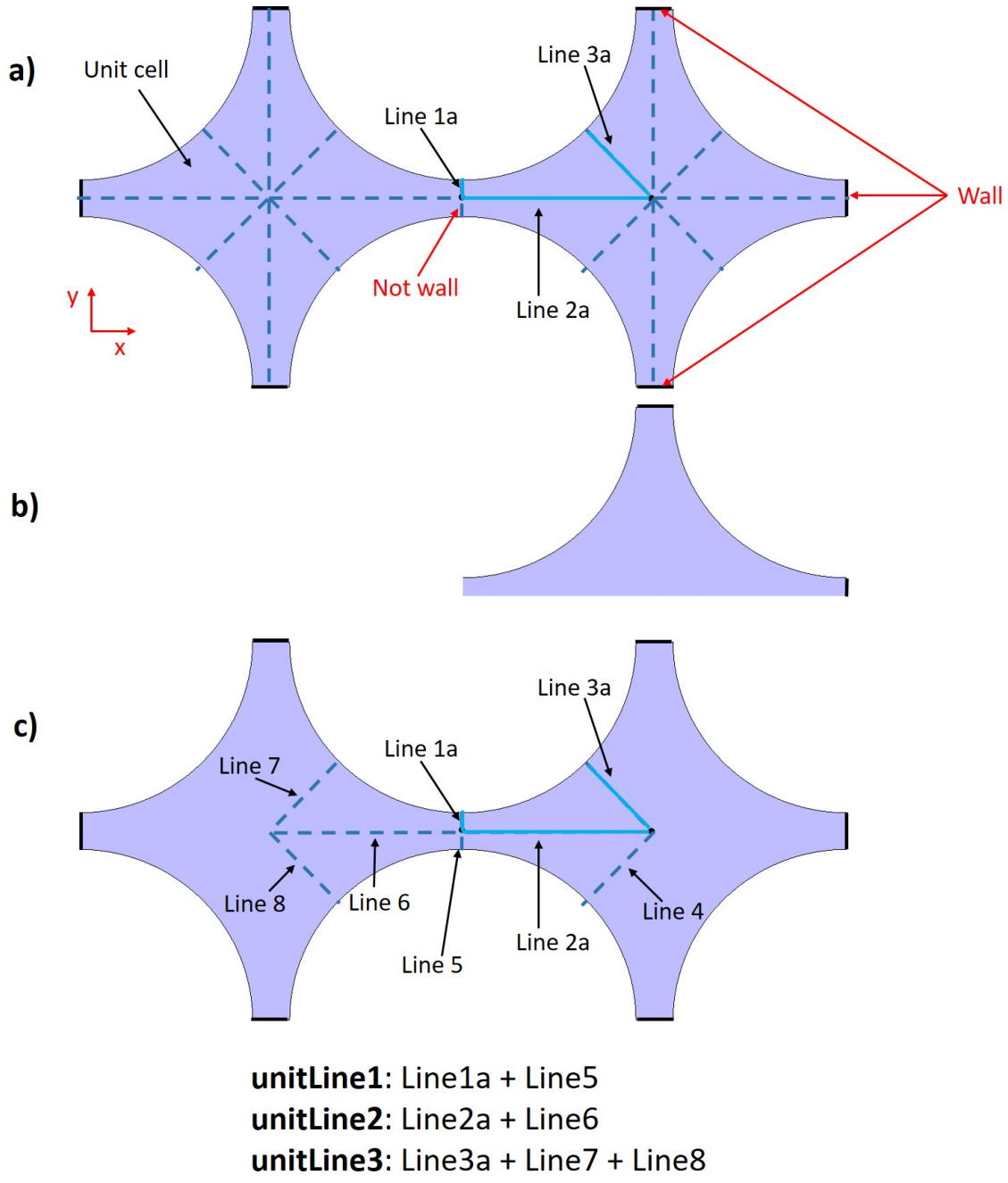

Figure 57: Unit lines in Hooper geometry.

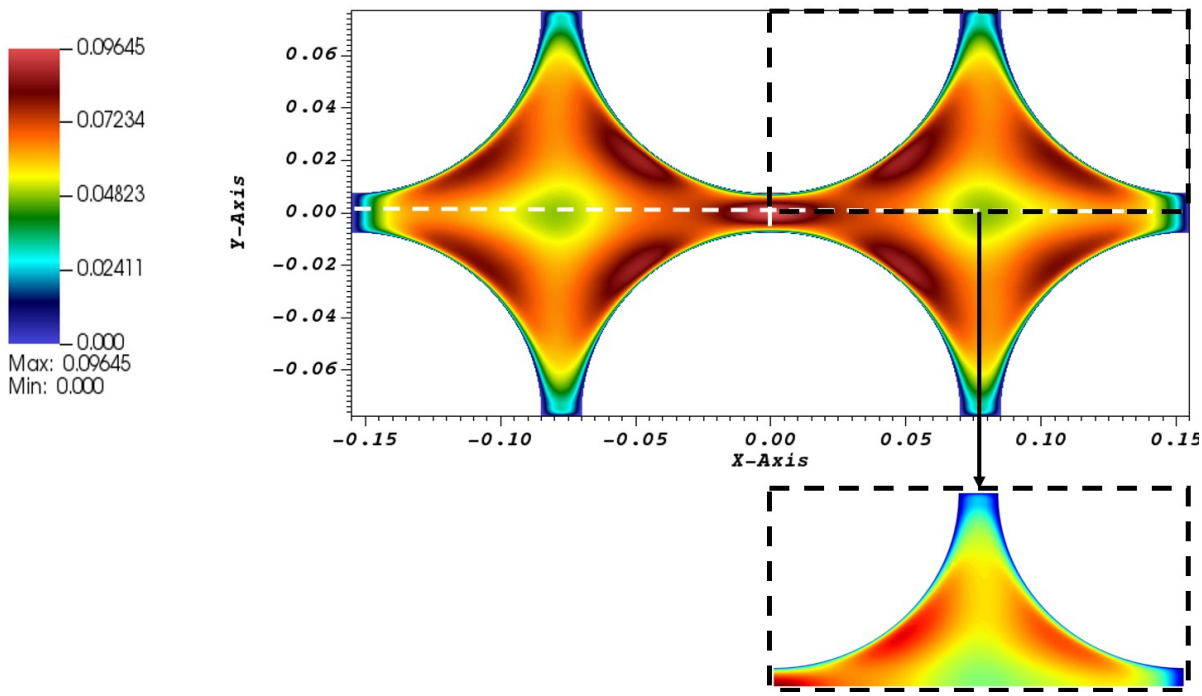

Figure 58: Cross-section averaging of mean velocity.

Therefore, it was decided to calculate integral error on the lines:

$$\varepsilon_\phi = \frac{\int |\phi_1 - \phi_0|}{\int \phi_1} \tag{5.7}$$

In order to check the quality of statistical quantities, the errors between two different time steps were compared, namely data collection for 10 FTT and 15 FTT were compared. The results of unitLine errors computed along unitLine 3 are presented in Table 8.

Table 8: Errors between 10 and 15 FTT.

	u	v	w	PS1	PS2	PS3	PS4	PS5	PS6
avg	5.06	14.87	0.03	0.06	0.03	0.02	0.04	3.51	3.76
rms	0.21	0.13	0.14	0.27	0.14	0.12	0.46	15.44	16.87
covu	0.37	0.59	1.99	1.28	1.49	1.58	2.23	0.94	0.90
covv	0.59	0.24	1.66	1.35	1.55	1.60	1.98	3.74	4.31
covw	1.99	1.66	0.24	0.33	0.22	0.19	0.55	1.92	2.24
dissipation			0.15						

The errors were computed for the first order statistics (mean values) and second order statistics (fluctuations, Reynolds stresses and turbulent

heat fluxes). For most of the quantities errors between two time steps are lower than 1%. The highest values can be noticed for PS5 and PS6, however, it was already explained that those passive scalars did not reach the quasi steady state and longer time is needed to fully develop these thermal fields. The errors for the average values of u-velocity and v-velocity components are quite high. Nevertheless, for the thesis perspective the most important is the streamwise velocity component (w), which is the dominant component. Comparing $u-$ and $v-$velocity components to the $w-$velocity component the difference of three-four orders is observed. Therefore, the streamwise velocity component will be used for the turbulent model validation purpose, in details presented in Section 6. Finally, it was concluded that the gather of statistical data is reliable and high fidelity, and could be used as a reference database for further turbulent model validation purpose.

5.4 Results of DNS

5.4.1 Analysis of the velocity field

The wall distribution normal to rod surfaces is calculated as a function of u_z^+ and y^+, to obtain profiles that conform to the law of the wall. Definitions of all dimensionless quantities were given in Section 3. Subscript 'z' indicated streamwise velocity and quantities are normalized with the local value of friction velocity (u_τ). Figure 59 showed the viscous sublayer with $u_z^+ = y^+$ and the log layer with Kármán constant $\kappa = 0.41$ and the constant $C^+ = 5.1$. Overall, the viscous sub-layer is captured using DNS, and the log-law region matches well with distributions found from turbulent empirical data. Along L3 toward the sub-channel center in Fig. 59, velocities match perfectly with the log-law region for DNS. The obtained results are compared with those measured in the hydraulic experiment performed by Hooper, Wood and Crawford [98]. Looking at the experimental data one can notice that for the lowest Reynolds number $Re = 22600$ the velocities

are under-predicted. This new finding reveals that even the lowest Reynolds number corresponds with the logarithmic law, contrary to Hooper and Wood′s [26]. In fact three highest Reynolds numbers of the four measured in experiment followed the log-law region. The explanation for this difference is that the wall shear stress at the lowest experimental Reynolds was over-predicted because of uncertainties in measurement techniques [26]. The last check made was analyzing documented viscosities in [98]. It was noted that values vary in a non-linear way from 1.622×10^{-5}, 1.475×10^{-5}, 1.644×10^{-5}, and 1.769×10^{-5} m^2/s respectively for increasing Re numbers. Even small uncertainties in kinematic viscosity could influence the reported Reynolds number, which can alter the friction velocity. In the gap region, velocities also matched with the viscous sub-layer. For the log-law region, velocities went slightly above the theoretical value because of their proximity to the opposing rod. The length of L1 went only up to $y^+ = 10^2$. The distribution follows logarithmic law to a great extent and confirms the consistency of DNS calculations.

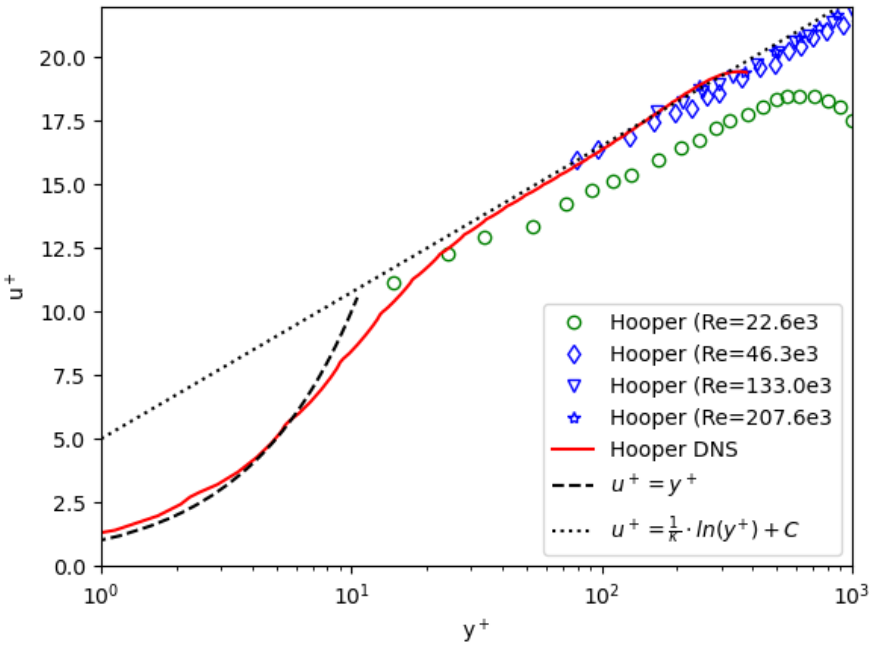

Figure 59: Mean velocity profile along L3.

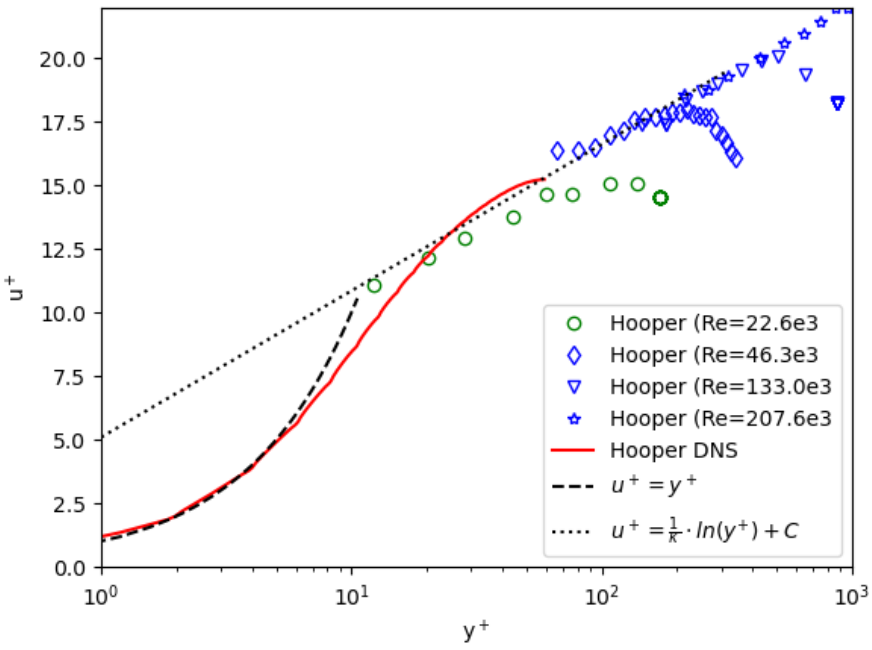

Figure 60: Mean velocity profile along L1.

5.4.2 Wall Shear Stress

The average wall shear stress in the azimuthal direction was calculated using the near-wall velocity gradients from DNS calculations. Results were computed at every 5° across the surface of center rod, as it is shown in Fig. 61. Additionally, the results were compared with the experimental data [98]. This data was collected across the center rod and normalized using the mean wall shear stress ($\tau_{w,m}$) between $0° \leq \theta \leq 45°$. The same normalization was applied for the calculated results. Both profiles in Fig. 61 are nearly identical. Overall, there is good correlation between experimental data [98] and DNS calculations. DNS has great symmetry, since the model considers perfectly smooth and symmetric rods.

5.4.3 Turbulent kinetic energy

In Fig. 62 the normalized turbulent kinetic energy (TKE) k was presented. TKE was normalized by local friction velocity u_τ and was calculated along

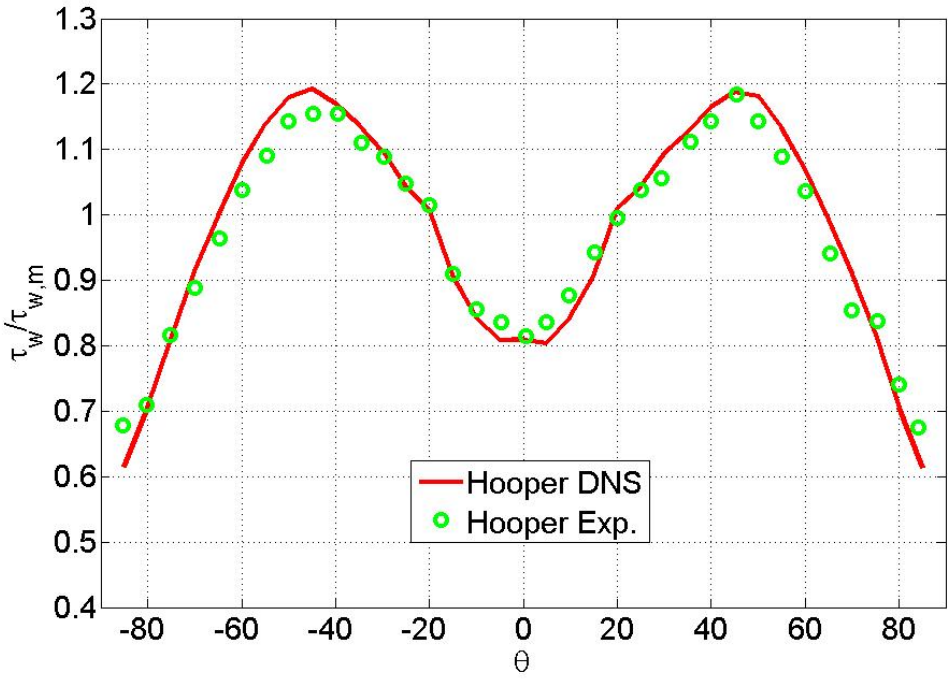

Figure 61: Wall shear stress across surface of center rod.

L1 and L3. The length of these lines was normalized as:

$$L^+ = \frac{L}{L_{max}} \tag{5.8}$$

where L is the length of certain line, L_{max} is the distance to the lines centers. This means $\frac{L}{L_{max}} = 1$ becomes a point of symmetry for statistics at L1a and L3a. The TKE near the wall is highly characteristic for any turbulent flow. An initial peak in fluctuations is present before they begin to decay toward far-wall regions of the geometry. One feature to observe is that the maximum normalized k decreases as the angle goes closer to the gap center. On the other hand, the relative location of the maxima increases as the angle decreases. This variation in k attributed to geometrical effects may contribute to the difficulty of RANS models for capturing the proper energy in this flow.

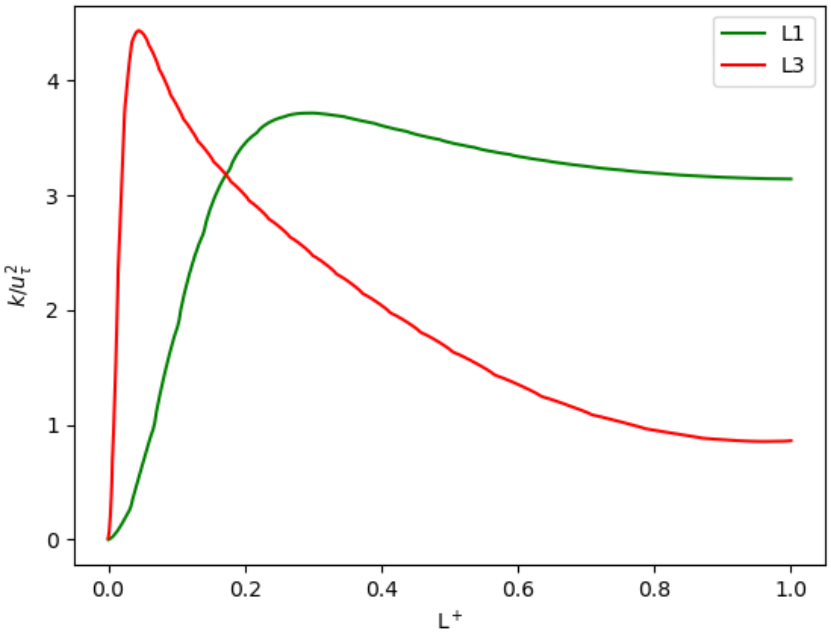

Figure 62: Turbulent kinetic energy along L1a and L3a.

5.4.4 Momentum frequency

The flow in a tightly spaced rod bundles is characterized be the appearance of gap vortex street [26,59,85,98,99]. These specific pattern can be identify by dominant frequency f. Instantaneous velocity values were collected at various locations, in order to reveal a characteristic frequency for this P/D ratio.

The Welch's method [100] was used to estimate the power spectral density (PSD). In Fig. 63 PSD was calculated in the centre of gap region, at Probe #68 (exact location of different probes was explained in Section 5.3.1 and shown in Fig. 55). In this location PSD occurs at 3.7 Hz, the majority of the energy lies within this frequency, and high frequencies are minimal. Also observation of the instantaneous spanwise velocity profile showed characteristic oscillatory behavior at this location. The Strouhal number defined as:

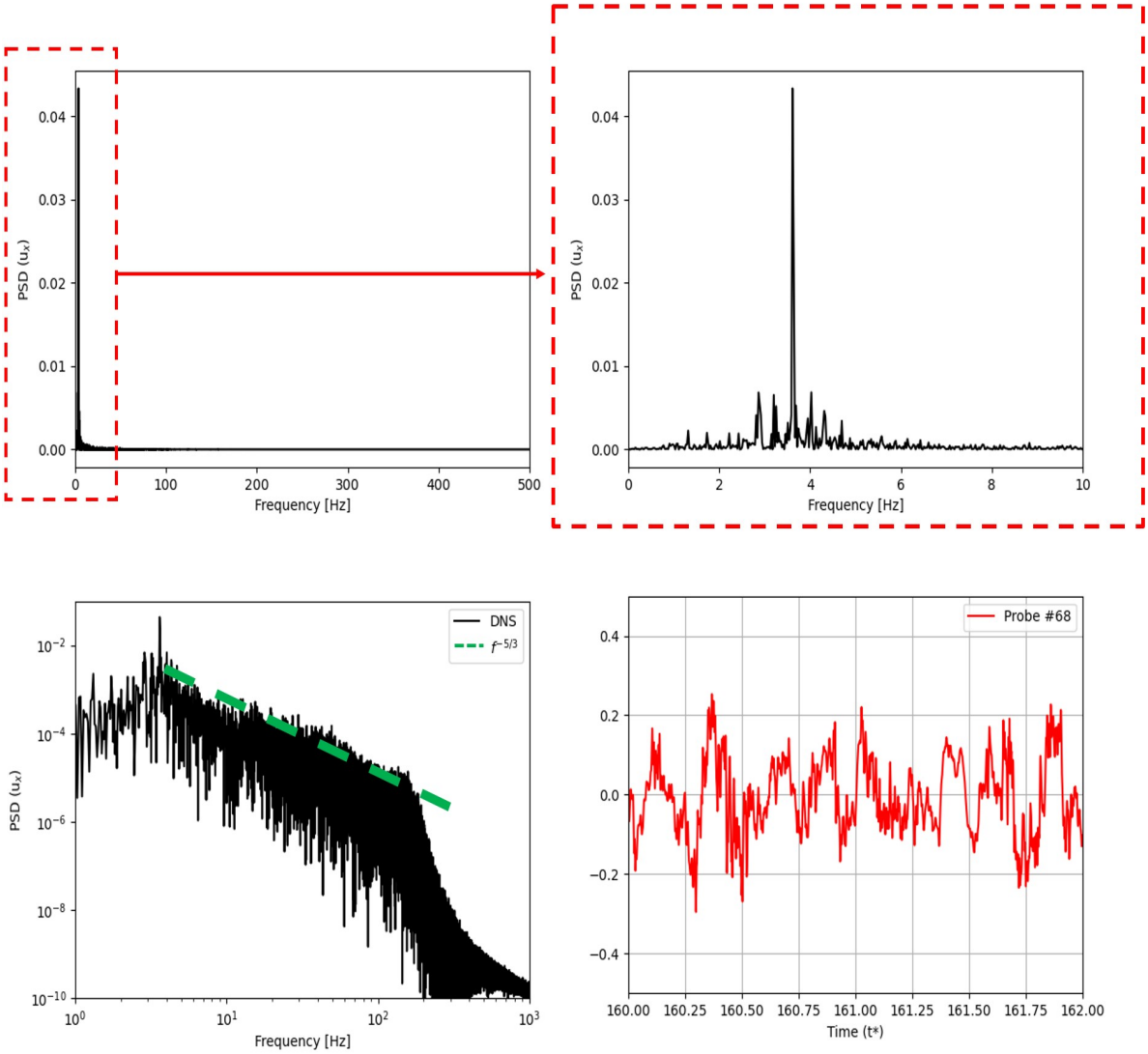

Figure 63: Power spectral density of x-velocity in the middle of gap region (top and left bottom) and instantaneous x-velocity (right bottom).

$$St = \frac{fL}{U}, \tag{5.9}$$

(where: where f is the frequency of vortex, L is the characteristic length (for example, hydraulic diameter) and U is the flow velocity), was calculated and yield to 0.48, indicating that pulsations are large-scale in nature.

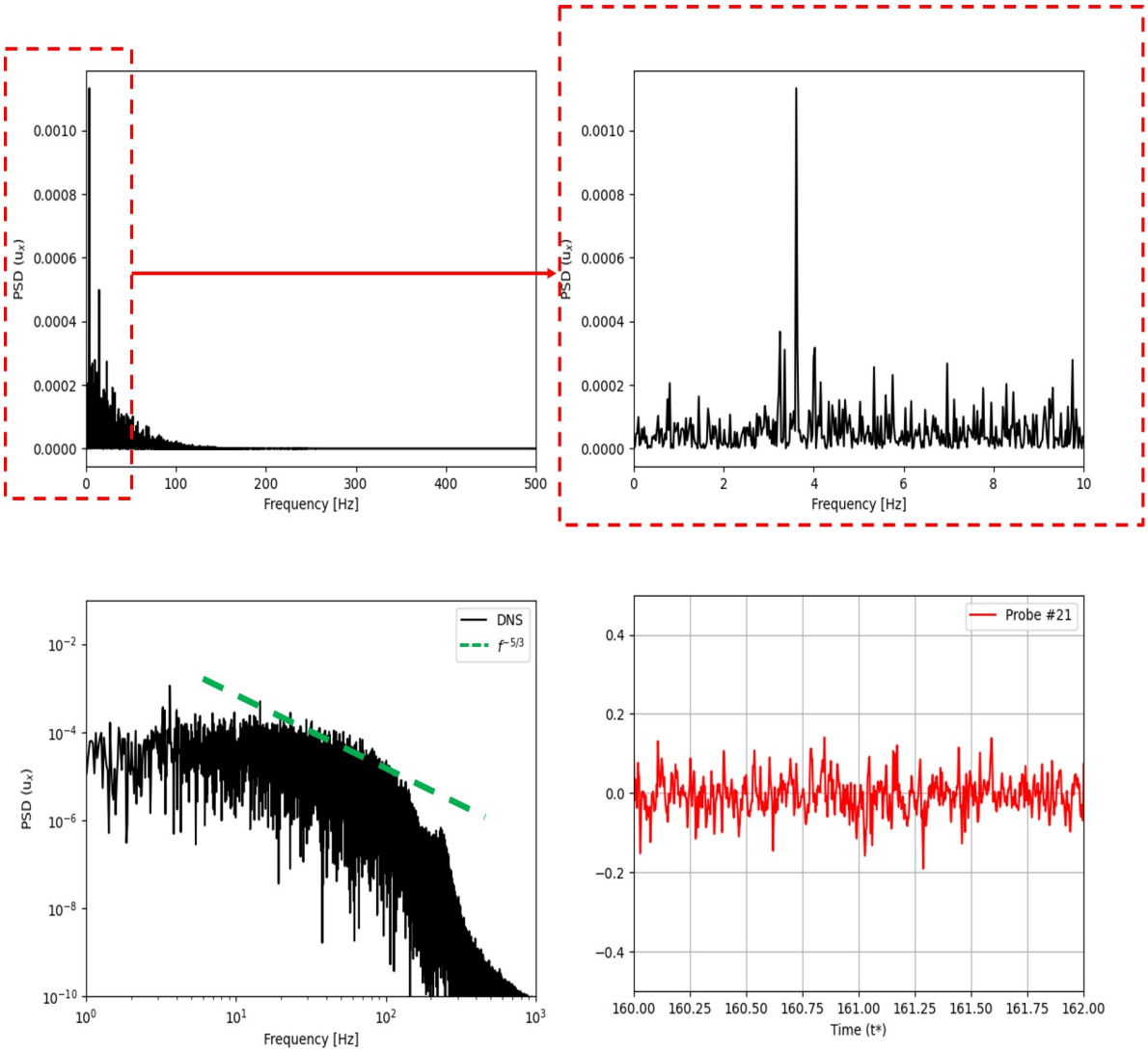

Figure 64: Power spectral density of x-velocity in the middle of sub-channel region (top and left bottom) and instantaneous x-velocity (right bottom).

PSD of observed pulsations was check in the other location as well. Here the results from the Probe #21, thus from the center of the sub-channel region are discussed and presented in Fig. 64. While the location

is farer from the walls, determination of the characteristic frequency becoming less prominent. It is due to the fact, that this region is governed by local turbulent effects. Energy more clearly cascades to higher frequencies and multiple small peaks appeared in the PSD plot. Nevertheless, still one dominant peak was observed at 3.7 Hz, indicating that this frequency could be a governing characteristic at other locations as well. Comparing the instantaneous spanwise velocity profile at this location with the characteristic in gap region, it can be noted that the amplitude of pulsations is smaller and values are changing more frequently.

Although not showed in this thesis, analyses of PSD at other locations have also been conducted and for transverse and axial velocities. In general, PSD of the streamwise velocity u_z is characterized by the set of multiple peaks of characteristic frequencies. In contrary, the energy within u_y has no spectral peak that stands out among the wide range of frequencies. This characteristic is partially attributed to the wall boundaries, suppressing pulsations in the y direction for this geometry.

5.4.5 Instantaneous velocity field

In Fig. 65 the contour of the instantaneous velocity was depicted. It is easily noticed many scales of motion captured by DNS. Whereas URANS techniques would have steadier gap vortex street pattern in the gap region, DNS revealed other turbulent effects as well. Since the flow pulsations are moved side to side in the gap, mass is being exchanged from one sub-channel region to another one. This, in turn, causes that the turbulent kinetic energy in one sub-channel increases, the energy in the other sub-channel decreases. Since this geometry does not represent an infinite rod array, wall effects of the bonding walls suppress pulsations from occurring at other gap locations.

Additionally, one can observe that in the sub-channel region whirls are much larger. As the fluid approached closer to the walls, turbulent whirls

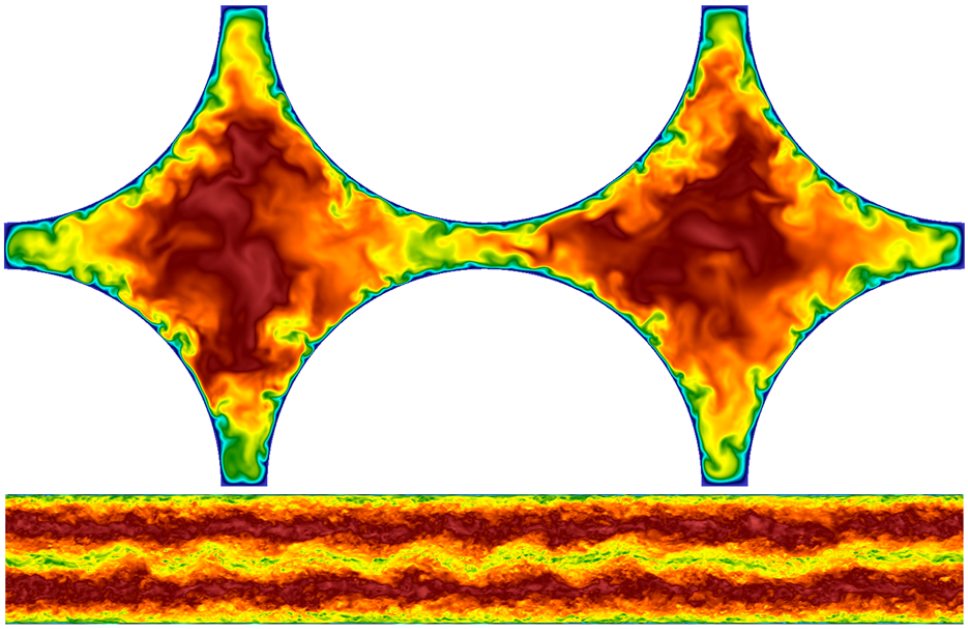

Figure 65: Contours of the instantaneous velocity field in cross section (top) and streamwise plane (bottom).

increase in number, but decrease in size. The scales of motion are much smaller near the wall, which allow these effects to be fully captured. The large structures around the sub-channel regions are not unidirectional and tend to follow a sinusoidal path - clearly visible in bottom plot presented in Fig. 65. This characteristic is an expected feature for bare rod bundles with low P/D as discussed by the work of Tavoularis [13].

5.4.6 Analysis of the thermal field

In this section, the average and instantaneous thermal fields are analysed. It is worth recalling that constant fluid properties are considered, hence the temperature is a passive scalar. The DNS has been performed with six passive scalars (PS): for three different coolants, corresponding to water, air, and liquid metal, in combination with two different thermal boundary conditions (BC): iso-thermal boundary conditions (denoted as PS 1, PS 2, and PS 3) and iso-flux boundary condition (denoted as PS 4, PS 5, and PS 6). The thermal field obtained with iso-thermal boundary con-

ditions is analysed only, since the thermal fields with iso-flux BC did not reach yet the statistical convergence. Nevertheless, some preliminary results were also highlighted in the theses for Neumann BS (mainly by means of instantaneous field).

5.4.7 Instantaneous profiles of thermal field

The temperature contours of six passive scalars are consider qualitatively and are presented in Fig. 66 in cross-section and in Fig. 67 along streamwise plane. The influence of Pr number was observed, namely Pr number influencing/changing the scales of motion within the energy equation. The temperature magnitudes were, different but still comparable with scaling.

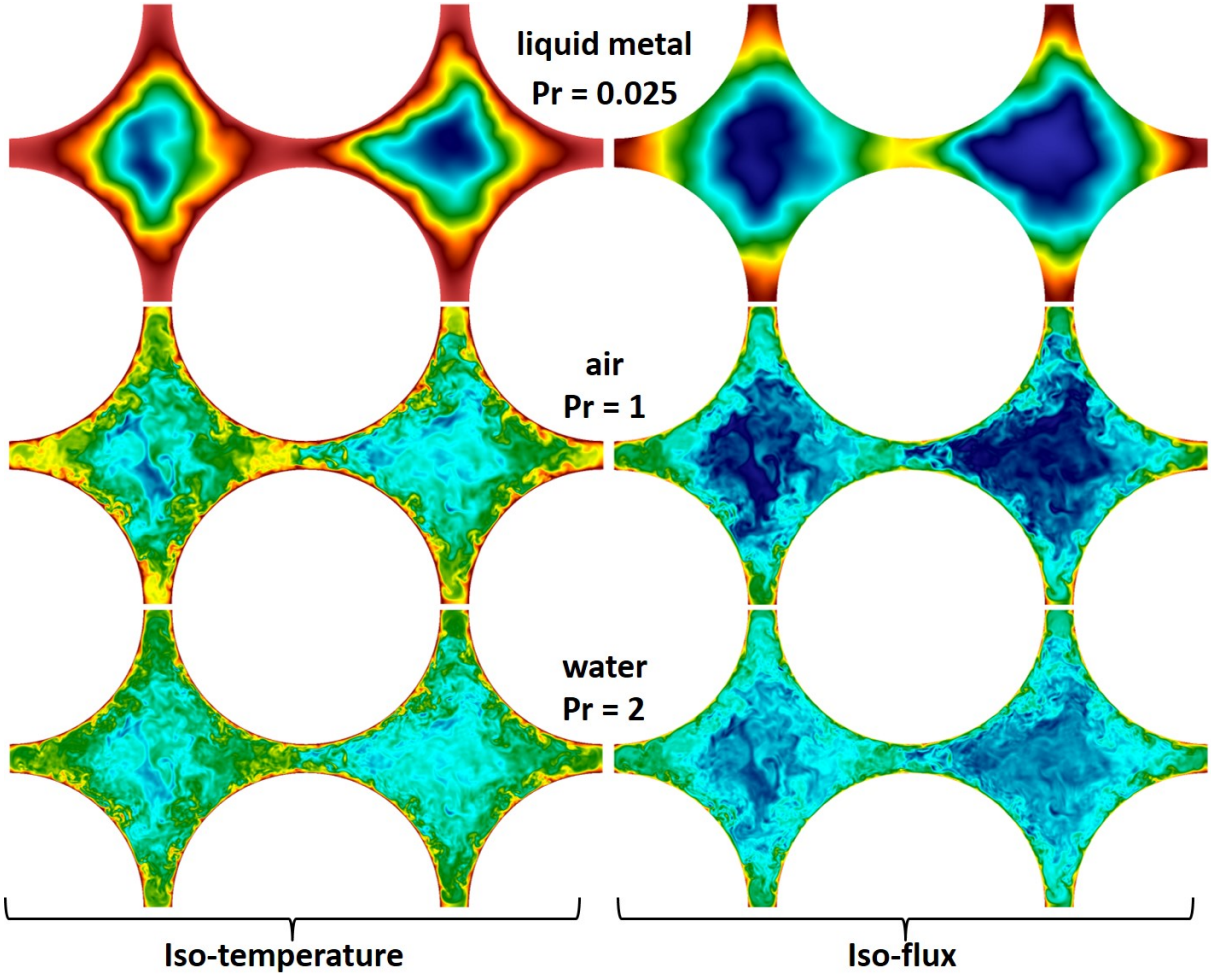

Figure 66: Contours of the instantaneous temperature profiles with iso-thermal (left) and iso-flux (right) BC for three Prandtl fluids.

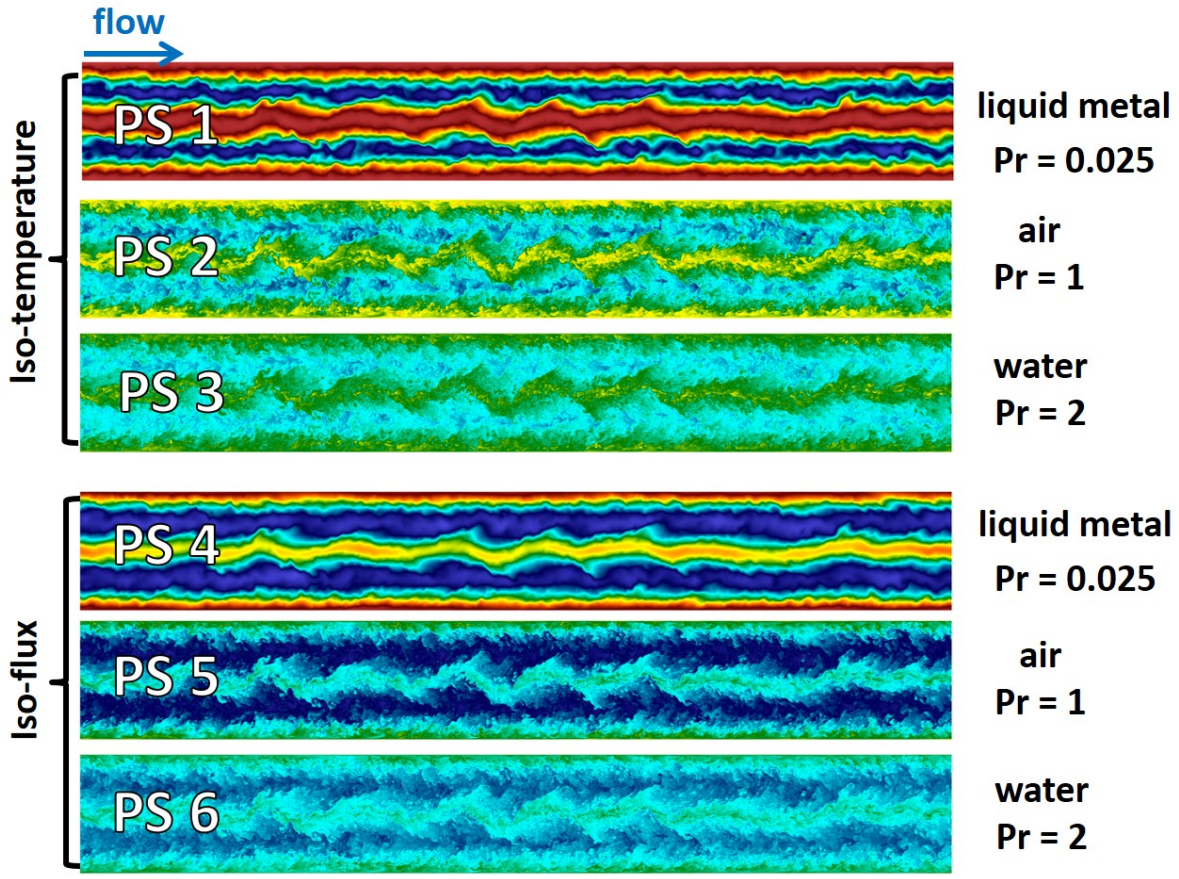

Figure 67: Contours in the streamwise direction of the instantaneous temperature for six passive scalars.

For the highest investigated Pr number (PS 3 and PS 6), the temperature has much steeper gradients than its respective contours at the same time. Moreover, the heat transfer characteristics become very complex. The contours of Pr =1 (PS 2 and PS 4) looks the closest velocity contours (which were presented in Fig. 65) since momentum (δ_m) and thermal (δ_t) boundary layers are equal. While the Pr number decrease to the smallest number, corresponding to the liquid metal fluid, the temperature field became smoother, allowing the overall temperature to be closer to the bulk temperature. Even with this very high thermal conductivity, gap vortex street within the gap region was still observed, whereas temperature at the bounding walls became roughly constant. This qualitative observation demonstrated that the large pulsating effects of the gap still have an

significant influence on the thermal field even for the lowest Pr number coolants.

5.4.8 Thermal frequency

Similarly as for momentum, the frequency of temperature was computed. However, in order to properly compare energy in the frequency spectrum for temperature, the magnitude of the signals must be the same. Therefore, the amplitude of the signals was normalized to one by dividing the fluctuations by three times the standard deviation (σ), since this mathematically lies within the 99.7 percentile. Fig. 68 depicted the power spectral density of

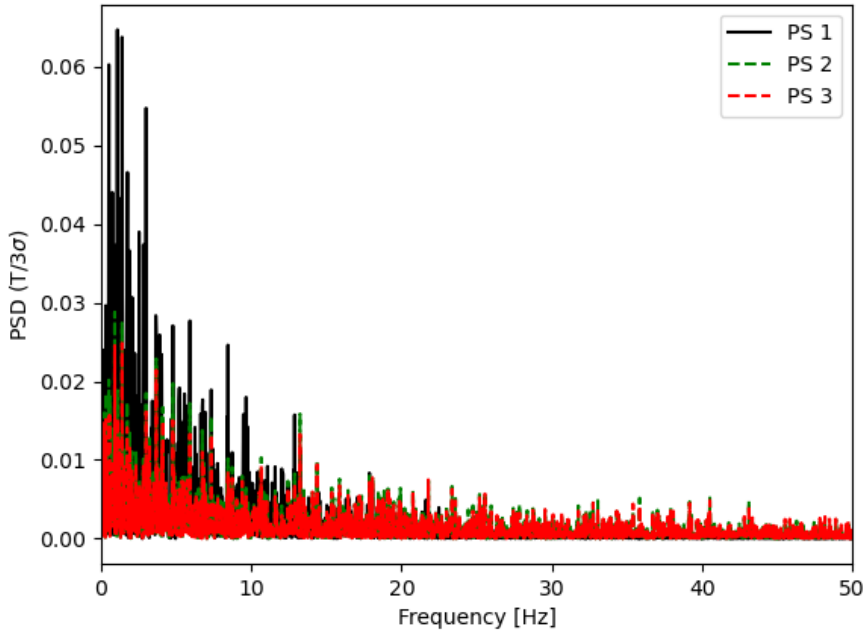

Figure 68: Power spectral density of temperature in the middle of sub-channel region.

temperature in the middle of sub-channel region (at Probe #21). It can be noticed that peak frequency shifted from lower to higher frequencies as Pr increases. This feature was expected, since Pr increases, energy in low frequencies is transferred to the higher frequencies. This pattern is prominently visible up to 10 Hz where energy is systematically lower as Pr number increases.

A different behavior was observed in the gap region. The narrow gap suppresses the higher frequencies, and the low frequencies are uniquely characterized, as presented in Fig. 69. One can notice that the characteristic frequency of 3.7 Hz is present, the same as for the momentum. However, for 1 Hz and between 6 and 8 Hz, additional peaks were observed, which manifested itself differently depending on the Pr number. These additional peaks became prominent at low Pr and were higher in intensity than the primary peak at 3.7 Hz. A similar mechanism (as in the sub-channel region) is likely to act at low Pr number. Energy is transported with larger scale motions, while transport through smaller eddies is less dominant because of the high value of thermal conductivity. As Pr increases, the smallest scales play a larger and larger role.

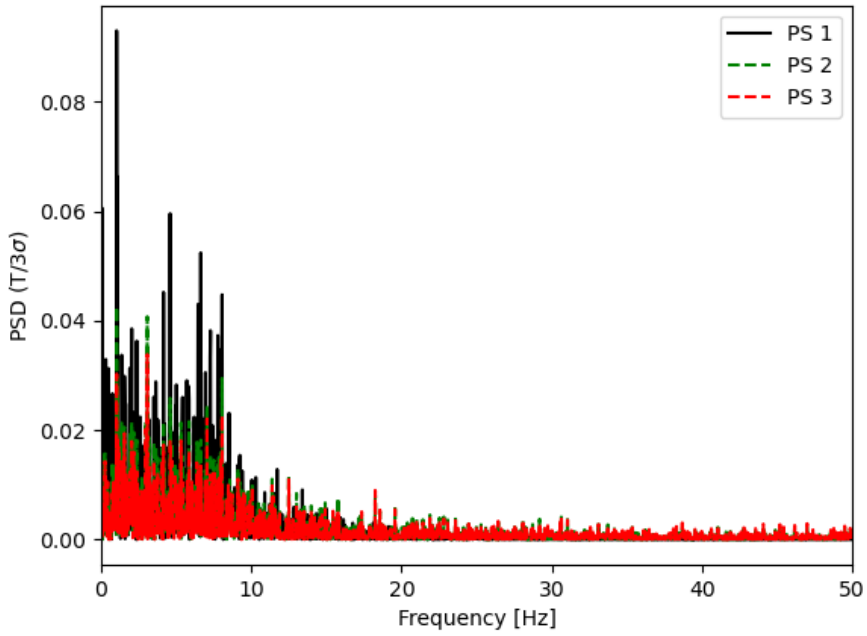

Figure 69: Power spectral density of temperature in the middle of gap region.

5.4.9 Average temperature profiles

Average temperature profiles in different locations, namely in the gap (along L1) and sub-channel regions (along L3) were investigated. Here-

after, all the results will be presented at half the length of the lines L1 and L3 (so actually along L1a and L3a), thus L^+ is varying 0-1. In order to compare the profile from different coolants, the temperature was normalized, presented as scaled temperature θ, which was defined in Section 4.3.3, see equation (4.2). In Fig. 72 scaled temperature along Line 3 are presented. For different Pr number the difference in near-wall ($L^+ = 0$) gradients for profiles toward the sub-channel center ($L^+ = 1$) is clearly visible. The gradients in temperature became much smaller, while thermal conductivity is increasing with decreasing Pr number. For Pr = 1 and 2, the relative temperature are nearly the same in magnitude. Additionally, profiles at location $\sim L^+ = 0.1$ break and begin to flatten out. Completely different characteristic is observed for the lowest Pr number (liquid metal). In this case the profile starts to smooth around the center of the line. This feature exemplifies one of the major difficulties that is involved in predicting heat transfer for liquid metals and is a challenge for the RANS models.

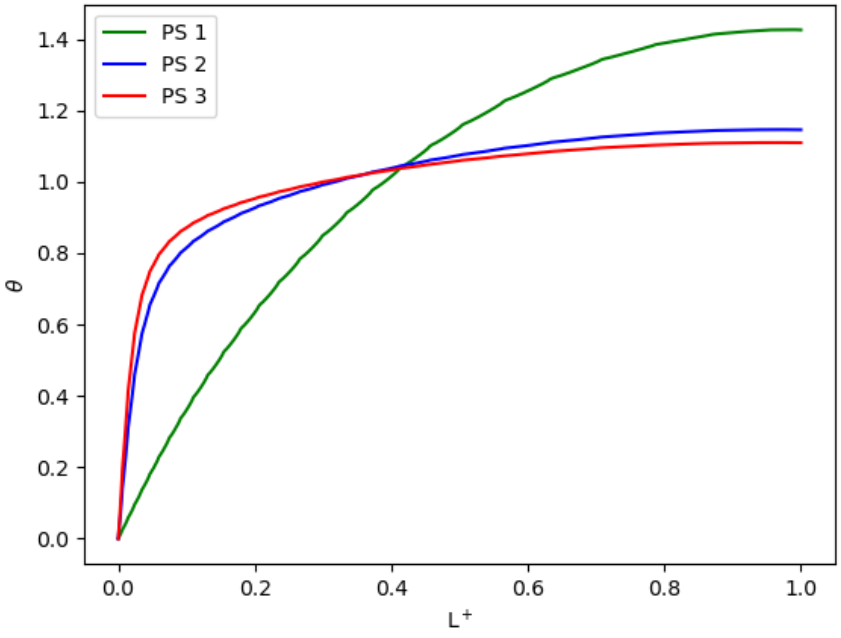

Figure 70: Mean temperature profile in the sub-channel region.

The similar trends are observed in the gap region, as illustrated in

Fig. 73. However, profiles for Pr = 1 and 2 are not so sharp close to the wall-region and they more closely resemble the characteristics of the profile for Pr = 0.025. Nevertheless, the break point can be observed from which the profiles begin to flatten out, although now it is around $\sim L^+ = 0.4$, so much farther from the wall. The proximity of two adjacent rods in this location causes the radial temperature to become extremely high. This leads to smaller variations in radial.

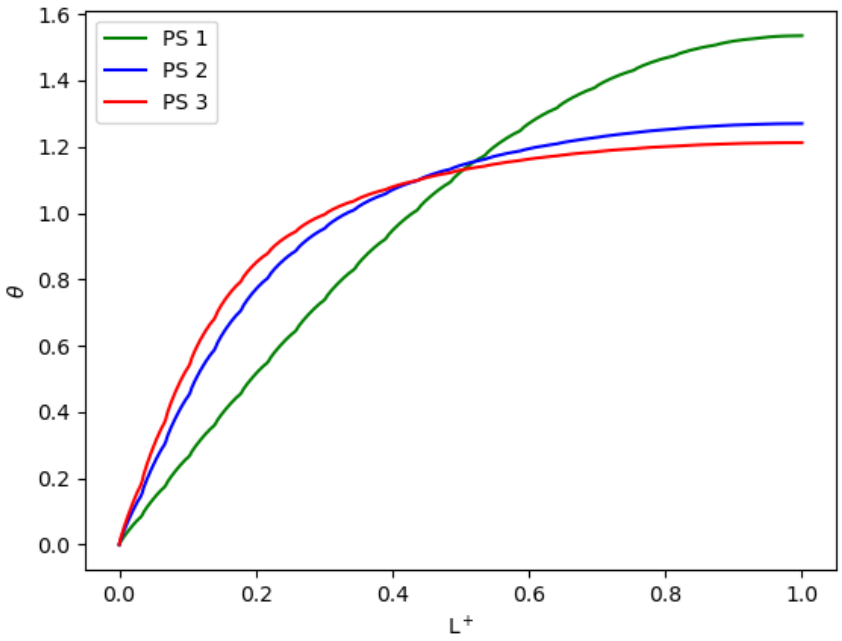

Figure 71: Mean temperature profile in the gap region.

5.4.10 Temperature Fluctuations

Due to the existence of gap vortex street and large swirls in the tightly spaced rod bundles, the temperature fluctuations became very important to analyze. Therefore the root-mean-square (RMS) of temperature was calculated and presented in Fig. 72 and 73. RMS were normalized by the local maximum value of RMS. Fig. 72 depicted the RMS of temperature in the sub-channel region. The profiles for high Pr numbers has a similar shape as the TKE. However, once the correlation between conductivity and

viscosity break down, the profile becomes much different. The maxima of fluctuations increase as Pr decreases. This highlights that at for low Prandtl numbers the high thermal diffusion begins to outweigh the effects of momentum fluctuations.

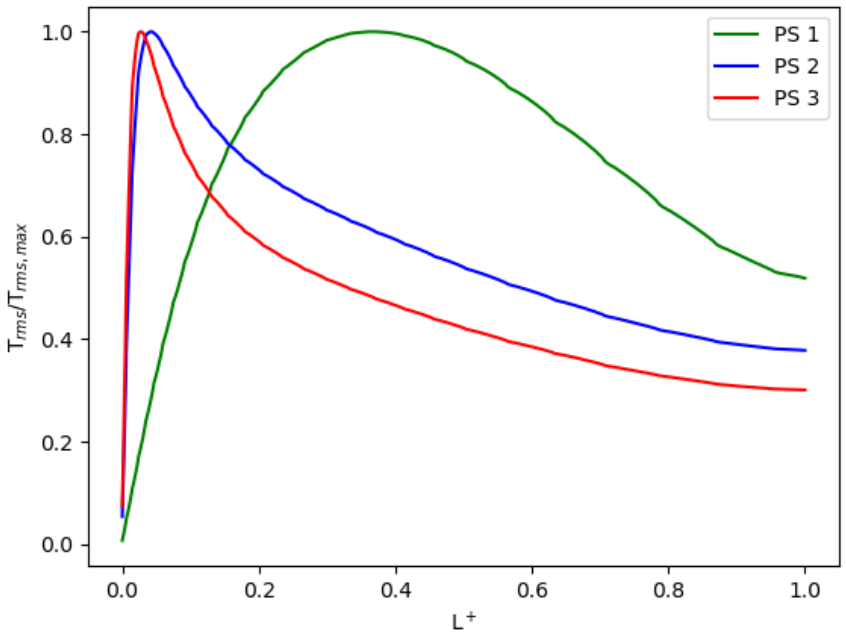

Figure 72: RMS of temperature profile in the sub-channel region.

For RMS temperatures toward the gap center, a different phenomenon occurred. As shown in Fig. 73 with decreasing Pr number the maxima are going toward the center of the line 1. This means that low Prandtl numbers cause most of its temperature pulsations to occur in the gap center. Further investigation into these physics should be done for different Reynolds number to determine if this effect is dependent on the Prandtl number. Still, this behavior is different from locations farther from adjacent rods, because the two heated rods are in high proximity. These findings showed that the shape of the temperature fluctuations change drastically depending on the Pr number and pose a challenge for modeling heat transfer in such geometry.

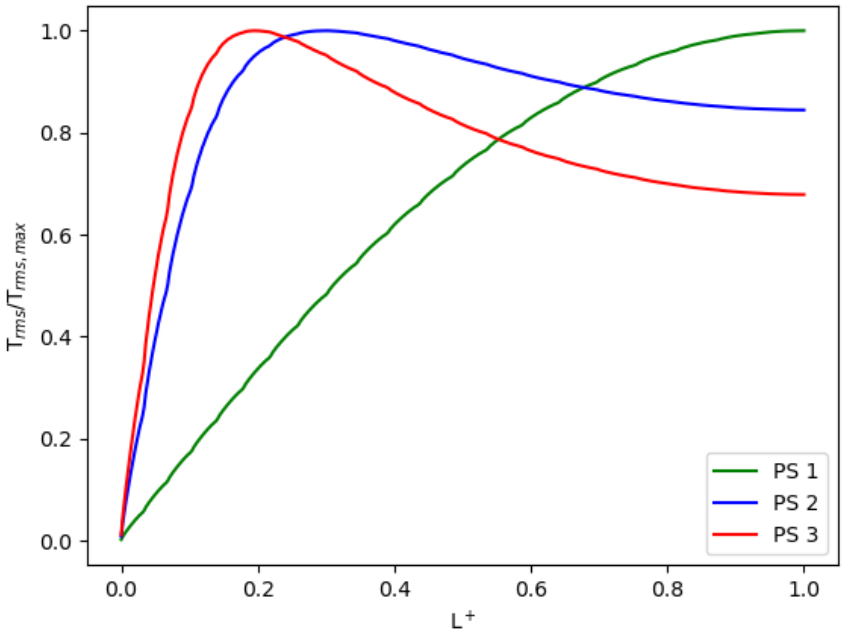

Figure 73: RMS of temperature profile in the gap region.

5.4.11 Collected statistical quantities

Although in this thesis only some of the first and second order statistics were presented and discussed, the generated database consists of much broader spectrum of computed and collected statistical quantities. The list of gathered statistics is given below. The generated DNS results yield in extensive database as a reference for validation purpose, therefore the collected statistical quantities are available on request. Final data generated for DNS, takes about 1.5 TB of disk space (included 3D fields).

List of collected statistical quantities.

- Instantaneous fields
  - $u,\ v,\ w,\ P,\ PS1\ldots6$
- Time-averaged 3D fields
  - Time average:$\langle u\rangle,\ \langle v\rangle,\ \langle w\rangle,\ \langle P\rangle,\ \langle PS1\ldots6\rangle$
  - RMS: $\langle u'\rangle,\ \langle v'\rangle,\ \langle w'\rangle,\ \langle P'\rangle,\ \langle PS1\ldots6'\rangle$

  - Covariance with u-velocity:
    $\langle uu \rangle$, $\langle uv \rangle$, $\langle uw \rangle$, $\langle PP \rangle$, $\langle uPS1 \ldots 6 \rangle$
  - Covariance with v-velocity:
    $\langle uv \rangle$, $\langle vv \rangle$, $\langle vw \rangle$, $\langle PP \rangle$, $\langle vPS1 \ldots 6 \rangle$
  - Covariance with w-velocity:
    $\langle uw \rangle$, $\langle vw \rangle$, $\langle ww \rangle$, $\langle PP \rangle$, $\langle wPS1 \ldots 6 \rangle$
  - Skewness: $\langle u \rangle_{skew}$, $\langle v \rangle_{skew}$, $\langle w \rangle_{skew}$, $\langle P \rangle_{skew}$, $\langle PS1 \ldots 6 \rangle_{skew}$
  - Flatness: $\langle u \rangle_{flat}$, $\langle v \rangle_{flat}$, $\langle w \rangle_{flat}$, $\langle P \rangle_{flat}$, $\langle PS1 \ldots 6 \rangle_{flat}$
  - Gradient x: $\langle u_{dx} \rangle$, $\langle v_{dx} \rangle$, $\langle w_{dx} \rangle$, $\langle P_{dx} \rangle$, $\langle PS1 \ldots 6_{dx} \rangle$
  - Gradient y: $\langle u_{dy} \rangle$, $\langle v_{dy} \rangle$, $\langle w_{dy} \rangle$, $\langle P_{dy} \rangle$, $\langle PS1 \ldots 6_{dy} \rangle$
  - Gradient z: $\langle u_{dz} \rangle$, $\langle v_{dz} \rangle$, $\langle w_{dz} \rangle$, $\langle P_{dz} \rangle$, $\langle PS1 \ldots 6_{dz} \rangle$

- Streamwise-averaged 2D fields of the time-averaged quantities
  - Time average:$\langle u \rangle$, $\langle v \rangle$, $\langle w \rangle$, $\langle P \rangle$, $\langle PS1 \ldots 6 \rangle$
  - RMS: $\langle u' \rangle$, $\langle v' \rangle$, $\langle w' \rangle$, $\langle P' \rangle$, $\langle PS1 \ldots 6' \rangle$
  - Covariance with u-velocity:
    $\langle uu \rangle$, $\langle uv \rangle$, $\langle uw \rangle$, $\langle PP \rangle$, $\langle uPS1 \ldots 6 \rangle$
  - Covariance with v-velocity:
    $\langle uv \rangle$, $\langle vv \rangle$, $\langle vw \rangle$, $\langle PP \rangle$, $\langle vPS1 \ldots 6 \rangle$
  - Covariance with w-velocity:
    $\langle uw \rangle$, $\langle vw \rangle$, $\langle ww \rangle$, $\langle PP \rangle$, $\langle wPS1 \ldots 6 \rangle$
  - Skewness: $\langle u \rangle_{skew}$, $\langle v \rangle_{skew}$, $\langle w \rangle_{skew}$, $\langle P \rangle_{skew}$, $\langle PS1 \ldots 6 \rangle_{skew}$
  - Flatness: $\langle u \rangle_{flat}$, $\langle v \rangle_{flat}$, $\langle w \rangle_{flat}$, $\langle P \rangle_{flat}$, $\langle PS1 \ldots 6 \rangle_{flat}$
  - Gradient x: $\langle u_{dx} \rangle$, $\langle v_{dx} \rangle$, $\langle w_{dx} \rangle$, $\langle P_{dx} \rangle$, $\langle PS1 \ldots 6_{dx} \rangle$
  - Gradient y: $\langle u_{dy} \rangle$, $\langle v_{dy} \rangle$, $\langle w_{dy} \rangle$, $\langle P_{dy} \rangle$, $\langle PS1 \ldots 6_{dy} \rangle$
  - Gradient z: $\langle u_{dz} \rangle$, $\langle v_{dz} \rangle$, $\langle w_{dz} \rangle$, $\langle P_{dz} \rangle$, $\langle PS1 \ldots 6_{dz} \rangle$

- Time-averaged 3D TKE

  - Dissipation: $\langle \varepsilon_{uu} \rangle$, $\langle \varepsilon_{vv} \rangle$, $\langle \varepsilon_{ww} \rangle$
  - Production: $\langle \Pi_{uu} \rangle$, $\langle \Pi_{vv} \rangle$, $\langle \Pi_{ww} \rangle$
  - Pressure diffusion: $\langle D_{uu} \rangle$, $\langle D_{vv} \rangle$, $\langle D_{ww} \rangle$
  - Pressure strain: $\langle P_{uu} \rangle$, $\langle P_{vv} \rangle$, $\langle P_{ww} \rangle$
  - Viscous diffusion: $\langle \nu_{uu} \rangle$, $\langle \nu_{vv} \rangle$, $\langle \nu_{ww} \rangle$
  - Turbulent diffusion: $\langle t_{uu} \rangle$, $\langle t_{vv} \rangle$, $\langle t_{ww} \rangle$
- Stream-wise averaged 2D fields of the time-averaged TKE quantities
  - Dissipation: $\langle \varepsilon_{uu} \rangle$, $\langle \varepsilon_{vv} \rangle$, $\langle \varepsilon_{ww} \rangle$
  - Production: $\langle \Pi_{uu} \rangle$, $\langle \Pi_{vv} \rangle$, $\langle \Pi_{ww} \rangle$
  - Pressure diffusion: $\langle D_{uu} \rangle$, $\langle D_{vv} \rangle$, $\langle D_{ww} \rangle$
  - Pressure strain: $\langle P_{uu} \rangle$, $\langle P_{vv} \rangle$, $\langle P_{ww} \rangle$
  - Viscous diffusion: $\langle \nu_{uu} \rangle$, $\langle \nu_{vv} \rangle$, $\langle \nu_{ww} \rangle$
  - Turbulent diffusion: $\langle t_{uu} \rangle$, $\langle t_{vv} \rangle$, $\langle t_{ww} \rangle$
- Stream-wise averaged 2D fields of the time-averaged THF quantities
  - Dissipation: $\langle \varepsilon_{uT} \rangle$, $\langle \varepsilon_{vT} \rangle$, $\langle \varepsilon_{wT} \rangle$
  - Production: $\langle \Pi_{uT} \rangle$, $\langle \Pi_{vT} \rangle$, $\langle \Pi_{wT} \rangle$
  - Pressure-temperature gradient: $\langle g_{uT} \rangle$, $\langle g_{vT} \rangle$, $\langle g_{wT} \rangle$
  - Turbulent diffusion: $\langle t_{ut} \rangle$, $\langle t_{vT} \rangle$, $\langle t_{wT} \rangle$
  - Viscous diffusion: $\langle \nu_{ut} \rangle$, $\langle \nu_{vT} \rangle$, $\langle \nu_{wT} \rangle$
- Time-averaged 3D THF
  - Dissipation: $\langle \varepsilon_{uT} \rangle$, $\langle \varepsilon_{vT} \rangle$, $\langle \varepsilon_{wT} \rangle$
  - Production: $\langle \Pi_{uT} \rangle$, $\langle \Pi_{vT} \rangle$, $\langle \Pi_{wT} \rangle$
  - Pressure-temperature gradient: $\langle g_{uT} \rangle$, $\langle g_{vT} \rangle$, $\langle g_{wT} \rangle$
  - Turbulent diffusion: $\langle t_{ut} \rangle$, $\langle t_{vT} \rangle$, $\langle t_{wT} \rangle$
  - Viscous diffusion: $\langle \nu_{ut} \rangle$, $\langle \nu_{vT} \rangle$, $\langle \nu_{wT} \rangle$

6 Validation of RANS models

6.1 Introduction to RANS validation

It is an unfortunate fact that no single turbulence model is universally accepted as being superior for all classes of problems. The choice of turbulence model depends on considerations such as the physics of the flow, the established practice for a specific class of problem, the level of accuracy required, the available computational resources, and the amount of time available for the simulation. To make the most appropriate choice of model for certain application, one needs to understand the capabilities and limitations of the various options. Therefore, the validation study presented in this thesis aimed to assess the capabilities of different turbulence models for the prediction of turbulent flow and heat transfer in a tightly spaced bare rod bundle.

6.2 Numerical settings

6.2.1 CFD code

All the simulations for the validation purpose were performed with the use of commercial software ANSYS Fluent version R1 2022 [75, 76].

6.2.2 Flow and boundary condition

For the validation study, the same basics and conditions as defined in Section 4 has been considered. Since the DNS for iso-flux boundary condition was not finished, the validation assessment was done only for the iso-temperature boundary condition.

6.2.3 Initial conditions

6.2.3.1 Steady-state RANS Velocity field was initialized as a uniform field (0, 0, 1) m/s and a uniform temperature of 295 K was imposed in the entire domain.

6.2.3.2 Unsteady RANS Velocity and temperature fields were initialized with converged RANS solution.

6.2.3.3 Turbulence modelling In order to perform validation study, six turbulence models were considered. All the selected turbulence models have been presented in Section 3.5.4. None of the tested turbulence models have been tuned for modelling turbulent flow and heat transfer in a bare rod bundle configuration.

6.2.3.4 Solver settings Steady-state RANS simulations (hereafter RANS) have been performed using a coupled flow solver with SIMPLE algorithm. Second order upwind numerical schemes have been applied. The unsteady RANS simulations (hereafter URANS) have been performed using an implicit unsteady solver with second order numerical schemes. The applied time step (i.e. t = 0.001 s) resulted in a maximum convective Courant number ($C \sim 0.3$). with 30 sub-iterations per time step. The URANS computations were carried out for a total time of t = 32.285 s. This corresponds to $\sim$ 14 flow-through times in the modelled geometry with a bulk velocity of 1 m/s. The first $\sim$ 4 flow-through times (FTT) based results were not considered for the analyses and within this time period the flow was fully developed. Starting from the 5th FTT the data statistics were collected in order to get time-averaged quantities.

6.2.4 Mesh

6.2.4.1 Mesh sensitivity Mesh sensitivity study for RANS simulations was performed in 2 subsequent steps. As a first step, a 2D mesh sensitivity study has been performed in the cross-section normal to the streamwise direction. This study has been performed in a short streamwise computational domain with a length of 228.5 mm, which has been divided in 40 cells in the streamwise direction. Detailed mesh parameters are given in

Table 9. Extruded hexahedral meshes were applied with different hexahedral (i.e. base element size) as well as different arrangement of inflation layers (number of layers - N). Thus, a 2D mesh is first generated in a cross-section normal to the main flow direction. The total number of cells in these meshes is given as 2D cell count in Table 9. For all of the meshes, the first layer height is kept the same, whereas different values for growth rate (GR) in the inflation layers have been applied. The first cell size was set to $a_0 = 0.05mm$, which corresponds to $y^+ \sim 0.3$ and it is kept the same for all the meshes. Introducing Δz as a streamwise spatial discretization length, the maximal aspect ratio is $\Delta z/a_0 = 228.5mm/(40 * 0.05) \approx 114$ for every mesh listed in Table 9. Cross-sections of the applied meshes are shown in Fig. 74 with gap region zoomed area.

Table 9: 2D mesh sensitivity study.

Mesh	**2D cell el.**	Δz	**Base size [mm]**	**N**	**GR**	u_τ **[m/s]**	**Discr. [%]**
M1	6535	40	2.50	12	1.35	0.0591	0.96
M2	9295	40	2.00	13	1.30	0.0592	0.72
M3	14459	40	1.50	14	1.25	0.0594	0.49
M4	20199	40	1.25	16	1.20	0.0595	0.23
M5	29797	40	1.00	18	1.17	0.0596	0.09
M6	47688	40	0.75	20	1.15	0.0597	0

The mesh sensitivity study has been performed with the SST $k - \omega$ turbulence model. Results of streamwise velocity component w, turbulent kinetic energy k and $\langle v^{'} w^{'} \rangle$ Reynolds stress component along L1 and L3 were shown in Fig. 75

Although the mesh M1 is much coarser than the finest mesh M6 (see Fig. 74), this did not affect the prediction of streamwise velocity profile. In fact, similar velocity profiles are predicted on all considered meshes and along both lines. Only small discrepancies could be observed close to the center of L1, so in the centre of gap region [see Fig. 75 *a*)]. Additionally, the

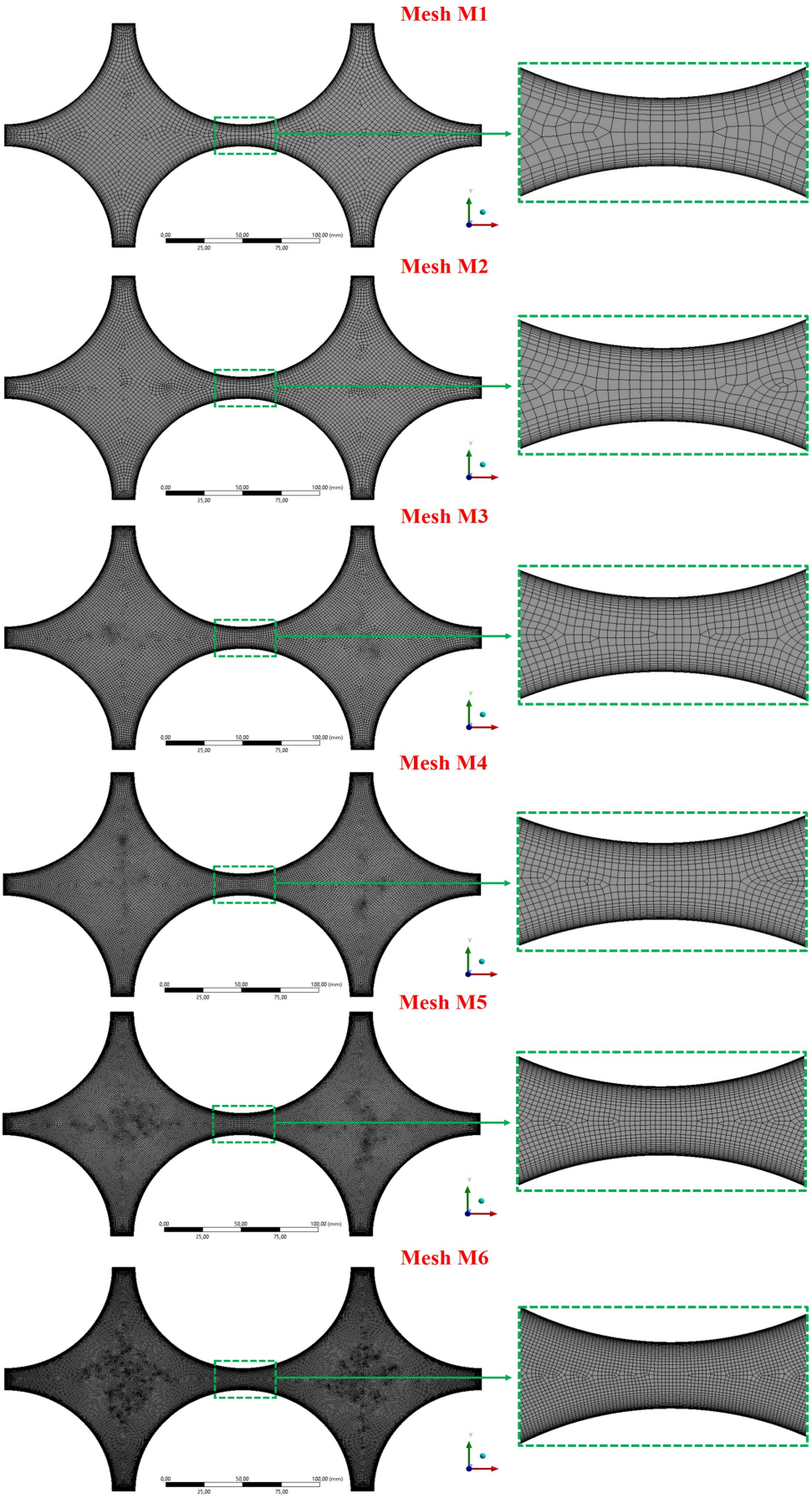

Figure 74: 2D cross-section meshes.

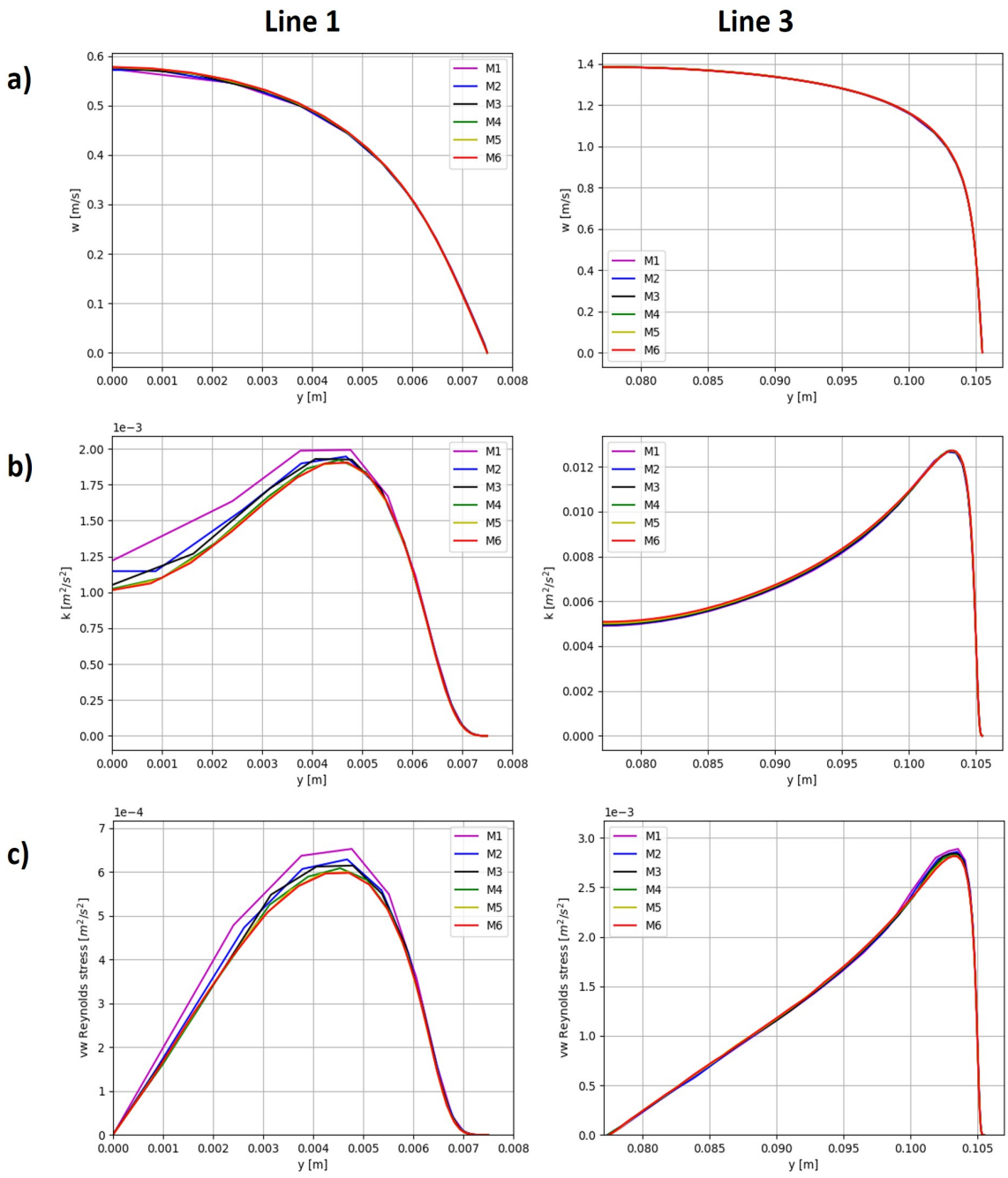

Figure 75: Results of mesh sensitivity study along two lines: streamwise velocity - *a*), turbulent kinetic energy - *b*), and $\langle v'w' \rangle$ Reynolds stress - *c*).

similar profiles compatibility was observed for TKE and $\langle v^{'} w^{'} \rangle$ Reynolds stress considering the sub-channel region (L3). However, visible differences were noticed in the results for the TKE and $\langle v^{'} w^{'} \rangle$ Reynolds stress in the gap region (L1) as depicted in Fig. 75 *b*) and *c*). Namely, results from the mesh M1 significantly over-predicted TKE and $\langle v^{'} w^{'} \rangle$ Reynolds stress with respect to the results from the finest mesh M6. Results from M2 and M3 meshes as well slightly over-predicted, while from other meshes M4-M6 were found to be in a very good mutual agreement everywhere. Especially results form M5 and M6 matched perfectly. As a second step, mesh discretization has been varied in the streamwise direction only. In this study, the complete rod bundle length (i.e. 2.285 m) has been simulated, which is 100-times longer than the streamwise domain in the previous 2D mesh sensitivity study. Mesh M5 from the previous 2D mesh sensitivity study was used as a baseline 2D cross-sectional discretization. This mesh proved to be fine enough since the profiles in Fig. 75 are converged as well as the calculated mean friction velocity u_{τ} (presented in Table 9) is less within 0.1% of the result obtained on the finest mesh M6. Hence, mesh M5 is extended to a 100-times longer domain using three different streamwise discretizations, denoted as meshes M5_A, M5_B and M5_C, and presented in Table 10. In spite of a much larger maximum aspect ratio (max AR) of the cells, the applied streamwise discretization does not affect the predictions of the wall shear stresses noticeably. Hence, it was estimated that the spatial discretization of mesh M5_B is sufficiently fine for steady-state RANS simulations. Therefore, this mesh was used for all the other simulations performed in the validation study.

6.3 Results - validation study

URANS, time-averaged results of the of the validation study are presented in this section. A quantitative analysis was performed on the flow behaviour along L1 and L3, which correspond to the gap and sub-channel

Table 10: 3D mesh sensitivity study.

Mesh	**Mesh size** [10^6]	$\mathbf{N_z}$	**Max AR**	u_τ **[m/s]**	**Discr. [%]**
M5	1.9	40	11.4	0.0596	/
M5_A	11.9	400	114	0.0596	0
M5_B	5.95	200	229	0.0596	0
M5_C	2.97	100	457	0.0596	0

region, respectively. Results obtained with different turbulence models were compared with the reference DNS database as well as among each other.

6.3.1 Wall shear stress

The proper prediction of the wall shear stress (WSS) distribution is the most crucial result for the correct prediction of a pressure drop. In bare rod bundles, wall shear stress is a non-uniform function of location with the smallest value in the gap region, and the largest value at the widest region of the sub-channel, which corresponds to the largest fluid velocity in the bulk region. Fig. 76 depicted different predictions of wall shear stress distribution along the perimeter of the bottom rod.

Clearly, all applied turbulence models usually over-predicted the wall shear stress with respect to the prediction of the DNS results. The RKE model as well as SST $k-\omega$ performed better than the other isotropic and non-isotropic models in the gap region, which corresponds to $\theta = 90°$. On the other hand, considering the sub-channel regions ($\theta = 45°$ and $\theta = 135°$) these models significantly over-predicted wall shear stress. The best fit for these locations was found with the WJ-BSL-EARSM model. Surprisingly, the most sophisticated model - RSM, which was tested in the validation study, did not give the best results. Those observations highlighted that for this specific application, namely flow in the tightly spaced rod bundle, there is no universal turbulent model, which could properly predict the flow behaviour in the whole domain. In general, the analysis has shown

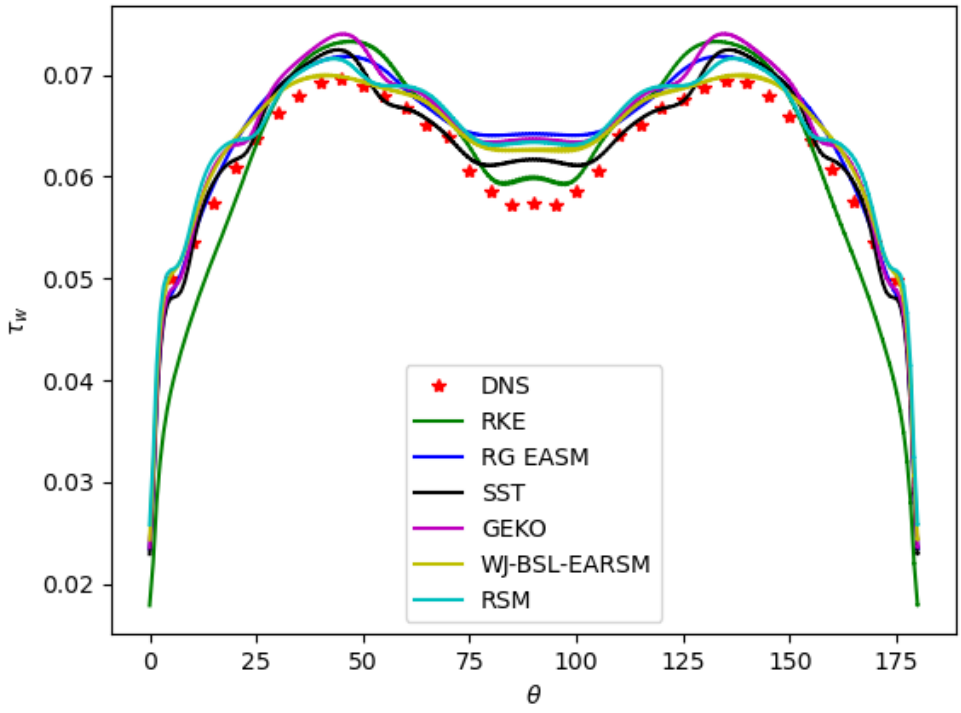

Figure 76: Wall shear stress distribution along the rod surfaces.

that the prediction of the wall shear stress is still the main issue for correct reproduction of a turbulent flow in a bare rod bundle. The reason for that might be related to the fact that none of the applied turbulence models have been tuned for this flow configuration. For a comparison, magnitudes of the mean shear stress have been reported also in [54]. In this study several linear and non-linear eddy viscosity models have been verified and discrepancies in the mean wall shear stress predictions ranged from 3% to 14% for the $k-\epsilon$ linear and SST $k-\omega$ model, respectively.

6.3.2 Averaged velocity

Fig. 77 presents the comparison of normalized streamwise velocity. In the gap region all models under-predict the velocity. The best fit is obtained for the RKE model, which is related to the best mapping of WSS by this model in gap region. In the sub-channel region, all the models over-predict the

values of streamwise velocity. Actually, RANS models are almost consistent with each other.

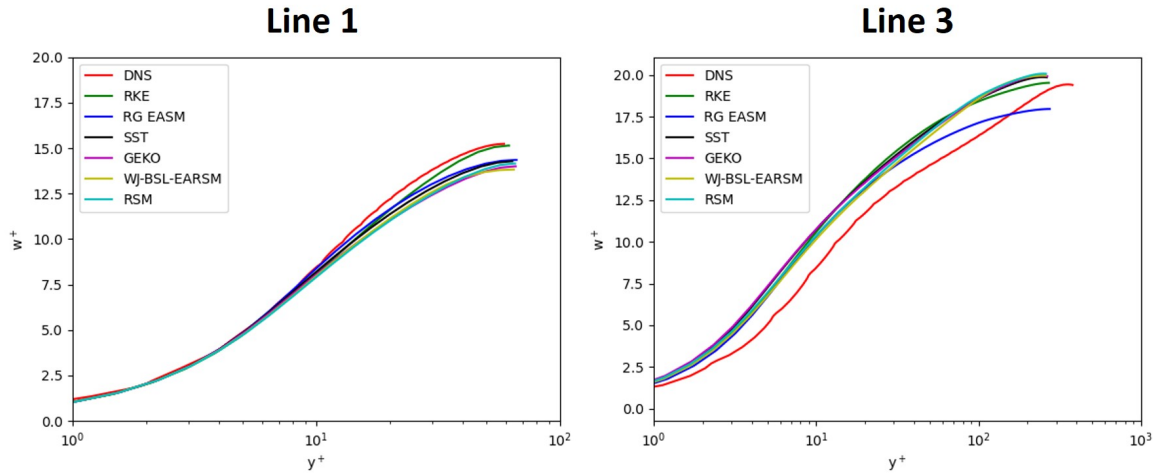

Figure 77: Comparison of the predicted streamwise velocity versus DNS results.

6.3.3 Turbulent kinetic energy

In Fig. 78 the comparison between the reference DNS result and various turbulence models is presented. It turns out that in the gap region, RG EASM, RKE, and RSM are in quite good agreement with DNS results. Comparing the general shape of the profiles, the shape of the RSM most closely resembles the reference result. However, the peak in the close-wall region ($L^+ = 0.1 \sim 0.3$) is clearly under-predicted. Considering the peak magnitude, the best fit is found with RG EASM, but, this model for $L^+ > 0.2$ starts to deviate and is characterized by the steeper slope. Quite good fit is found for REK model, but in this case the peak location is moved toward the gap center. Comparing the results in the sub-channel region, all the models under-predict the peak of TKE in the near-wall region, while in the center of the line, this trend reverse and all the models under-predict the TKE.

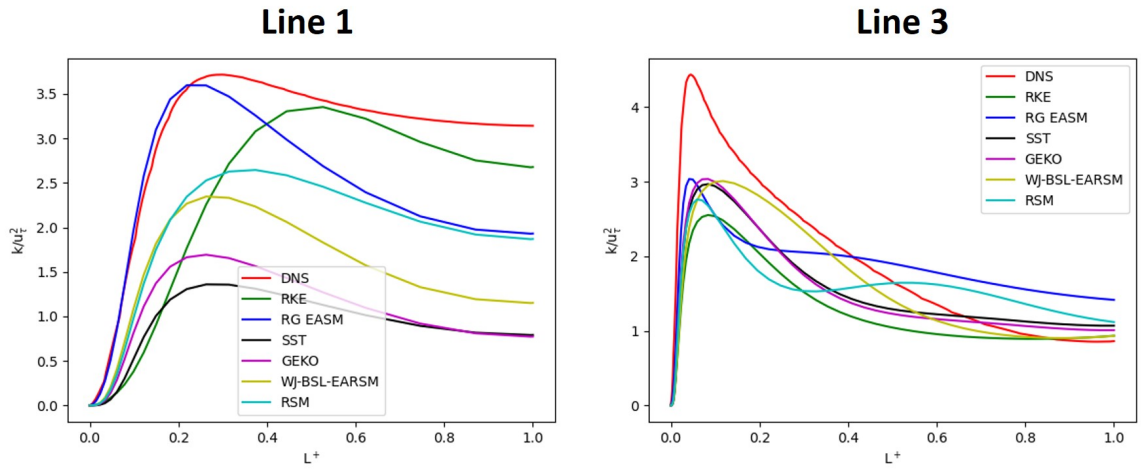

Figure 78: Comparison of the predicted turbulent kinetic energy versus DNS results.

6.3.4 Momentum frequency

In the validation study, the capability of the reproduction of the gap vortex street in the tightly spaced rod bundle configuration is verified. As illustrated in Fig. 79 all models are able to recreate the gap vortex street. Fig. 79 depicts the contours of streamwise velocity. Although the velocity magnitudes are different, they are still comparable with scaling.

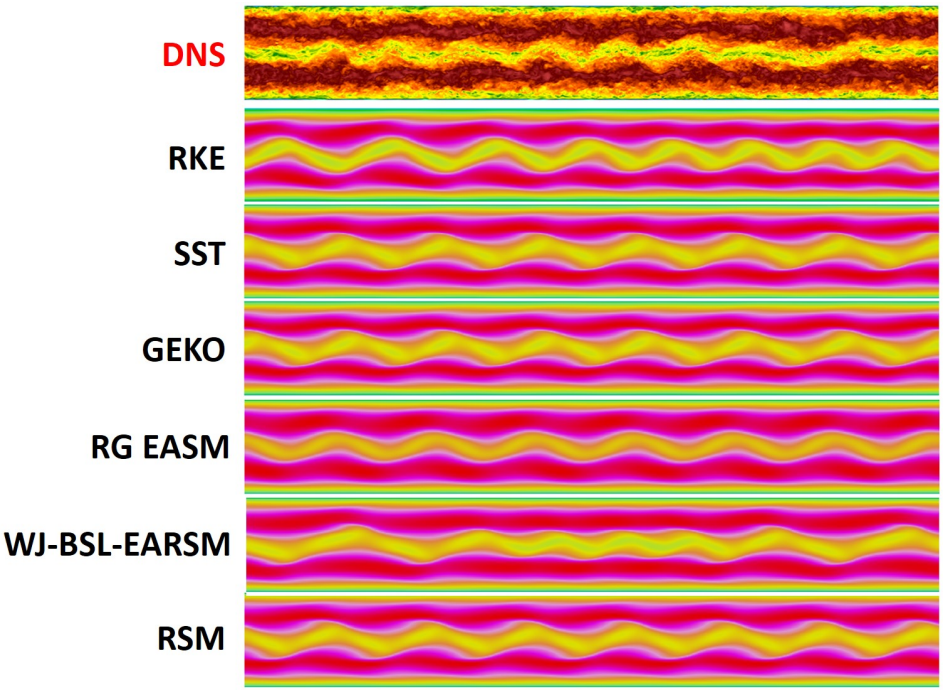

Figure 79: Velocity contours - comparison between DNS and RANS models.

It is easily to notice that DNS contour is very complex with a lot of small and big swirls. The RANS models are able to only reproduce the macroscopic flow behavior. As it was mentioned in Section 5.4.4, the dominant frequency of flow pulsations occurred at 3.7 Hz. For RANS models, the characteristic frequency is computed as well. For all the RANS models the characteristic frequency is similar $\sim 3.1 - 3.2Hz$, which is slightly smaller value than for DNS. Additionally, for RKE and WJ-BSL-EARSM, apart form the dominant frequency, a set of characteristic peaks is observed. In these models, gap vortex street is composed of smaller and bigger waves (see Fig. 79).

6.3.5 Thermal field

In the last step of the validation study, the RANS models are assessed to model the turbulent heat flux. Usually, the heat transfer has been modelled assuming a simple Gradient Diffusion Hypothesis (SGDH), which has used a linear relationship between turbulent heat flux $\langle t^{'} u_i^{'} \rangle$ and the temperature gradient:

$$\langle t^{'} u_i^{'} \rangle = -\alpha_t \frac{\partial T}{\partial x_i}, \tag{6.1}$$

where turbulent thermal diffusivity is applied as $\alpha_t = \nu_t / Pr_t$ using turbulent momentum diffusivity ν_t calculated from the turbulence model and the turbulent Prandtl number $Pr_t = 0.9$. The SGDH approach is based on the Reynolds analogy. This approach is overly simplistic and is available in all RANS based CFD codes. Although this approach is widely used, then, it is not the best choice for predicting the heat transfer, especially in liquid metal flows, as illustrated in Fig. 80 *a*). Considering the liquid metal flow in the gap region, all the RANS models highly deviate. The presented figure indicates that for RANS models the temperature field in the gap region has almost the same value as the temperature imposed as a BC on the rod walls. Similar, but not so significant trend is observed in

the sub-channel region, where the temperature field is not uniform as in the gap region, which means that all the RANS models highly under-predict the temperatures.

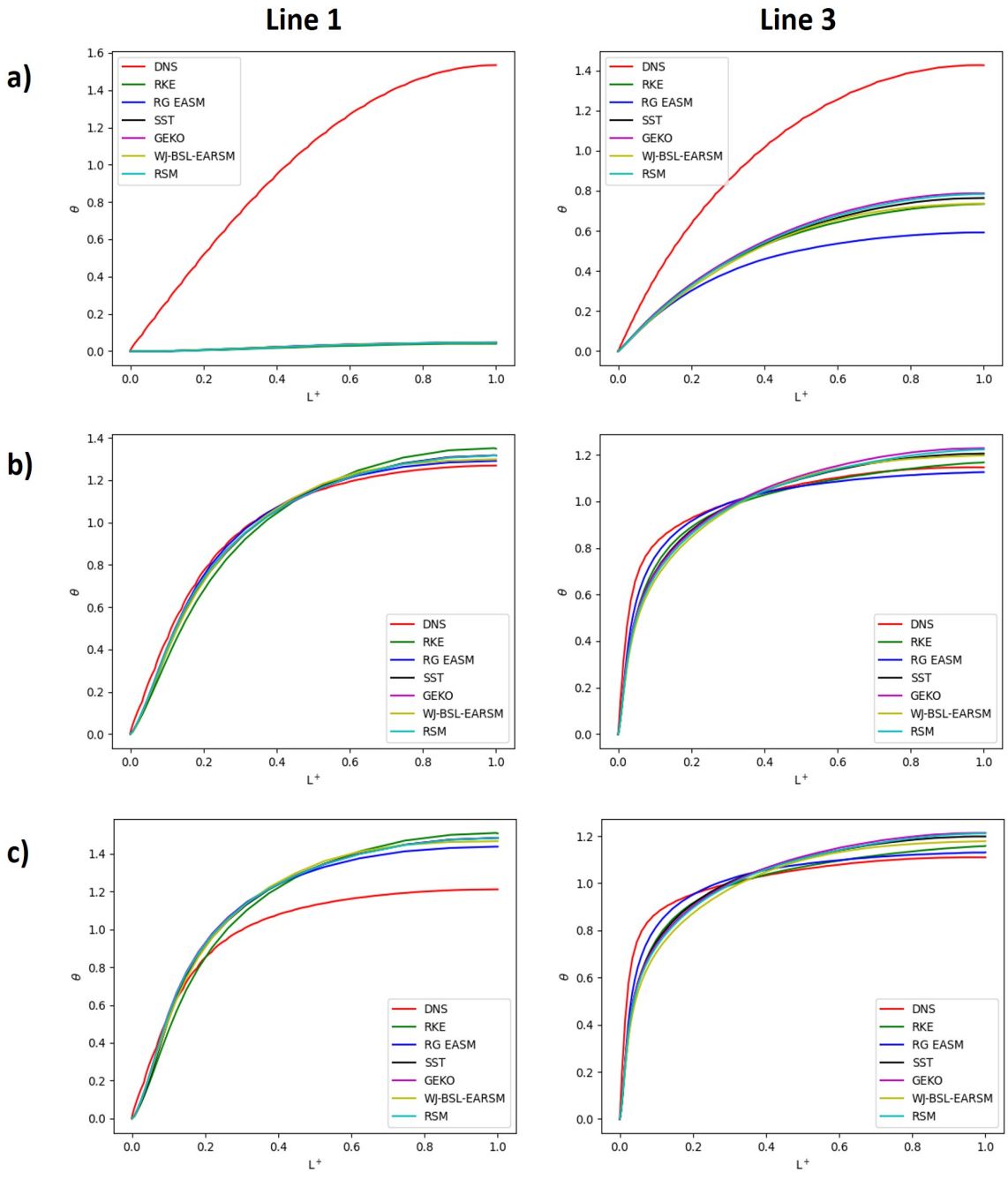

Figure 80: Comparison of the thermal field in the gap and sub-channel region: (a) liquid metal - Pr = 0.025, (b) air - Pr = 1, (c) water - Pr = 2.

For case with Pr = 1 presented in the Fig 80 *b*), temperature profiles were fund in quite good agreement with the reference data. In this case

the thermal and momentum BC are practically equal and in fact RANS models in general are tuned for such BC. For the last passive scalar, namely Pr = 2, RANS models "loose" the prediction capabilities considering the thermal fields. It is especially visible in the gap region. However, on the contrary to the case with Pr $\ll$ 1, here the RANS models over-predict the temperature fields.

These observations clearly prove that apart from the gas-cooled reactor, the usage of RANS approaches can lead to the misleading results. Therefore, one should always be careful in applying the Reynolds analogy to non-unity Pr fluids, particularly to low-Pr fluids and must realize its limitations with respect to accuracy. It is worth reminding, that all the tested turbulent RANS models were run with default options. In this study, it was found which models have given the most promising results. In the future, those models will be thoroughly tested by changing the default values as well as the sensitivity and uncertainties study of turbulent constant models will be performed. This would allow tunning the pragmatic turbulent model and proposing the best practice guidance for the numerical prediction of the turbulent flow and heat transfer in tightly spaced rod bundles.

7 Summary and conclusions

This thesis presents a comprehensive approach toward the accurate prediction of the turbulent flow and heat transfer in a tightly spaced rod bundles. As a reference, the Hooper's hydraulic experiment [25] geometry has been adopted. The diameter (D) of the rod was 14 cm and the pitch (P) between the two rods was 15.5 cm, so the pitch-to-diameter ratio P/D = 1.107, which makes itself a tightly spaced rod bundle. The streamwise length of the test section was 9.14 m, which is equivalent to 128 hydraulic diameters. Air at room temperature was used as a working fluid for the Hooper case. However, performing a DNS of the Hooper case requires a huge amount of computational power. An initial mesh estimation of this case was performed (based on the obtained URANS results) and it would require a total of 14 billion grid points only for the flow field to perform a true DNS. Furthermore, additional constraints with respect to the simulation time-step etc. would make this DNS not feasible for available computer resources. Hence, a calibration of the Hooper case was performed to optimize the flow configuration in such a way that it preserves the essence of the Hooper experiment, i.e. the gap vortex street.

As a first step, the numerical experiment have been designed. A wide range of unsteady RANS study has been performed to calibrate and optimize the Hooper case for the targeted DNS study. The calibration was related to the scaling of the Reynolds number, which was scaled down in such a way that the overall phenomenology of the flow field remained the same, and the axial flow pulsations existed. Afterwards, the calibration of the computational domain with the respective boundary conditions has been performed to obtain an optimized Hooper case, which was feasible for the available computational resources. In addition to the flow field, a parametric study for different passive scalars has been performed in order to take into account the heat transfer analysis, which was not included in the

original Hooper case.

Secondly, based on the set up configuration defined in the calibration study, the proper DNS simulation has been performed. In the simulations three different passive scalars, which corresponded to the Prandtl numbers of three working fluids, i.e. air, water, and liquid metal have been investigated. The heat transfer of these three fluids has been studied in combination with two different boundary conditions at the walls, i.e. a constant temperature and a constant heat flux. The final DNS has been yielded in an extensive validation database for flow and the thermal fields representing different reactor coolants. Although the results with constant heat flux BC did not reach the statistical convergence, the obtained results already gave an extensive reference database. This database with results of first and second, then third, and fourth order statistics is available upon a request to the author or author's institution. The available variables have been listed in Section 5.4.11.

Further, different RANS models have been thoroughly investigated in order to assess their prediction capabilities and limitations. It has been found that due to a complex geometry of the rod bundle, the flow was characterized by non-uniform profiles. Validation study highlighted that there has been no single turbulence model, which would universally accurately predict turbulent flow and heat transfer in tightly spaced rod bundles. The geometry is characterized by two regions: the gap and the sub-channel. In the gap region - the narrowest area between two adjacent rods - the lowest values of velocity and the highest values of temperature have been recorded. The opposite situation has been observed in the sub-channel region: the highest values of velocity and lowest temperatures. This has indicated that in order to get reliable RANS results, probably two different models have to be used. In the validation study, some of the most promising models have been defined. In the future study those models will further be investigated in order to check the influence of model turbulent

constants.

Finally, the comprehensive CFD methodology toward an accurate prediction of turbulent flow and heat transfer phenomena at sub-channel level with the set of the best practice guidelines has been developed and defined.

References

[1] A. Shams and T. Kwiatkowski. Towards the direct numerical simulation of a closely-spaced bare rod bundle. *Annals of Nuclear Energy*, 121:146 – 161, 2018.

[2] A. Shams, D. De Santis, A. Padee, P. Wasiuk, T. Jarosiewicz, T. Kwiatkowski, and S. Potempski. High-Performance Computing for Nuclear Reactor Design and Safety Applications. *Nuclear Technology*, 206(2):283–295, 2020.

[3] T. Cardoso De Souza, A. Shams, F. Roelofs, and T. Kwiatkowski. Calibration Of High fidelity bare rod bundle simulations for various PRANDTL fluids. In *International Topical Meeting on Nuclear Reactor Thermal Hydraulics 2015, (NURETH16)*, volume 4, pages 2774–2787, 2015.

[4] A. Shams and T. Kwiatkowski. Design of a closely-spaced rod bundle for a reference direct numerical simulation. volume Volume 8: Computational Fluid Dynamics (CFD); Nuclear Education and Public Acceptance of *International Conference on Nuclear Engineering, ICONE26*, 07 2018. V008T09A002.

[5] A. Shams, D. De Santis, A. Padee, P. Wasiuk, T. Jarosiewicz, T. Kwiatkowski, and S. Potempski. High- Performance Computing for Nuclear Reactor Design and Safety Applications. Advances in Thermal Hydraulics (ATH 2018), ANS Winter Meeting Embedded Topical, 2018.

[6] A. Padee, T. Kwiatkowski, P. Wasiuk, T. Jarosiewicz, S. Potempski, and A. Shams. Assesment of high performance computing for nuclear reactor thermal-hydraulics applications. 18th International Topical Meeting on Nuclear Reactor Thermal Hydraulics, NURETH-18, 2019.

[7] T. Kwiatkowski and A. Shams. Towards the accurate prediction of flow and heat transfer in a tightly spaced bare rod bundle configuration. The International Congress on Advances in Nuclear Power Plants - ICAPP2021, 2021.

[8] T. Kwiatkowski and A. Shams. The formation of the gap vortex street in square arranged rod bundles. The International Congress on Advances in Nuclear Power Plants - ICAPP2021, 2021.

[9] T. Kwiatkowski, M. Spirzewski, and A. Shams. Validation of rans based cfd modelling approach for flow in a tightly spaced bare rod bundle with heat transfer in various prandtl fluids. 13th International Topical Meeting on Nuclear Reactor Thermal-Hydraulics, Operation and Safety (NUTHOS-13 2022), 2022. under-review.

[10] D. De Santis, A. De Santis, A. Shams, and T. Kwiatkowski. The influence of low prandtl numbers on the turbulent mixed convection in an horizontal channel flow: Dns and assessment of rans turbulence models. *International Journal of Heat and Mass Transfer*, 127:345–358, 2018.

[11] A. Shams, D. De Santis, D. Rosa, T. Kwiatkowski, and E.J.M. Komen. Direct numerical simulation of flow and heat transfer in a simplified pressurized thermal shock scenario. *International Journal of Heat and Mass Transfer*, 135:517–540, 2019.

[12] P. Szymczak, K. Kwiatkowski, M. Jarosinskí, T. Kwiatkowski, and F. Osselin. Wormhole Formation During Acidizing of Calcite-Cemented Fractures in Gas-Bearing Shales. *SPE Journal*, 24(02):795–810, 02 2019.

[13] S. Tavoularis. Reprint of: Rod bundle vortex networks, gap vortex streets, and gap instability: A nomenclature and some com-

ments on available methodologies. *Nuclear Engineering and Design*, 241(11):4612–4614, 2011.

[14] A. Shams, F. Roelofs, I. Tiselj, J. Oder, Y. Bartosiewicz, M. Duponcheel, B. Niceno, W. Guo, E. Stalio, D. Angeli, A. Fregni, S. Buckingham, L.K. Koloszar, A. Villa Ortiz, P. Planquart, C. Narayanan, D. Lakehal, K. van Tichelen, W. Jäger, and T. Schaub. A collaborative effort towards the accurate prediction of turbulent flow and heat transfer in low-prandtl number fluids. *Nuclear Engineering and Design*, 366:110750, 2020.

[15] A. Shams. Turbulent heat transport. In F. Roelofs, editor, *Thermal Hydraulics Aspects of Liquid Metal Cooled Nuclear Reactors*, page 273–292. Woodhead Publishing, 2019.

[16] G. Groetzbach. Anisotropy and buoyancy in nuclear turbulent heat transfer - critical assessment and needs for modelling. Technical report, Forschungszentrum Karlsruhe, FZKA 7363, 2007.

[17] Z. Hu, J. Liu, L. Gan, and S. Xu. Wake modes behind a streamwisely oscillating cylinder at constant and ramping frequencies. *Journal of Visualization*, 22:505–527, 2019.

[18] L. Chandra, F. Roelofs, E. M. J. Komen, and E. Baglietto. Unsteady RANS and LES Analyses of Hooper ' s Hydraulics Experiment in a Tight Lattice Bare Rod-bundle. In *The 8th International Topical Meeting on Nuclear Thermal-Hydraulics, Operation and Safety (NUTHOS-8)*, pages 1–13, Shanghai, 2010.

[19] B.H. Yan. The thermal hydraulic phenomenon in tight lattice bundles: A review. *Annals of Nuclear Energy*, 126:330–349, 2019.

[20] J.T. Rogers and N.E. Todreas. Coolant interchannel mixing in reactor fuel rod bundles single-phase coolants. In *ASME Annual Winter Meeting*, pages 1–2, New York, 1968.

[21] D. S. Rowe. Measurement Of Turbulent Velocity, Intensity And Scale In Rod Bundle Flow Channels, BNWL - 1736. Technical report, Battelle Pacific Northwest Laboratories, Richland, Washington, 1973.

[22] A.C. Trupp and R.S. Azad. The structure of turbulent flow in triangular array rod bundles. *Nuclear Engineering and Design*, 32:47–84, 1975.

[23] J.D. Hooper. Developed single phase turbulent flow through a square-pitch rod cluster. *Nuclear Engineering and Design*, 60(3):365–379, 1980.

[24] J.D. Hooper and K. Rehme. The structure of single-phase turbulent flows through closely spaced rod arrays. Technical report, Kernforschungszentrum Karlsruhe GmbH, Karlsruhe, 1983.

[25] J.D. Hooper and K. Rehme. Large-scale structural effects in developed turbulent flow through closely-spaced rod arrays. *Journal of Fluid Mechanics*, 145:305–337, 1984.

[26] J.D. Hooper and D.H. Wood. Fully developed rod bundle flow over a large range of Reynolds number. *Nuclear Engineering and Design*, 83(1):31–46, 1984.

[27] S. V. Möller. On phenomena of turbulent flow through rod bundles. *Experimental Thermal and Fluid Science*, 4(1):25–35, 1991.

[28] K. L. Lee and B. J. Lee. Study on the relationship between turbulent normal stresses in the fully developed bare rod bundle flow. *Journal of the Korean Nuclear Society*, 27(6):888–893, 1995.

[29] M. S. Guellouz and S. Tavoularis. The structure of turbulent flow in a rectangular channel containing a cylindrical rod–Part 1: Reynolds-averaged measurements. *Experimental Thermal and Fluid Science*, 23:59–73, 2000.

[30] M. S. Guellouz and S. Tavoularis. The structure of turbulent flow in a rectangular channel containing a cylindrical rod – Part 2: phase-averaged measurements. *Experimental Thermal and Fluid Science*, 23:75–91, 2000.

[31] A. S. Lexmond, R. F. Mudde, and T. H. J. J. van der Hagen. Visualisation of the Vortex Street and Characterisation of the Cross Flow in the Gap Between Two Sub-Channels. In *11th International Topical Meeting on Nuclear Reactor Thermal-Hydraulics (NURETH-11)*, pages 1–20, Avignon, 2005.

[32] A. Gosset and S. Tavoularis. Laminar flow instability in a rectangular channel with a cylindrical core. *Physics of Fluids*, 18(4), 2006.

[33] A. Mahmood, M. Rohde, T.H.J.J. van der Hagen, and R. F. Mudde. Contribution of large-scale coherent structures towards the cross flow in two interconnected channels. In *The 13th International Topical Meeting on Nuclear Reactor Thermal Hydraulics (NURETH-13)*, pages 1–12, Kanazawa, 2009.

[34] F. Baratto, S. C.C. Bailey, and S. Tavoularis. Measurements of frequencies and spatial correlations of coherent structures in rod bundle flows. *Nuclear Engineering and Design*, 236(17):1830–1837, 2006.

[35] Ch. Y. Lee, Ch. H. Shin, and W. K. In. Effect of gap width on turbulent mixing of parallel flow in a square channel with a cylindrical rod. *Experimental Thermal and Fluid Science*, 47:98–107, 2013.

[36] A. K. M. F. Hussain. Coherent structures - reality and myth. *Physics of Fluids*, 26(10):2816–2850, 1983.

[37] D. Chang and S. Tavoularis. Simulations of turbulence, heat transfer and mixing across narrow gaps between rod-bundle subchannels. *Nuclear Engineering and Design*, 238(1):109–123, 2008.

[38] L. Meyer. Measurements of Turbulent Velocity and Temperature in a Central Channel of a Heated Rod Bundle. Technical Report January 1991, Karlsruhe Institute of Technology, 1991.

[39] L. Meyer. Measurement of turbulent velocity and temperature in axial flow through a heated rod bundle. *Nuclear Engineering and Design*, 146(93):71–82, 1994.

[40] T. Krauss and L. Meyer. Characteristics of turbulent velocity and temperature in a wall channel of a heated rod bundle. *Experimental Thermal and Fluid Science*, 12(1):75–86, 1996.

[41] T. Krauss and Leonhard Meyer. Experimental investigation of turbulent transport of momentum and energy in a heated rod bundle. *Nuclear Engineering and Design*, 180(3):185–206, 1998.

[42] G. Mayer and G. Házi. Direct numerical and large eddy simulation of longitudinal flow along triangular array of rods using the lattice boltzmann method. *Mathematics and Computers in Simulation*, 72(2):173–178, 2006. Discrete Simulation of Fluid Dynamics in Complex Systems.

[43] H. Ninokata, E. Merzari, and A. Khakim. Analysis of low reynolds number turbulent flow phenomena in nuclear fuel pin subassemblies of tight lattice configuration. *Nuclear Engineering and Design*, 239(5):855–866, 2009. Special Edition in honor of the retirement of Professor Neil Todreas.

[44] H. Wang, J. Zang, J. Wang, and Y. Huang. Large eddy simulation of the heat transfer and unsteady pulsation of supercritical carbon dioxide in a square subchannel. *International Journal of Thermal Sciences*, 172:107377, 2022.

[45] Y. Duan and S. He. Heat transfer of a buoyancy-aided turbulent flow in a trapezoidal annulus, nov 2017.

[46] Y. Duan and S. He. Large eddy simulation of a buoyancy-aided flow in a non-uniform channel – Buoyancy effects on large flow structures. *Nuclear Engineering and Design*, 312:191–204, feb 2017.

[47] T. Ikeno and T. Kajishima. Analysis of dynamical flow structure in a square arrayed rod bundle. *Nuclear Engineering and Design*, 240(2):305–312, 2010. Twelfth International Topical Meeting on Nuclear Reactor Thermal Hydraulics (NURETH-12).

[48] G. Mayer, J. Páles, and G. Házi. Large eddy simulation of subchannels using the lattice boltzmann method. *Annals of Nuclear Energy*, 34(1):140–149, 2007.

[49] E. Merzari and H. Ninokata. Proper orthogonal decomposition of the flow in a tight lattice rod-bundle. *Nuclear Engineering and Design*, 241(11):4621–4632, 2011. 13th International Topical Meeting on Nuclear Reactor Thermal Hydraulics (NURETH-13).

[50] B. Mikuž and I. Tiselj. Wall-resolved large eddy simulation in grid-free 5×5 rod bundle of matis-h experiment. *Nuclear Engineering and Design*, 298:64–77, 2016.

[51] H. Ninokata and E. Merzari. Computational fluid dynamics and simulation-based-design approach for tight lattice nuclear fuel pin subassemblies. In *12th International Topical Meeting on Nuclear Reactor Thermal Hydraulics, NURETH-12*, pages 1–20, 2007.

[52] A. Shams, B. Mikuž, and F. Roelofs. Numerical prediction of flow and heat transfer in a loosely spaced bare rod bundle. *International Journal of Heat and Fluid Flow*, 73(February):42–62, 2018.

[53] J. Walker, E. Merzari, A. Obabko, P. Fischer, and A. Siegel. Accurate prediction of the wall shear stress in rod bundles with the spectral element method at high reynolds numbers. *International Journal of Heat and Fluid Flow*, 50:287–299, 2014.

[54] E. Baglietto and H. Ninokata. A turbulence model study for simulating flow inside tight lattice rod bundles. *Nuclear Engineering and Design*, 235(7):773–784, 2005.

[55] D. Chang and S. Tavoularis. Numerical simulation of turbulent flow in a 37-rod bundle. *Nuclear Engineering and Design*, 237(6):575–590, 2007.

[56] M. Liu and Y. Ishiwatari. Unsteady numerical simulations of single-phase turbulent mixing in tight lattice geometries. *Nuclear Engineering and Design*, 256:28–37, 2013.

[57] B.H. Yan. Periodic large scale vortex structure in rectangular channels with non-uniform wall roughness. *Nuclear Engineering and Design*, 241(8):2948–2955, 2011.

[58] B.H. Yan and H.Y. Gu. The flow and heat transfer of turbulent pulsating flow in rod bundles in rolling motion. *Progress in Nuclear Energy*, 54(1):49–55, 2012.

[59] L. Meyer. From discovery to recognition of periodic large scale vortices in rod bundles as source of natural mixing between subchannels—a review. *Nuclear Engineering and Design*, 240(6):1575–1588, 2010.

[60] A. Moorthi, A. Kumar Sharma, and K. Velusamy. A review of subchannel thermal hydraulic codes for nuclear reactor core and future directions. *Nuclear Engineering and Design*, 332:329–344, 2018.

[61] S. B. Pope. *Turbulent Flows*. Cambridge University Press, 2000.

[62] H. Tennekes and J. L. Lumley. *A First Course in Turbulence*. The MIT Press, 1972.

[63] L. F. Richardson. Weather prediction by numerical process, cambridge (university press), 4°. pp. xii + 236. 30s.net. *Quarterly Journal of the Royal Meteorological Society*, 48(203):282–284, 1922.

[64] A. Kolmogorov. The local structure of turbulence in incompressible viscous fluid for very large Reynolds' numbers - in Russian. *Doklady Akademiia Nauk SSSR*, 30:301–305, 1941.

[65] C.E. Shannon. Communication in the presence of noise. *Proceedings of the IRE*, 37(1):10–21, jan 1949.

[66] H. K. Versteeg and W. Malalasekera. *An introduction to computational fluid dynamics. The finite volume method,*. Pearson Education Limited, 2007.

[67] T. Von Kármán. *Mechanische Ähnlichkeit und Turbulenz*. Sonderdrucke aus den Nachrichten von der Gesellschaft der Wissenschaften zu Göttingen : Mathematisch-physische Klasse. Weidmannsche Buchh., 1930.

[68] T.-H. Shih, W. W. Liou., A. Shabbir, Z. Yang, and J. Zhu. A new $k-\epsilon$ eddy viscosity model for high reynolds number turbulent flows. *Computers & Fluids*, 24(3):227–238, 1995.

[69] F. R. Menter. Two-equation eddy-viscosity turbulence models for engineering applications. *AIAA Journal*, 32(8):1598–1605, 1994.

[70] F. R. Menter, R. Lechner, and A. Matyushenko. Best Practice: Generalized $k-\omega$ (GEKO) Two-Equation Turbulence Modeling in Ansys CFD. Technical Report Version 1.01, 2021 ANSYS.

[71] S. Wallin and A. V. Johansson. An explicit algebraic reynolds stress model for incompressible and compressible turbulent flows. *Journal of Fluid Mechanics*, 403:89–132, 2000.

[72] M. M. Gibson and B. E. Launder. Ground effects on pressure fluctuations in the atmospheric boundary layer. *Journal of Fluid Mechanics*, 86(3):491–511, 1978.

[73] Brian E. Launder. Second-moment closure: present... and future? *International Journal of Heat and Fluid Flow*, 10(4):282–300, 1989.

[74] B. E. Launder, G. J. Reece, and W. Rodi. Progress in the development of a reynolds-stress turbulence closure. *Journal of Fluid Mechanics*, 68(3):537–566, 1975.

[75] ANSYS Inc. Ansys Fluent Theory Guide. Technical report, ANSYS Inc., USA, 2022. Release 2022 R1.

[76] ANSYS Inc. Ansys Fluent User′s Guide. Technical report, ANSYS Inc., USA, 2022.

[77] F. R. Menter, R. Lechner, and A. Matyushenko. Best Practice: RANS Turbulence Modeling in Ansys CFD. Technical Report Version 1.01, 2021 ANSYS.

[78] E. Merzari, H. Ninokata, and E. Baglietto. Numerical simulation of flows in tight-lattice fuel bundles. *Nuclear Engineering and Design*, 238(7):1703–1719, 2008.

[79] ANSYS Inc. ANSYS Fluent Theory Guide. Technical report, ANSYS Inc., USA, 2016. Release 17.2.

[80] ANSYS Inc. ANSYS Meshing User's Guide. Technical report, ANSYS Inc., USA, 2016. Release 17.2.

[81] A. Shams, G. Damiani, D. Rosa, and E. M.J. Komen. Design of a single-phase PTS numerical experiment for a reference Direct Numerical Simulation. *Nuclear Engineering and Design*, 300:282–296, 2016.

[82] A. Shams, F. Roelofs, and E. M. J. Komen. High-Fidelity Numerical Simulation of the Flow Through an Infinite Wire-Wrapped Fuel Assembly. In *NURETH16*, pages 2817–2829, Chicago, 2015.

[83] A. Shams, F. Roelofs, E. Baglietto, S. Lardeau, and S. Kenjeres. Assessment and calibration of an algebraic turbulent heat flux model for low-Prandtl fluids. *International Journal of Heat and Mass Transfer*, 79:589–601, 2014.

[84] B.E. Launder and D.B. Spalding. The numerical computation of turbulent flows. *Computer Methods in Applied Mechanics and Engineering*, 3(2):269–289, 1974.

[85] D. Chang and S. Tavoularis. Unsteady Numerical Simulations of Turbulence and Coherent Structures in Axial Flow Near a Narrow Gap. *Journal of Fluids Engineering*, 127(3):458–466, 2005.

[86] D. Chang and S. Tavoularis. Numerical simulations of developing flow and vortex street in a rectangular channel with a cylindrical core. *Nuclear Engineering and Design*, 243:176–199, 2012.

[87] Amer Mahmood. *Single-phase crossflow mixing in a vertical tube bundle geometry - An experimental study.* PhD thesis, Technische Universiteit Delft, 2011.

[88] H. Ramm, K. Johannsen, and N. E. Todreas. Single phase transport within bare rod arrays at laminar, transition and turbulent flow conditions. *Nuclear Engineering and Design*, 30(2):186–204, 1974.

[89] I. Tiselj. Tracking of large-scale structures in turbulent channel with direct numerical simulation of low prandtl number passive scalar. *Physics of Fluids*, 26(12):125111, 2014.

[90] J. Y. Murthy and S. Mathur. Periodic Flow and Heat Transfer Using Unstructured Meshes. *Int. J. Numer. Meth. Fluids*, 25(25):659–677, 1997.

[91] James W. Lottes Paul F. Fischer and Stefan G. Kerkemeier. nek5000 Web page, 2008. http://nek5000.mcs.anl.gov.

[92] M. O. Deville, P. F. Fischer, and E. H. Mund. *High-Order Methods for Incompressible Fluid Flow*. Cambridge University Press, 2002.

[93] A. Shams and E. M. J. Komen. Towards a direct numerical simulation of a simplified pressurized thermal shock. *Flow, Turbulence and Combustion*, 101:627 – 651, 2018.

[94] A. W. Vreman and J. G. M. Kuerten. Comparison of direct numerical simulation databases of turbulent channel flow at $re_\tau = 180$. *Physics of Fluids*, 26(1):015102, 2014.

[95] J. Kim, P. Moin, and R. Moser. Turbulence statistics in fully developed channel flow at low reynolds number. *Journal of Fluid Mechanics*, 177:133–166, 1987.

[96] H. Kawamura, K. Ohsaka, H. Abe, and K. Yamamoto. Dns of turbulent heat transfer in channel flow with low to medium-high prandtl number fluid. *International Journal of Heat and Fluid Flow*, 19(5):482–491, 1998.

[97] M. Niemann and J. Fröhlich. Direct numerical simulation of turbulent heat transfer behind a backward-facing step at low prandtl number. *PAMM*, 14(1):659–660, 2014.

[98] J. D. Hooper, D. H. Wood, , and W. J Crawford. Data Bank of Developed Single-Phase Flow Through a Square-Pitch Rod Cluster for Four Reynolds Numbers,. Technical report, Australian Nuclear Science and Technology Organisation, 1983.

[99] E. Baglietto, H. Ninokata, and T. Misawa. Cfd and dns methodologies development for fuel bundle simulations. *Nuclear Engineering and Design*, 236(14):1503–1510, 2006. 13th International Conference on Nuclear Energy.

[100] P. Welch. The use of fast fourier transform for the estimation of power spectra: A method based on time averaging over short, modified periodograms. *IEEE Transactions on Audio and Electroacoustics*, 15(2):70–73, 1967.